Modeling of Induced Surface Oscillation Damping Behavior in Levitated Molten Metal Droplets

Submitted by

Xiao Xiao

In partial fulfillment of the requirements for the degree of

DOCTOR OF PHILOSOPHY

in Mechanical Engineering

School of Engineering, Tufts University

August 2017

Certified by: _____

Douglas Matson, Associate Professor
Department of Mechanical Engineering, Tufts University

Committee: _____

Anil Saigal, Professor
Department of Mechanical Engineering, Tufts University

Committee: _____

Xiaozhe Hu, Assistant Professor
Department of Mathematics, Tufts University

Committee: _____

Jonghyun Lee, Assistant Professor
Department of Mechanical Engineering, Iowa State University

Abstract

Measurement of thermophysical properties including the temperature-dependent viscosity of molten metals is important in material research. Microgravity Electromagnetically levitation (EML) experiments on board the International Space Station (ISS) were launched to measure the viscosity of levitated molten metal droplets through the analysis of the damping behavior of oscillations induced by pulse excitations.

The work presented here contributes in the following areas. Firstly, the damping behavior of the oscillating droplet could be evaluated from the two-dimensional projected image signals of the sample droplet using an elliptical fit, and the time-temperature-dependent damping rate of the oscillating droplet could be derived through appropriate segmentations of the oscillating signals. Secondly, possible factors that would influence the damping rate analysis and viscosity measurement are evaluated, including the power settings of EML coil, test temperature of the molten metal liquid, and the magnitude and distribution of oscillation modes for droplet deformation. Thirdly, the oscillation transition behavior of the damped signal is presented which reflects in an overestimated damping rate and an increased apparent viscosity of the droplet primarily due to the turbulent convection inside the droplet induced from the heater pulse. An empirical estimation of the time scale for turbulence decay is established based on the experimental data and Magnetohydrodynamic(MHD) simulation results. Finally, a guideline is provided for parameter design for viscosity measurement experiments using the ISS EML facility. Based on these analyses, space results are compared to previous containerless results and although each data set shows similar accuracy, the precision of the measurements is shown to vary by 10.7% for ground-based electrostatic levitation, and 13.8% for parabolic flight EML as compared to 7.4% for the new space EML results presented in this work.

Table of Contents

List of Figures

List of Tables

Acknowledgements

I would like to express my appreciation to my advisor, Professor Douglas Matson, who supports and advises me throughout my studies during the years. I was always inspired by his wit and erudition either in research or non-academic aspects.

I would like to thank Professor Jonghyun Lee who provided lots of advices from the beginning of this work in both of modeling and data analysis section, and Professor Anil Saigal and Professor Xiaozhe Hu for serving on my dissertation committee, who devoted their precious time and effort to review my work and gave important suggestions.

I would like to thank our collaborators—the colleagues of the DLR in Cologne, Germany, for their tremendous technical support on the experiments, and Professor Robert Hyers of University of Massachusetts-Amherst, and Dr. Rainer Wunderlich of University of Ulm, Germany, for their valuable advices.

I would like to thank NASA for the funding support for this work under grant NNX16AB59G.

Finally, I would like to thank my family for their support through my life.

1 Introductions

1.1 Purpose and Motivation

This work systematically studies the damping behavior captured with a machine vision technique for an electromagnetically levitated (EML) molten metal droplet which is subjected to induced surface oscillation and develops analysis methods to conduct viscosity measurement for molten metals in microgravity. The objective of this work is to better understand and explain the damped oscillation behavior of a levitated molten metal droplet, determine the valid regime and improve the accuracy of the viscosity measurement, and provide a guideline for experiment parameter design using the EML technique. As the results, viscosities of several molten alloys are measured from the EML experiments on board the International Space Station (ISS) utilizing the techniques developed in this work. These results also demonstrate the theory presented in this work regarding the levitated droplet's damped oscillation behavior.

Thermophysical properties of molten metals, including viscosity, density, etc., are fundamental and crucial properties for widely-used industrial important alloys or various high-performance alloys. Accurate values of thermophysical properties are also required in the simulation of fluid flow during metal material solidification and processing, such as predictions of dendritic growth in the undercooled melts, modeling of casting, welding process, etc. However, it is usually hard to precisely measure the viscosity of molten metals at high temperature or in the undercooled region using traditional experiment equipment such as rotating cup viscometry due to the high reactivity between the melt and test container such that contamination prevents the melt from achieving deeply undercooled conditions.

Containerless measurement techniques have been developed to overcome the existing difficulties; examples include aerodynamic levitation, electrostatic levitation, and electromagnetic levitation. Especially in the microgravity environment, the EML facility could levitated a relatively large-size molten metal droplet under a wide range of temperature from several hundreds of superheating to deep undercoolings; additionally control is demonstrated across various internal convection conditions from nearly negligible laminar flow to fully developed turbulence through careful selection of operating parameters. The viscosity of a

molten metal sample could be measured through the analysis of high-speed camera which captures the damping behavior of the droplet's oscillation which can be induced using electromagnetic pulse forces applied to the sample. However, the current experiment design for viscosity measurement utilizing ISS EML facility is empirically-based. The timing and size of the pulse applied and the selection of camera operation conditions, etc., would significantly affect the validity (accuracy and precision) of the measurement using a machine vision technique, such as how the turbulent convection inside the molten droplet induced from electromagnetic momentum force could produce an overestimated apparent viscosity due to turbulent eddies that changes the momentum transfer mechanism, and how the camera settings could skew the assessment of captured damped oscillating signals. Thus, it is important and necessary to study the induced oscillation damping behavior of the levitated molten metal droplet under the influences of various factors to allow evaluation of the experimental techniques and provide a template for more parameterized experiment design in the future.

1.2 Background

1.2.1 Containerless measurement techniques

A containerless levitation facility provides the capability to position and process a metal sample without requiring the use of a crucible to hold the sample. For the studies of metals with high reactivity, Electrostatic Levitation (ESL) and Electromagnetic Levitation (EML) are usually used.

The principle of ESL is that a static electric field is applied to charge and levitate either a conductive or non-conductive sample from positioning electrodes in an evacuated chamber while the test temperature is controlled by a heating laser which is independent of the operation of the levitation system. Due to the limitations on levitation force, ESL facilities can only support relatively small samples – on the order of 50mg weight or 2-3 mm in diameter. While the heating laser is on, the molten sample is irradiated from a single side which could introduce Marangoni convection flow inside the droplet due to thermal gradients from unbalanced

temperature distribution. The internal Marangoni flow is usually laminar with moderate to negligible flow velocity.

The principle of EML is that an alternating electromagnetic field is applied to a conductive sample located within a water-cooled high frequency electromagnetic coil. Eddy currents induced inside the sample provide coupled sample heating and sample positioning functions. The test temperature is controlled by adjustment of the field, and the cooling rate of the sample is controlled by the flow of gas over the sample in terrestrial applications. In space, where the sample weight does not need to be overcome, two separate coil frequencies are utilized (one for heating and one for levitation positioning) and testing may be accomplished either in vacuum or in a gas environment without the need for cooling gas. EML could support relatively large sample on the order of 1g weight or 5-7mm in diameter. While the electromagnetic field is imposed on a molten sample, convective flow inside the droplet is induced by the applied Lorenz force. The internal convection is significant when the heating power is on, and may cause turbulence flow inside the droplet during processing.

The theory and model of the electromagnetically levitated droplet was developed from Okress[1]. Lohöfer presented the absorbed power, current distribution and impedance of an electromagnetically levitated metal sphere [2][3][4]. Szekely, et al. developed the mutual inductance method [5] to calculate electromagnetic forces in the spherical droplets, and discussed the shape of levitated droplet surface [6]. In this work, the SUPOS coil is utilized on board the ISS in a microgravity environment; the design basics of the coil are presented by Lohöfer [7].

During the EML experiments, the MSL-EML facility may be used to conduct thermophysical property measurements and solidification studies. In the solidification experiments, nucleation phenomenon, growth mechanism, and phase selection, etc. are studied. In the thermophysical property measurement experiments, the viscosity, density, surface tension, resistivity, heat capacity, and emissivity of metal sample is usually of research interest. The measurement of viscosity is of primary concerned in this work.

1.2.2 Measurement of viscosity

Fluid viscosity is a measure of resistance to shear or tensile stress. For Newtonian fluid including most molten metals, the shear stress is linearly proportional to shear rate connected with the coefficient of viscosity term. Viscosity has a simple functional dependence with temperature for most molten metals. An Arrhenius relation of viscosity versus temperature presented in Equation 3.2.1 is often most appropriate while it might be invalid for some glass forming alloy under deep undercoolings near the glass transition region due to change of the molecular interaction mechanism.

Traditional viscosity measurement methods need containers to hold the molten sample, including rotational viscometers, oscillating vessel and oscillating plate methods, which are surveyed in [8][9].

The contactless oscillating droplet method is usually used in containerless levitation techniques for viscosity measurement. The levitated droplet is subjected to an excitation force which is allowed to freely dampen out, and the viscosity can be evaluated through analysis of the damping rate related to the evolution of the deformed droplet shape with time. Lamb[10][11] and Rayleigh[12] developed the theory and expression for viscosity and surface tension in terms of the oscillation damping rate and resonant frequency. Further studies [13][14] discussed the damping behavior of viscous droplets subjected to different modes of oscillations including nonlinear effects. Recent work [15][16][17] has concentrated on the discussion of the influence of application of large amplitude oscillations on the viscosity and surface tension measurement. Egry [18] discussed the oscillation behavior for a sample with a difference in composition between bulk and surface, for example a contaminated sample with an oxide layer, and how these conditions influence droplet damping.

Based on the oscillating droplet method, a number of experiments were conducted using containerless levitation techniques. Viscosity measurement using ground-based ESL[19][20] is reported and the influence of electrostatic positioning force [21][22] is discussed highlighting the effects of environmental oxygen on the evaluation of droplet damping rate. Ground-based EML [23][24], parabolic flight EML in reduced gravity [25-27], and space EML in microgravity [29-31] have all been used extensively. In addition, there are reports of viscosity

measurement using gas-levitation [32], and surface oscillation techniques [33][34] using electric inductive signals reflection.

For the viscosity measurement using EML, the most influential factor is the induced convection; the measurement requires laminar flow and turbulence would make the measured results invalid [35][36]. Thus, during the experiment, the internal convection flow should be reduced appropriately for an effective viscosity measurement.

1.2.3 Magnetohydrodynamic models

The convective flow inside electromagnetically levitated droplets could have significant influence either on the solidification behavior of molten metals or on the validity of results from thermophysical property measurement. Previous research [37-39] showed that the nucleation behavior of the molten alloys, the dendritic growth, and the resulting microstructures will be affected by the internal convective flow. Work from the group of Szekely at MIT [35][36] states that turbulent convection will make the viscosity measurement impossible. A well-controlled and predictable convection flow condition is necessary to support related research and experiments. It is normally difficult to measure the internal convection velocity directly from experiment, and numerical methods have been developed to model the internal fluid flow of levitated droplets.

Magnetohydrodynamic (MHD) numerical models for the EML droplets was previously developed [5][40] using a k-ε turbulence model (turbulent kinetic energy - turbulent energy dissipation) for both ground-based and microgravity conditions. Recent work [41][42] reported results from calculations for laminar flow in spherical droplets in a microgravity EML facility, and extended to turbulent flow of gravitationally-deformed droplets in ground-based EML. Berry *et al.* [43] surveyed the turbulence models and stated that RNG k-ε turbulence model (renormalization group method variation) is the most suitable model for EML droplets. For the laminar-turbulence transition behavior in an electromagnetically levitated droplet, Hyers [45] suggested that the convection is laminar for a Reynolds number below 600 with transition to turbulent flow above the number. This is indicated by the formation and perturbation of the

stagnation line around the droplet equator as evidenced by experiment observations. Lee [46] validated the k-ε turbulence model through MHD simulation of convection in a copper-cobalt droplet levitated in ground-based EML, whose predicted flow velocity along the sample surface showed agreement with the experiment. Lee [47] also predicted the convection flow velocity and laminar/turbulence status for iron-based alloys levitated in microgravity EML in support of the experiments on board the International Space Station(ISS). As presented in Figure 1.2.1, guidelines [48] can be established for flow convection conditions under ground-based ESL, ground-based EML, and microgravity EML with different sample size. The flow is mainly laminar in ESL, and fully turbulence in ground-based EML, and could achieve a wide range from negligible laminar to fully turbulent in microgravity EML.

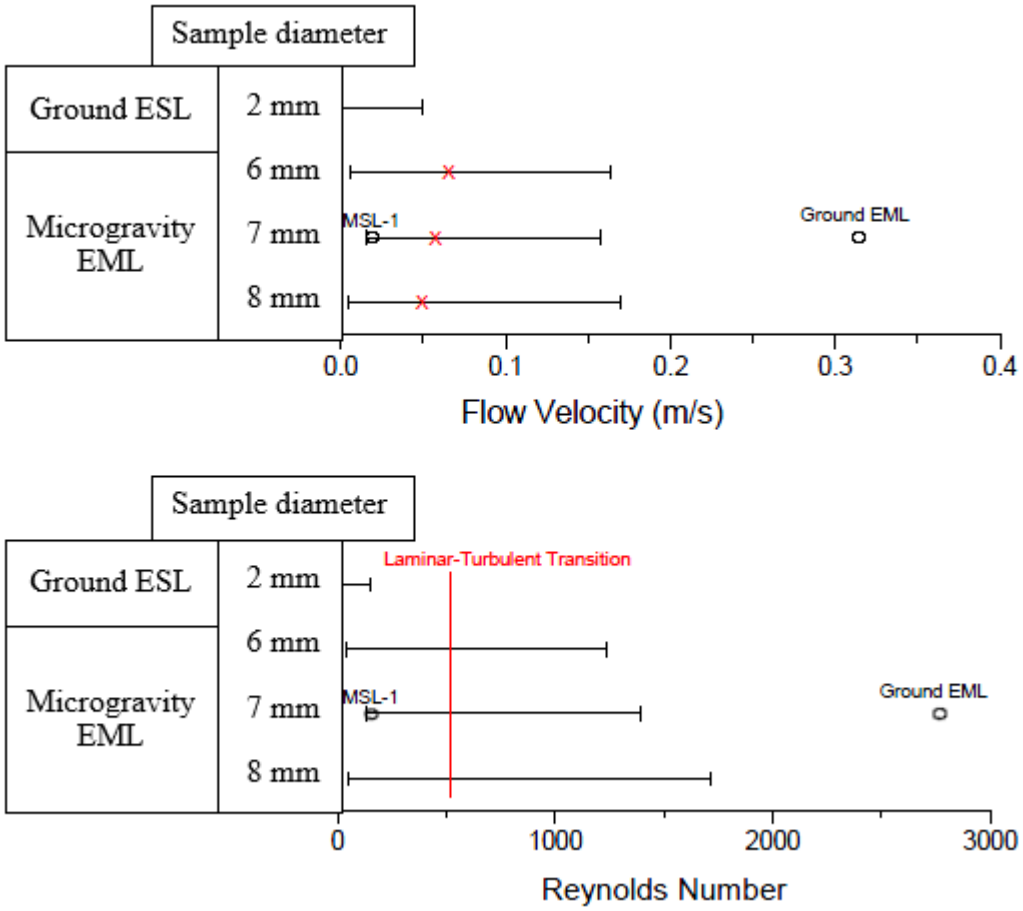

Figure 1.2.1: Ranges of Flow Velocity and Reynolds Number of Steel in ground ESL, ground EML, and Microgravity EML[48]

In addition to the k-ε turbulence models, other numerical methods have been developed. For the magnetic levitated liquid droplet, Bojarevics [49][50][51] used pseudospectral methods to solve the Navier-Stokes Equations with k-ω turbulence model (turbulent kinetic energy – dissipation rate), and extended the model to three-dimension. Easter [52][53] applied this method to simulate oscillating droplet subjected to multiple oscillation modes. Shatrov [54] analyzed the three-dimensional stability of the flow inside magnetic levitated droplet. Bjorkland [55] simulated the dynamics of a droplet subjected to an electric field with a Level-set method which is commonly applied in numerical analysis regarding surfaces and shapes.

1.3 Organization

This work consists of the following chapters:

Chapter 2 – Measurement Methods, discusses video and image processing related techniques including elliptical fitting method, aliasing effect, and segmentation analysis of the projection image signals.

Chapter 3 – Damped Oscillation Analysis, describes the transition behavior of the damped oscillating signals of the levitated droplet subjected to pulse excitation, and discusses multiple factors that might have potential influence on the droplet's damping behavior and viscosity measurement, including the heater high testing temperature/heater pulse power, large sample deformations, skewness from the sample projection under different oscillation modes, and nonlinear effect from anharmonic oscillation.

Chapter 4 – Magnetohydrodynamic simulation, introduces the MHD simulations for both equilibrium and transient status of the convective flow inside the electromagnetically levitated droplet. The laminar/turbulence region of the convective flow is predicted for various testing temperature and power settings, and an estimation of turbulence decay time is established based on the experimental data and simulation results.

Chapter 5 – Results and discussion, summarizes the key points in viscosity measurement, and presents viscosity results for three molten alloys as examples of application of the methods

proposed in this work. The acceptable region of test temperature/pulse excitation is predicted numerically to provide suggestions for parameter selection and control in the design of future experiments.

Chapter 6 – Conclusions, describes the achievements and contributions throughout this work.

Chapter 7 – Future work is suggested.

2 Experimental Methods

2.1 Electromagnetic Levitation on the International Space Station

The experiment was conducted using the MSL-EML facility in microgravity on the International Space Station. The size of the sample is around 6.5 mm in diameter, and inert gas such as helium or argon is often used to limit evaporation although the tests may also be run in vacuum. The sample was positioned and heated using SUPOS coil system[56] as shown in Figure 2.1.1 where a sample holder cage is installed in the center of the coil set. SUPOS coil is a single-coil/dual-current type with upper and lower coils wound in one piece; the heating and positioning current is controlled independently. The alternating current through the coil runs at a frequency of 150 kHz for the positioner that generates a quadrupole electromagnetic force field to locate the sample near the center of the coil set, and 350 kHz for the heater generating a dipole electromagnetic field and heat the sample by resistive heating due to the eddy currents. The schematic of SUPOS coil is shown in Figure 2.1.2. The coil currents and the control voltage has the following linear relations, where I_H is the heating current, I_P is the positioning current, V_H^{Ctrl} is the heater control voltage, and V_P^{Ctrl} is the positioner control voltage.

$$I_H = 19.09 + 19.00 \cdot V_H^{Ctrl}$$
$$I_P = 12.03 + 12.03 \cdot V_P^{Ctrl} \quad (2.1.1)$$

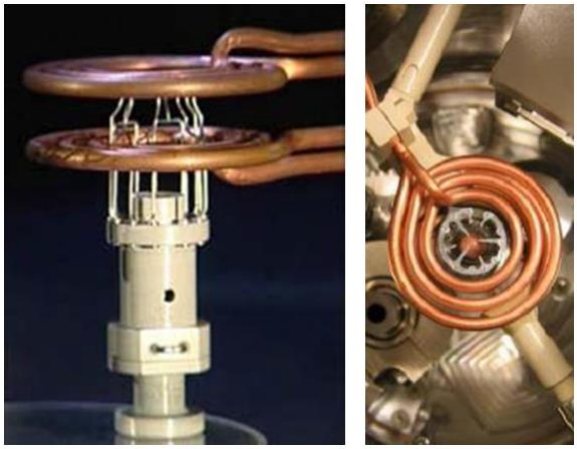

Figure 2.1.1: ISS EML SUPOS coil used to position and heat the sample

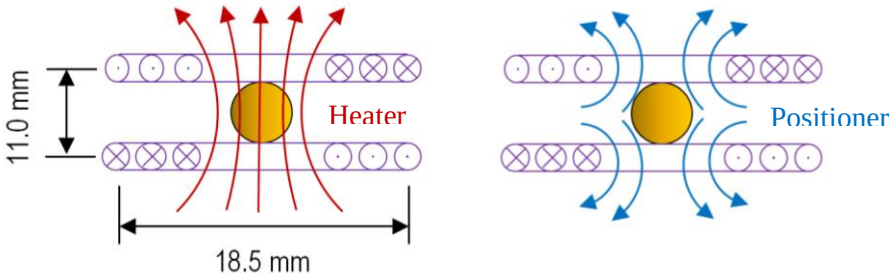

Figure 2.1.2: Schematic of SUPOS coil

2.2 Imaging and Signal Processing Technique

For a typical MSL-EML cycle, there are two cameras installed to capture the motion of the molten droplet. The top-view axial camera is nominally set to 8-bit grayscale 384x384 pixels at 150 Hz for viscosity and surface tension measurement[31], and facility health monitoring mode at 25 Hz. The side-view radial camera has two lens settings, high speed with 256x256 pixels at 30 kHz for recalescence detection and high resolution with 600x600 pixels at 400 Hz for data acquisition during viscosity measurement.

2.2.1 Video processing

The videos captured from 150 Hz top-view and 400 Hz side-view video are analyzed frame-by-frame to detect the projections of the sample, and synchronized the time-stamp with pyrometer profiles to obtain the time-temperature-oscillation data for further analysis. Figure 2.2.1 showed a typical sample projection from the top-view and side-view cameras, where the white pixels represented the molten sample. The shadow across the surface is caused by interference in view by the sample holder wire cage. White lines represent reflections of the wires which are distorted when viewed on the mirror surface finish of the molten sample.

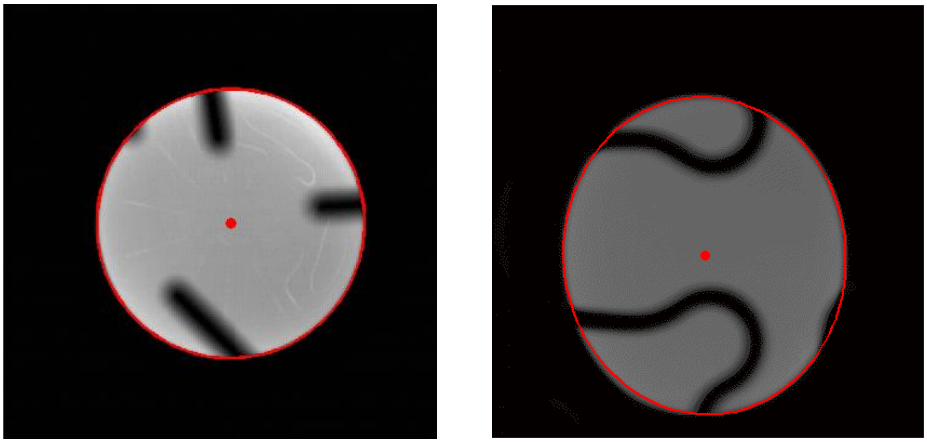

(a) Top-view camera **(b) Side-view camera**

Figure 2.2.1: Typical projections of the sample

For each frame, the 8-bit grayscale image was read into a logical matrix and converted to a $2 \times n$ coordinate array P, representing the 2-D Cartesian coordinate of the sample projection region. Khachiyan's Algorithm[58][59] was adopted to apply an ellipse fit (in red on the figure), finding the minimum area enclosing ellipse of the 2-D region defined by P, the fitted ellipse equation is in the following form,

$$(x - c)^T \ A \ (x - c) \ = \ 1 \tag{2.2.1}$$

Where A is a 2×2 matrix, and c is a 2 dimensional vector representing the centroid of the ellipse.

Khachiyan Algorithm: Find the A and c satisfing that,

$$\begin{gathered} \text{Minimize } det(A) \\ \text{subject to} \qquad (P_{i\_th\ column} \ - \ c)^T \ * A * (P_{i\_th\ column} \ - \ c) \ <= \ 1 \end{gathered} \tag{2.2.2}$$

0. Initialize $n \times 1$ vector: $u = \begin{bmatrix} u_1 \\ \dots \\ u_n \end{bmatrix} = \begin{bmatrix} \frac{1}{n} \\ \dots \\ \frac{1}{n} \end{bmatrix}$, and $3 \times n$ matrix: $Q = \begin{bmatrix} P_{11} & \dots & P_{1n} \\ P_{21} & \dots & P_{2n} \\ 1 & \dots & 1 \end{bmatrix}$,

1. Calculate 3×3 matrix $X = Q * U * Q^T$, and $n \times n$ matrix $M = Q^T / X * Q$,

2. Find maximum element $max(M)$ on the diagonal of M with index j, $step\_size = \frac{max(M)-3}{3\,(max(M)-1)}$

3. Update vector u:

$$u = (1 - step\_size) * u, \text{ and } u_j = u_j + step\_size$$

4. Repeat Step 1 – 3 until $err = norm(u_{updated} - u)$ is less than preset accuracy tolerance value.

Set $n \times n$ diagonal matrix: $U = \begin{bmatrix} u_1 & & \\ & \ldots & \\ & & u_n \end{bmatrix}$ and find A and c as follows,

$$A = \frac{1}{2}\,(P * U * P^T - (P * u) * (P * u)^T)^{-1} \tag{2.2.3}$$

$$c = P * u$$

Thus, the fitted ellipse has the following properties,

$$\text{Length of Maximum semi-axis: } R_1 = \frac{1}{\sqrt{\sigma_1}}$$

$$\text{Length of Minimum semi-axis: } R_2 = \frac{1}{\sqrt{\sigma_2}} \tag{2.2.4}$$

$$\text{Deflection angle: } \theta = \frac{1}{2} atan(\frac{2A_{12}}{A_{11} - A_{22}})$$

Centroid: (c_1, c_2) in Cartesian coordinate

Fitted Ellipse Area: $area = \pi R_1 R_2$

Where σ_i is the singular value of matrix A, derived from singular value decomposition (SVD).

For example, for a typical damped oscillation following a pulse excitation, Figure 2.2.2 shows the maximum/minimum radius of the fitted ellipse from the top view, and Figure 2.2.3 shows the ellipse area. Fast Fourier transform (FFT) is usually used on the changing amplitude of the damped oscillation signal to filter the data within its primary oscillation frequency region. As shown in Figure 2.2.4, the natural frequency around 35 Hz has the largest amplitude in the FFT analysis, and the signal is filtered near the detected frequency for further analysis.

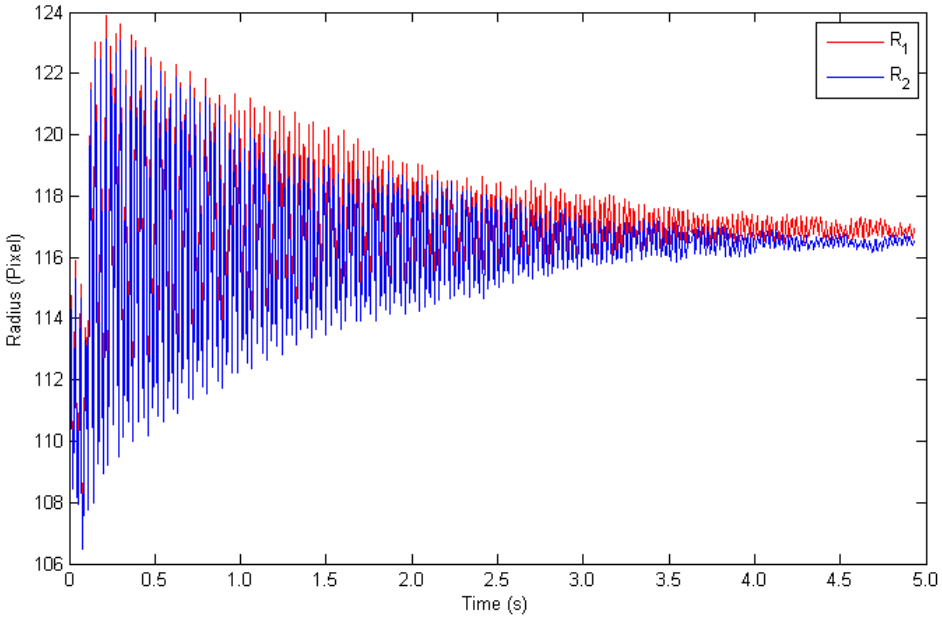

Figure 2.2.2: Length of max/min semi-axis R_1/R_2 in fitted ellipse

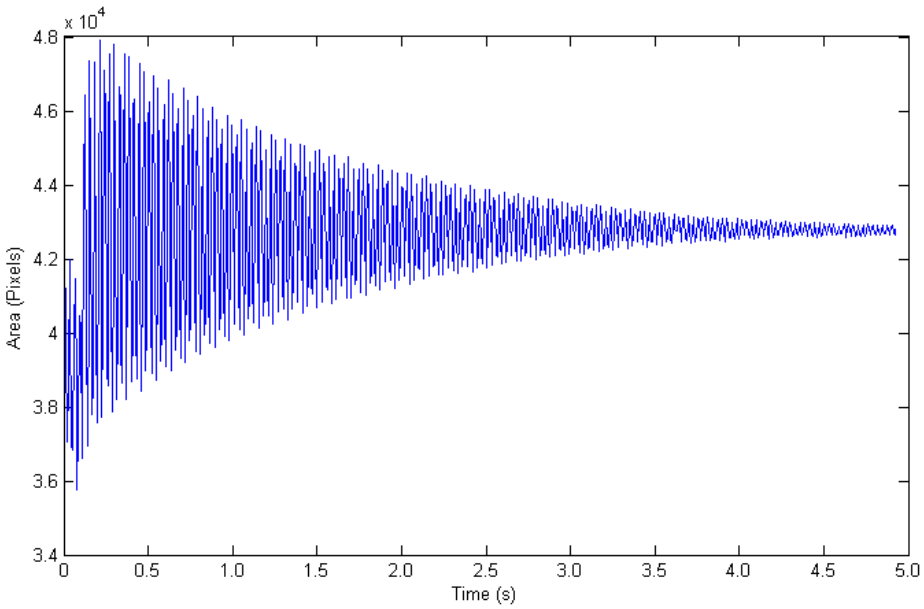

Figure 2.2.3: Area of fitted ellipse

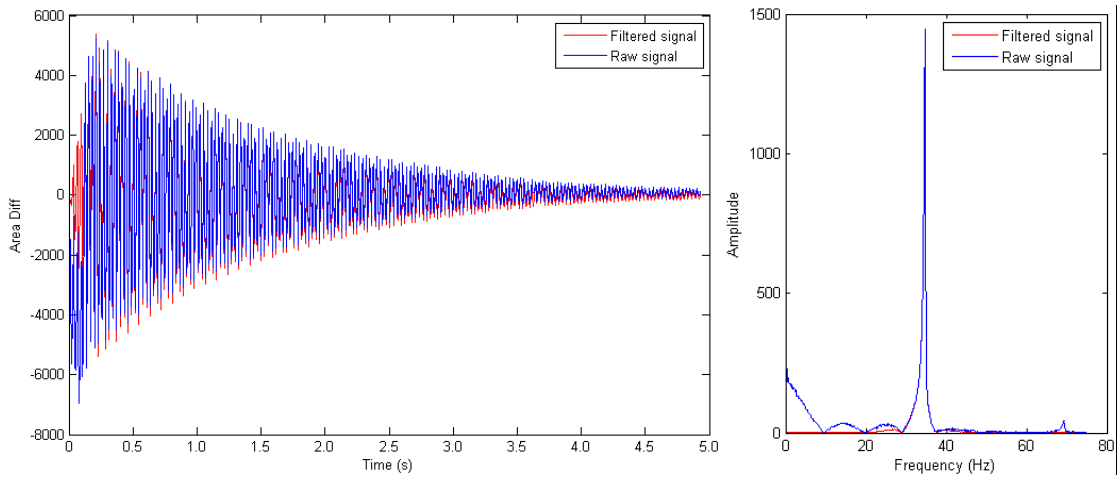

Figure 2.2.4: FFT of oscillation signals

2.2.2 Aliasing effect

The natural frequency for a 6.5mm diameter levitated molten droplet of selected alloy such as FeCrNi is normally 35-38 Hz, which could be revealed by Fast-Fourier Transform (FFT) analysis of the damped oscillation signal showing the shape deformation of the sample[57]. During the ISS EML experiments, the facility health monitoring video works at 25 Hz, and Top-view and Side-view video is normally set to 150 Hz and 400 Hz, respectively.

During facility checkout, the 25 Hz facility health monitoring video was the only available data source due to hardware configuration issues and aliasing played a significant role when data was evaluated. Consider the situation measuring a signal with natural frequency of 36.6 Hz with the video system at acquisition rate of 25 Hz. The Nyquist frequency limit is 25/2=12.5 Hz, and the actual 36.6 Hz signal is undersampling expecting information lost and aliasing. A simulated decaying sinusoidal signal is plotted in Figure 2.2.5, the signal frequency 36.6 Hz and the amplitude is arbitrarily reduced due to viscous damping, where the connected blue dots showed the beats formed from undersampling. The FFT analysis of the undersampled simulation showed the aliasing behavior at 11.72 Hz and 13.43 Hz as shown in Figure 2.2.6, and the simulated beats rate is 13.43-11.72=1.82 Hz as the effect combining the two aliases.

For signal frequency $f = 36.6\,Hz$ and sampling rate $f_s = 25\,Hz\ (n = 1, 2, \ldots)$, the theoretical value of the alias frequencies and beats rate could be calculated as follows,

$$\begin{gathered} 1^{st}\text{ alias frequency: } {f_a}^1 = f - (n)f_s = \ 11.6\text{ Hz } (n = 1) \\ 2^{nd}\text{ alias frequency: } {f_a}^2 = (n)f_s - f = \ 13.4\text{ Hz } \ (n = 2) \\ \text{Beats Rate: } f_{beat} = {f_a}^2 - {f_a}^1 = 1.8\text{ Hz} \end{gathered} \tag{2.2.5}$$

For the FFT analysis above the $f_s = 25\,Hz$ region, it also shows the frequency at 36.63 Hz and 38.34 Hz, and the alias frequencies of the alias could be calculated as,

$$\begin{gathered} \text{alias frequency of } 1^{st}\text{ alias: } {f_a}^{1'} = {f_a}^1 + f = 36.6\text{ Hz} \\ \text{alias frequency of } 2^{nd}\text{ alias: } {f_a}^{2'} = {f_a}^2 + f = 38.4\text{ Hz} \end{gathered} \tag{2.2.6}$$

Thus, the alias frequency of 1st alias represents the actual signal frequency which also has maximum signal amplitude in FFT analysis, and the oscillation frequency of the sample could be measured during undersampling situation, though it provides limited information for damping behaviour analysis.

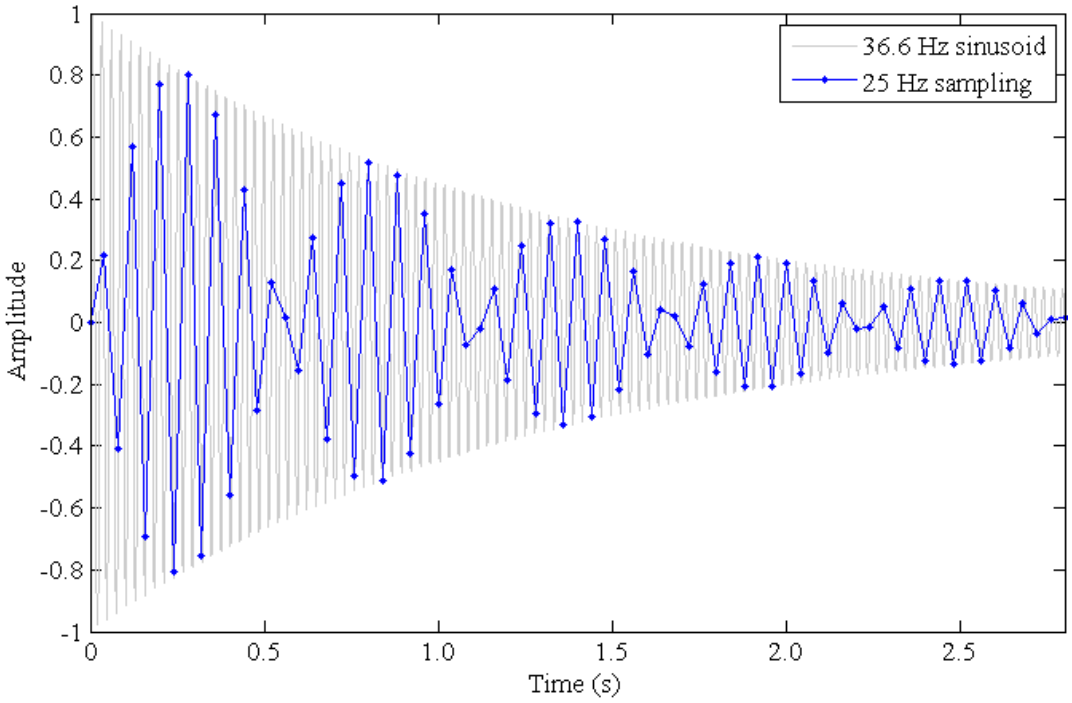

Figure 2.2.5: Simulated decaying sinusoid signal at 36.6 Hz with undersampling at 25 Hz

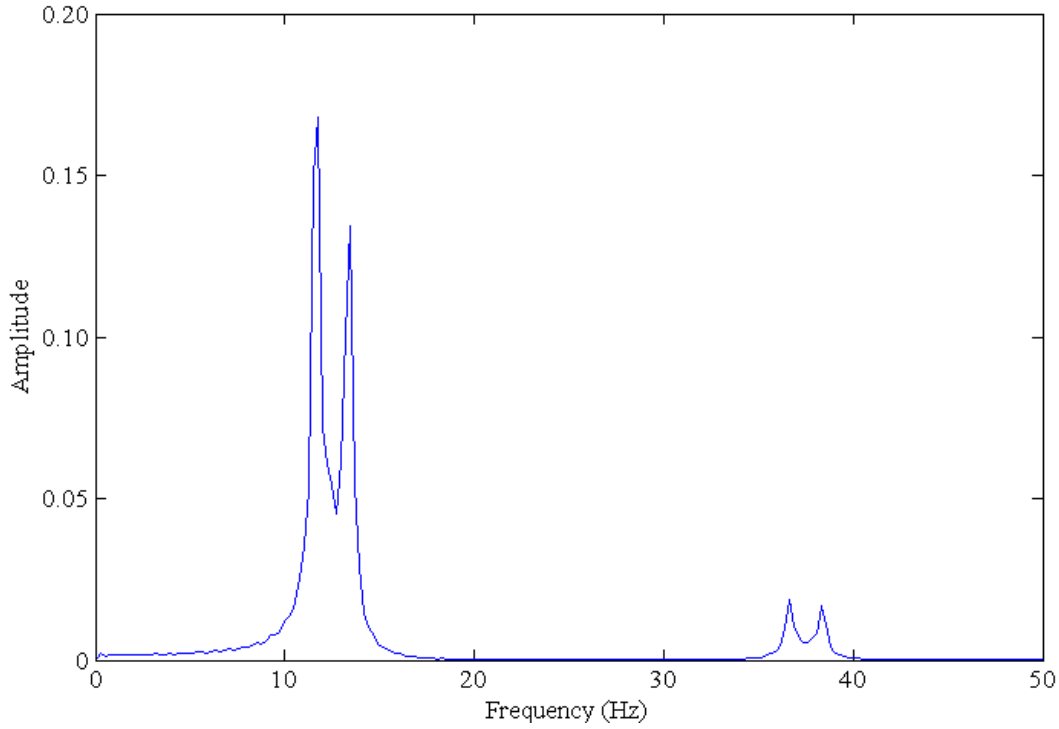

Figure 2.2.6: FFT of simulated sinusoid signal at 36.6 Hz with undersampling at 25 Hz

For an oversampling situation, if the sampling rate f_s is expected to be greater than 100 Hz, the Nyquist frequency $\frac{f_s}{2} > 50\ Hz$ would be appropriate for most alloy samples. Figure 2.2.7 shows a simulated sinusoidal signal with acquisition rate of 150 Hz that is usually set in Top-view video, and FFT analysis provides the frequency value of 36.69 Hz as shown in Figure 2.2.8. The video under oversampled condition is normally expected for thermophysical property measurement, and the effect of aliasing could be diminished with increased acquisition rate. Note that during nominal operations following facility check-out, sampling rate was increased. Thus the undersampling issues were resolved.

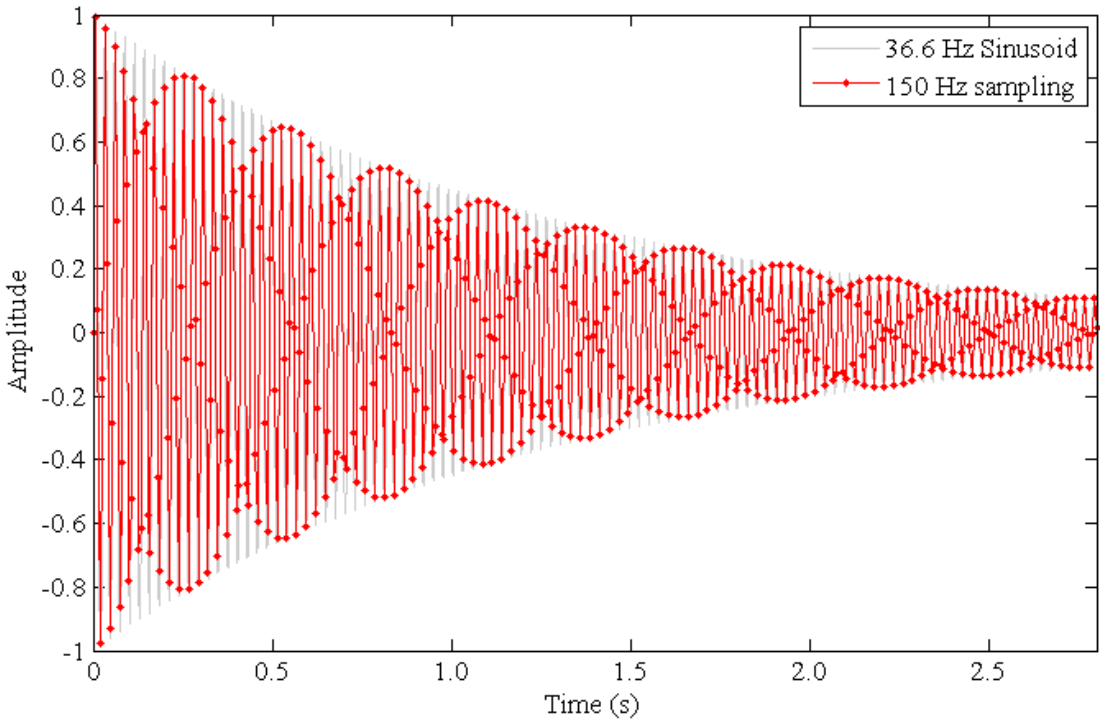

Figure 2.2.7: Simulated decaying sinusoid signal at 36.6 Hz with oversampling at 150 Hz

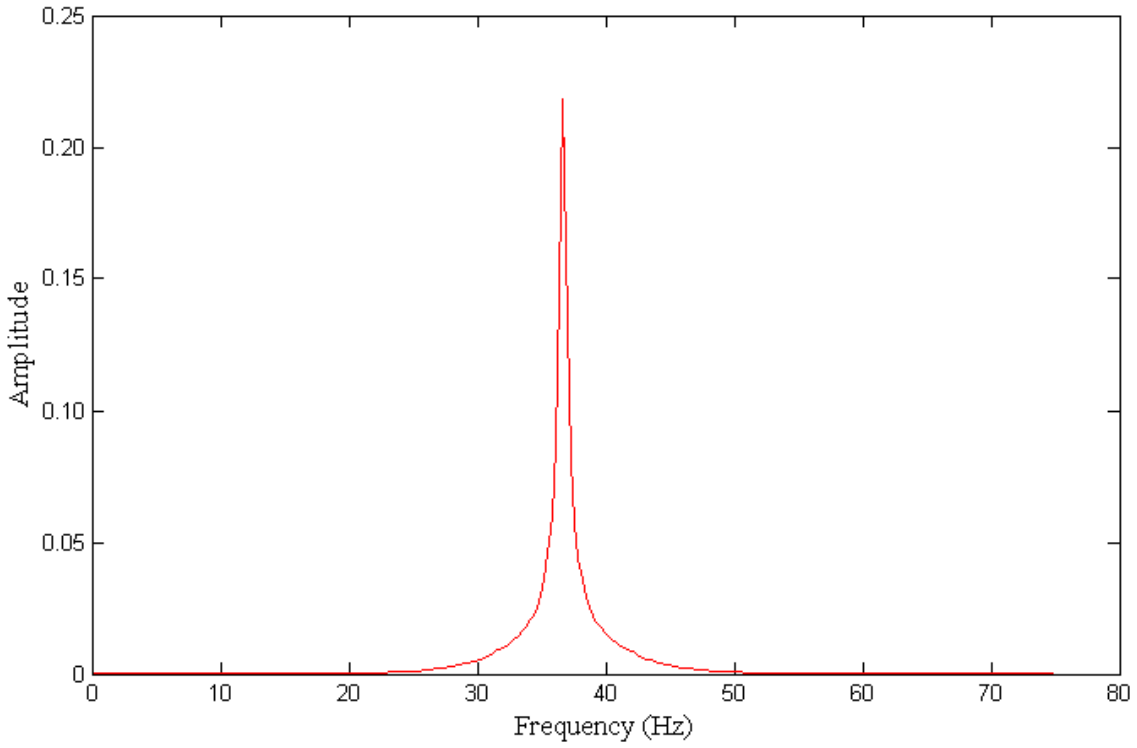

Figure 2.2.8: FFT of simulated sinusoid signal at 36.6 Hz with oversampling at 150 Hz

2.3 Segmentation Error Analysis

2.3.1 Time-Temperature profile

During a typical ISS EML thermal cycle, the sample temperature is measured with a single-color pyrometer, and the positioner and heater are maintained at a relatively large power level to maintain the stability of the sample and melt/superheat it quickly to reduce evaporation. The heater is then turned off or tuned to a moderate level to control the cooling rate of the molten sample, and the sample would be excited by one or more heater pulses at 5.0 ~ 9.0 Volts for 0.1 second duration at selected times during the cooling process prior to recalescence. For each pulse excitation, the levitated sample will start to oscillate and the oscillations will be damped out over time. The viscosity can be measured during this period using oscillating droplet method[31]. Figure 2.3.1 presents a typical Time-Temperature profile and damping signal showing the deformation of the sample. In this example, a molten FeCrNi sample was superheated to 1650 ℃ with 10.0V positioner and 7.8V heater, then the positioner was set to 5.2V and the heater was turn off to allow the sample to cool down freely. During the free cooling

process, two pulses of 6.0V and 7.0V were applied to excite the sample, and the change of the projected area of the sample could be detected from the Top-view video with synchronized time-stamps.

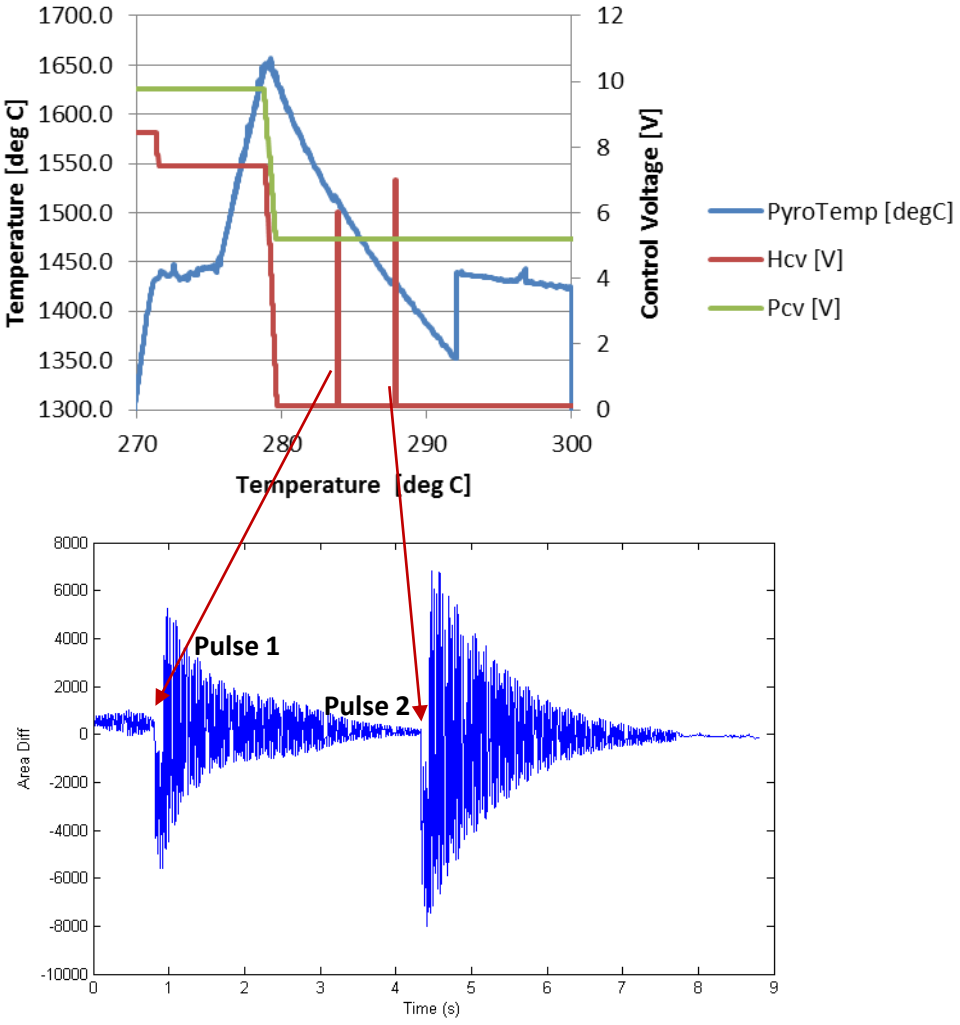

Figure 2.3.1: Time-Temperature profile and Damping signal of the sample for a typical thermal cycle with pulse excitations

2.3.2 Error in the decay of the sinusoidal signal fit

For a mode $l = 2$ oscillation[36], the viscosity μ of the sample can be determined as follows,

$$\mu = \frac{\rho R_0^2}{(l-1)(2l+1)\tau} \tag{2.3.1}$$

where τ is the damping constant representing the decaying rate of the damped oscillations, ρ and R_0 is the density and initial radius of the sample.

The variation of the deformation signal of levitated molten droplet changes with time, which can be expressed as an exponential decaying sinusoid with frequency f.

$$y(t) = y_0 \cos(2\pi f t) e^{-\frac{t}{\tau}} \tag{2.3.2}$$

The extreme value points in the sinusoidal signal are detected and can be used to fit the damping constant. The damping constant and viscosity changes with different sample temperature which was decreased with time. Thus, an appropriate segmentation of the decaying signal is necessary to fit the damping data for each small range of temperature change, showing the dependence of the thermophysical property on the temperature.

To evaluate data fitting accuracy on the damping constant and viscosity, apply a linear regression on $\ln(|\overline{y(t)}|)$ where $\overline{y(t)}$ is the extreme value points, assuming slope $\hat{k}$ and constant term $\hat{c}$ conforms to normal distributions.

$$ln(|y(t)|) = \hat{k} \cdot t + \hat{c} \tag{2.3.3}$$

In the 95% confidence interval,

$$\hat{k} = k \pm \sigma_k \tag{2.3.4}$$

Thus, for the best fit of damping constant value τ we obtain viscosity $\mu = -\frac{1}{5} k \rho R_0^2$ with error percentage $\pm \frac{\sigma_k}{k}$. Figure 2.3.2 represents a typical viscosity analysis for one segmentation of the

decaying sinusoid. The black curve shows the fitting for best damping constant, and two red curves show the boundaries of the fitting in 95% confidence interval.

$$\text{Damping constant: } \tau = -\frac{1}{\hat{k}}$$

$$\text{Viscosity: } \mu = -\frac{1}{5}(k \pm \sigma_k)\rho R_0^2 \qquad (2.3.5)$$

$$\text{Error in Viscosity Fitting: } \pm\frac{\sigma_k}{k} * 100\%$$

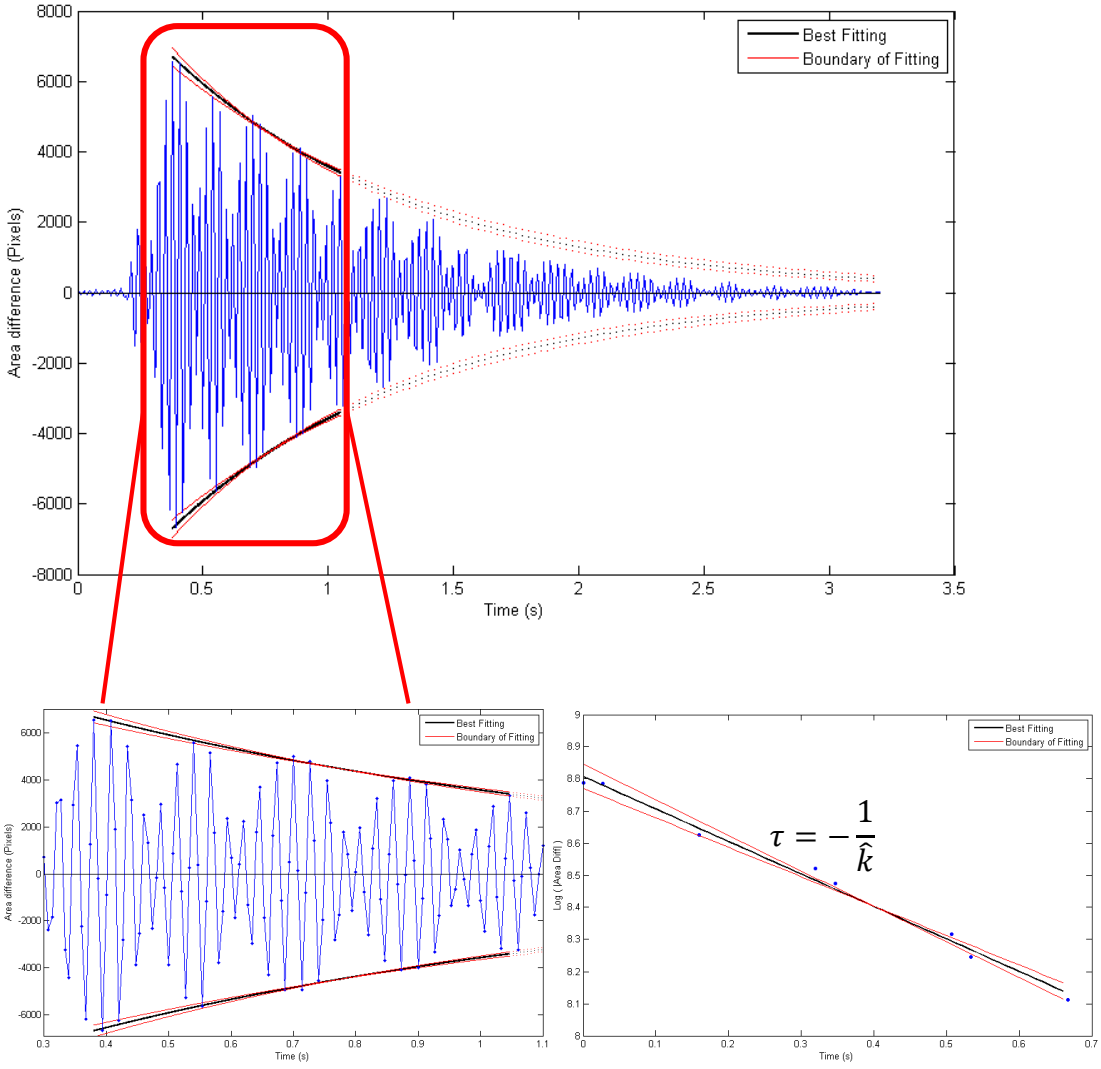

Figure 2.3.2: Preliminary Data fitting for damping constant

For oscillations at natural frequency around 37 Hz, approximately 40% of data points are selected to for the preliminary data fitting.

For each segmentation, a secondary data fitting is applied using all the data points (t_i, y_i) in the current segmentation, to find optimized damping constant τ and oscillation frequency f in Equation 2.3.2 minimizing the SSE defined as follows,

$$\text{Minimized SSE} = \frac{\sum||y(t_i)|-|y_i||}{\max(|y(t_i)|)} \tag{2.3.6}$$

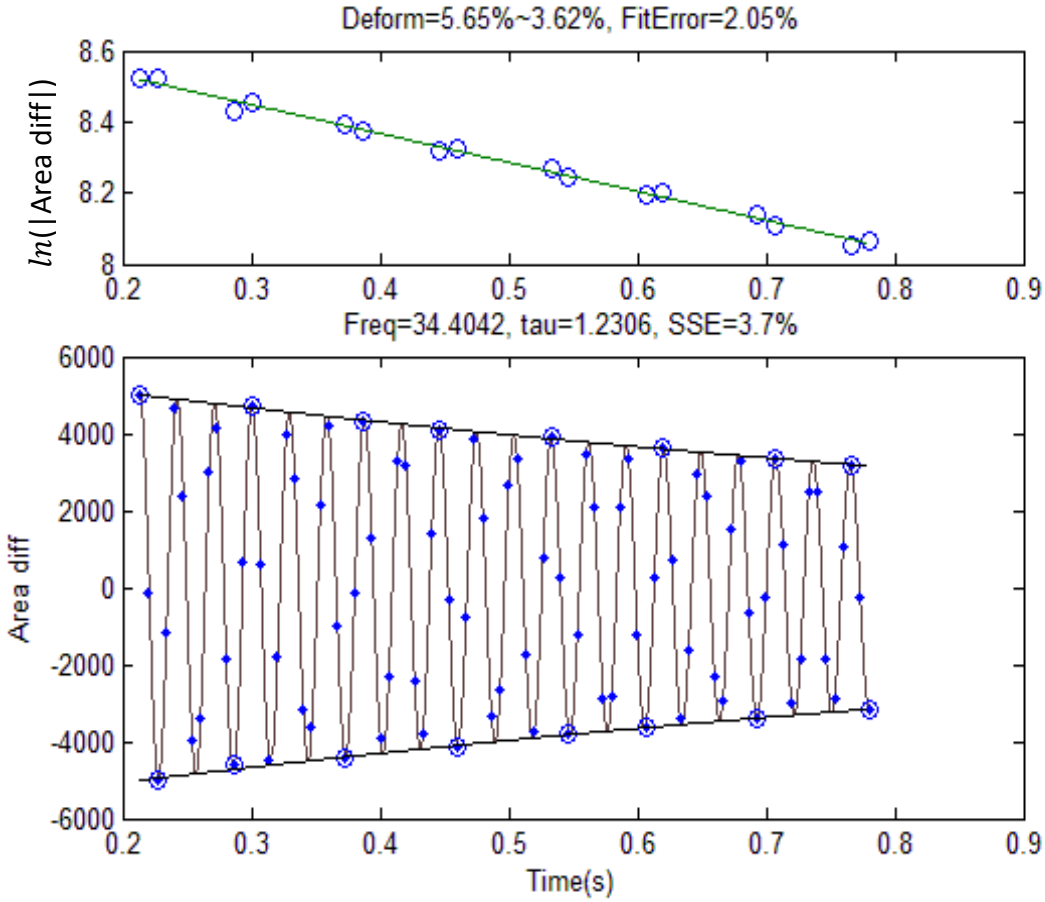

Figure 2.3.3: Secondary data fitting using all data points

2.3.3 Error in temperature range

The temperate range can be synchronized from pyrometer profiles based on the elapsed time of selected segmentation, as shown in Figure 2.3.1.

For each segmentation, the sample temperature has the following values,

$$\begin{aligned} &\text{Median Temperature: } \bar{T} = median(T) \\ &\text{Temperature range: } \Delta T = T_{max} - T_{min} \\ &\text{Error in Temperature: } \Delta T/400 * 100\% \end{aligned} \tag{2.3.7}$$

During a typical thermal cycle, the sample is usually superheated to 300 degrees above its molten temperature T_m, and undercooled to 100 degrees below T_m. The error percentage of temperature for each segmentation is approximated calculated as $\Delta T/400$.

Statistically, the fitting error of the damping constant and viscosity decreases as more data points are included in the regression as a results of diminishing the influence of arbitrary scattered and noisy data points while the temperature range would be larger due to wider time frame selected. A trade-off and optimization between errors in viscosity and temperature is necessary to be considered to keep balance between viscosity analysis quality and corresponding sample temperature precision.

In Figure 2.3.4, the errors in viscosity and temperature are represented together with the variable of number of frames or time steps. The two types of errors indicate opposite trends against the selected time frames, which intersect at around 100 frames for 150Hz data (0.67s). Thus, a reasonable range of time frames could be selected to moderate errors for both of viscosity and temperature.

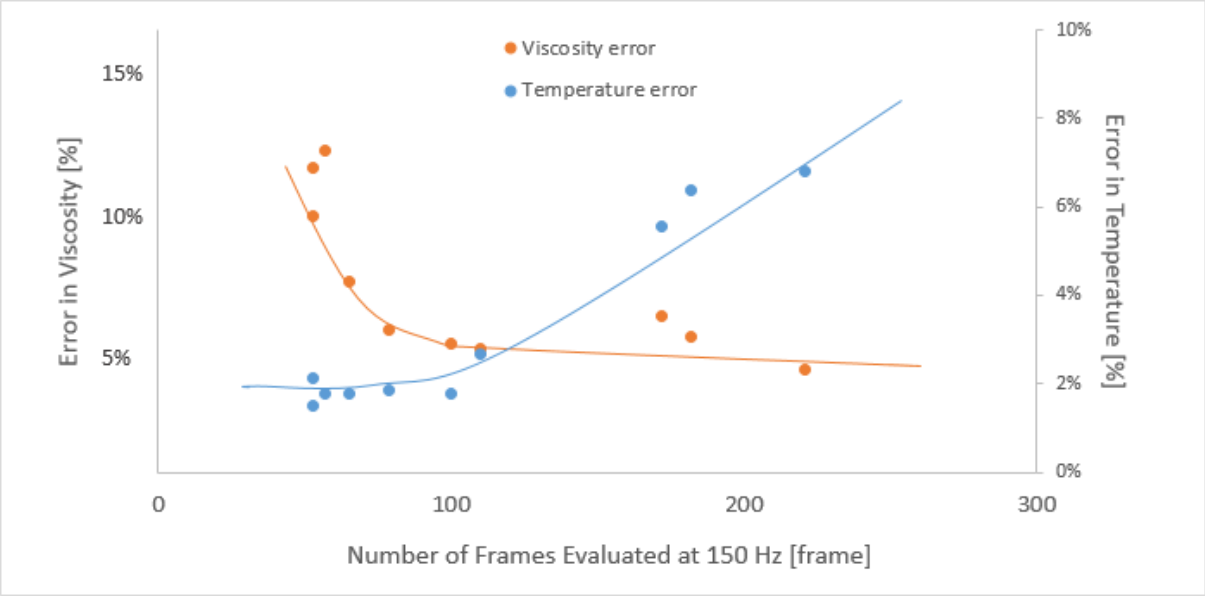

Figure 2.3.4: Trade-off between fitting errors in viscosity and temperature

2.3.4 Error in other factors

Background noises:

For each decaying oscillation excited by a pulse, the initial radius deformation of the sample is maximum at 4% - 9% depending on the sample's thermophysical properties and pulse size, and the deformation is expected to decrease and decay to 0% in the end. Actually, a 0.1% - 0.5% fluctuation error of the signal in the tail of the damped oscillation was observed as the background noise due to video data compression or exposure issues. For segmentations near the end of the oscillation where the radius deformation is less than 0.5%, the background noise could have significant influence on the viscosity analysis that would lead to invalid data fitting results; otherwise, the background noise has limited influence on the measurement.

Atmosphere:

During the testing, inert gas is fulfilled over the sample to limit evaporation. Both of Helium(He) and Argon(Ar) were used individually as the inert gas. As shown in Figure 2.3.5, the sample is exposed to He and Ar atmosphere in different tests, with cooling rate at 50K/s

and 20K/s separately, the results shows agreement of the viscosity analysis and indicate no significant influence of the atmosphere on the measurement.

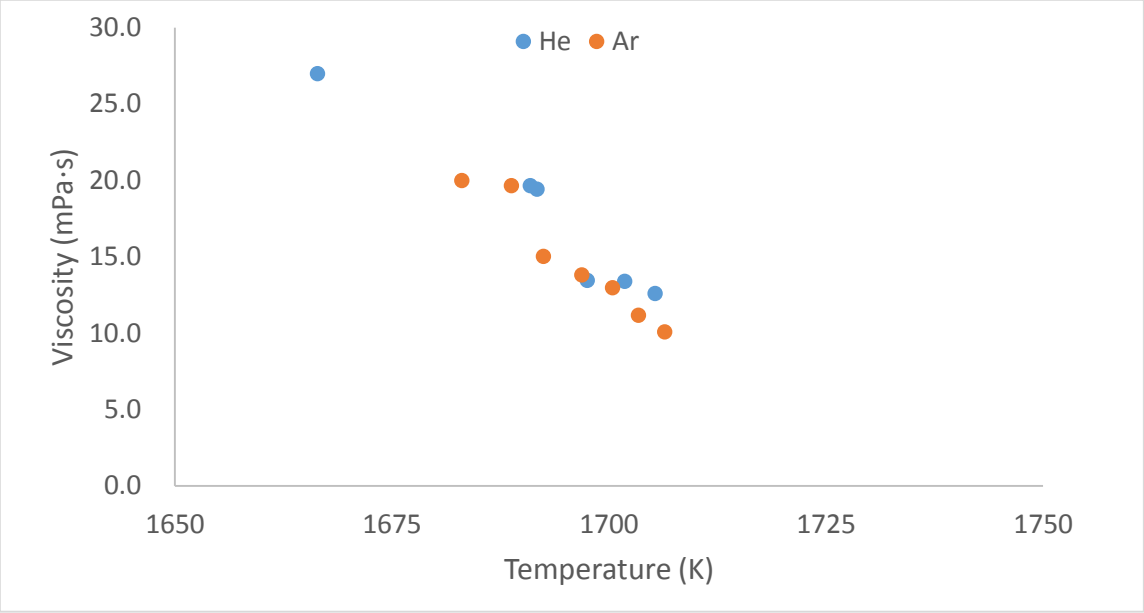

Figure 2.3.5: Helium/Argon atmosphere

3 Damped Oscillation Analysis

3.1 Preliminary Viscosity Analysis

During ISS EML experiment batch 1.2, several alloy compositions including $Fe_{72}Cr_{21}Ni_{19}$ at weight% (FeCrNi), LEK-94, and MC-2 were tested and performed oscillating droplet method and machine vision technique for viscosity measurement with pyrometer and high-speed camera system, which is described in the chapter 2. The excited oscillation is considered as mode $l = 2$ oscillation, and the viscosity is calculated from Equation 2.3.1 through fitting of the damping constant.

For each thermal cycle, the sample's temperature is decreasing at a known cooling rate following superheating, and the temperature-dependent shape is measured continuously during cooling. Preliminary analysis would show apparent viscosity over this temperature range.

Figure 3.1.1 shows an example of damping constant fitting for different segmentation in the same damped oscillation, and Figure 3.1.2 provides the time-temperature profile at the same time frame as the video, the vertical axis on left shows the cooling temperature vs. time, and the vertical axis on left shows the status of heater/pulse/positioner --- the positioner is normally kept at a constant voltage, and heater voltage is zero or at a less than 2 V moderate power setting except large pulse applied for 0.1 second to excite the sample. Corresponding to the synchronized elapsed time from pulse excitation, a relation between damping constant/viscosity and temperature will be established.

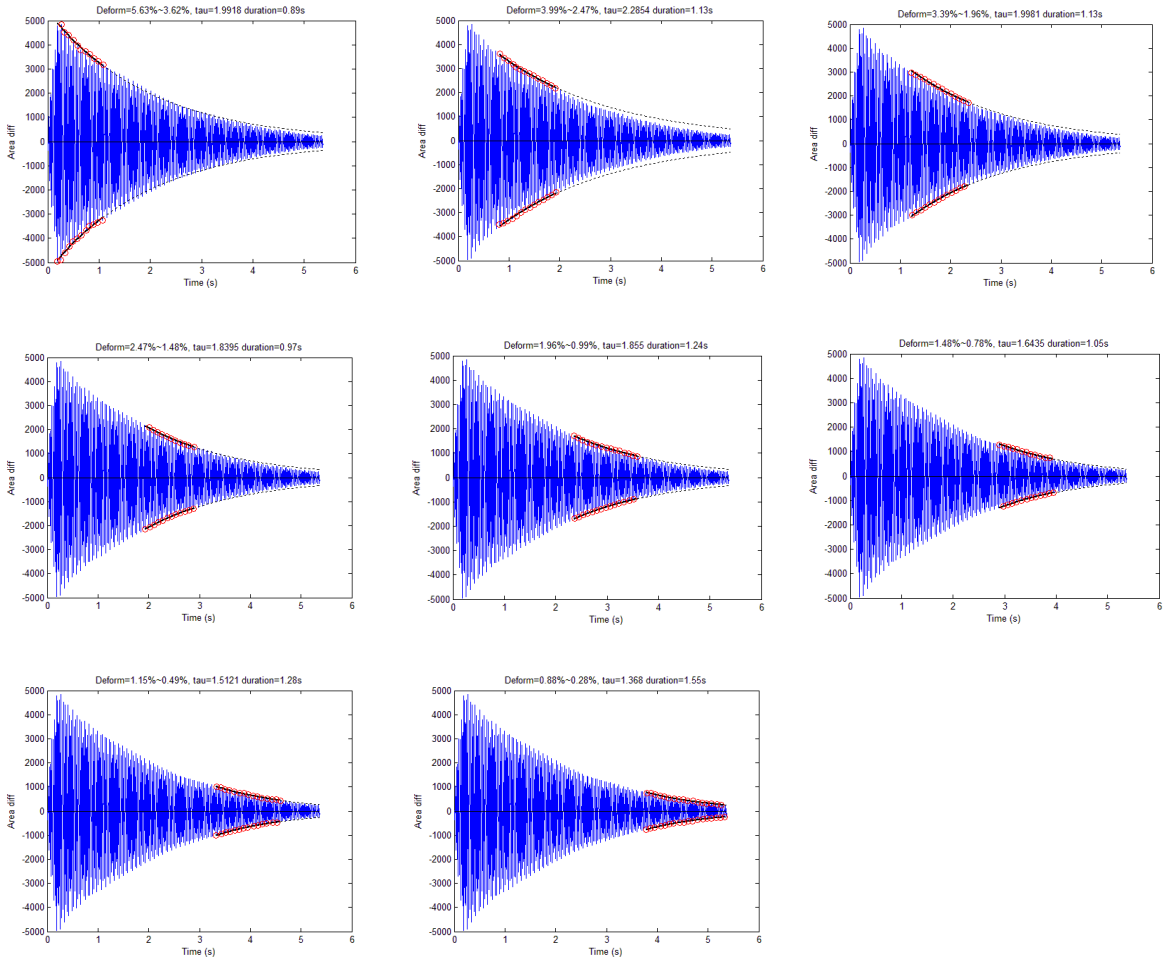

Figure 3.1.1: Damping constant measurement at successive segmentations

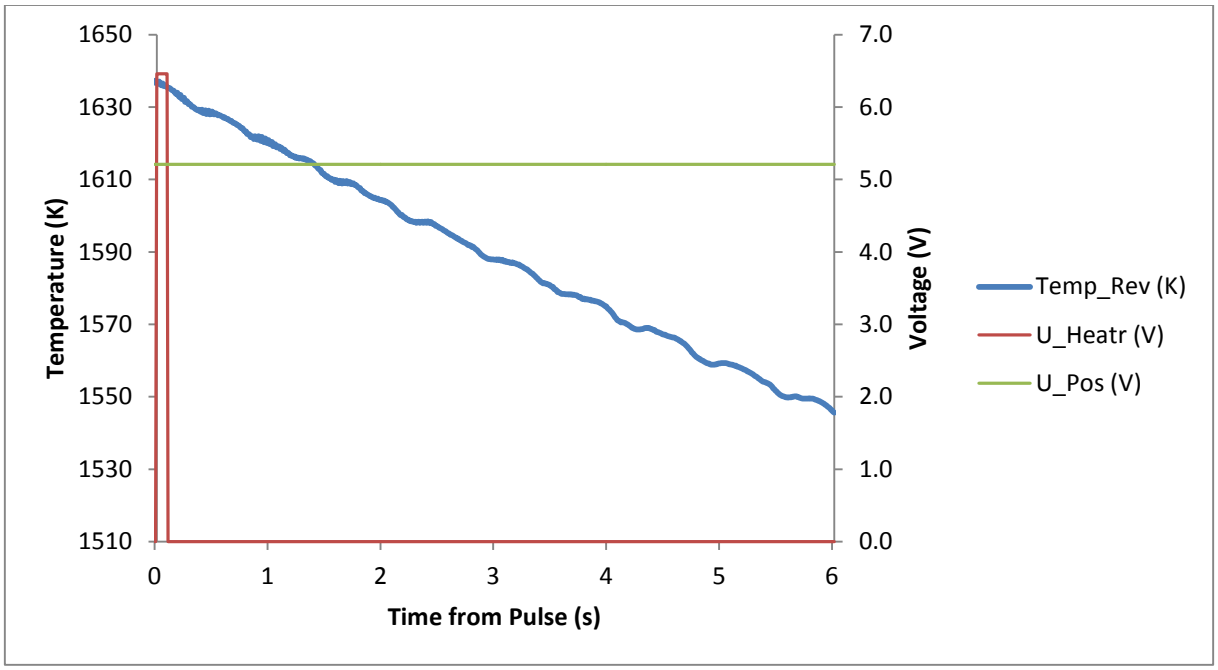

Figure 3.1.2: Time stamp synchronized pyrofile

3.2 Transition Behavior of Damped Oscillation

For each damped oscillation excited by a pulse, the preliminary analysis would show fitted damping constant as the function of temperature. Figure 3.2.1 represents a typical preliminary result where each data point stands for a segmentation in the oscillation signal, the error bar on the vertical direction shows the fitted error of damping constant as defined in Equation 2.3.5, and the error bar in the horizontal direction shows the testing temperature range near the median value for each segmentation. Figure 3.2.2 shows the corresponding viscosity values calculated from the damping constant.

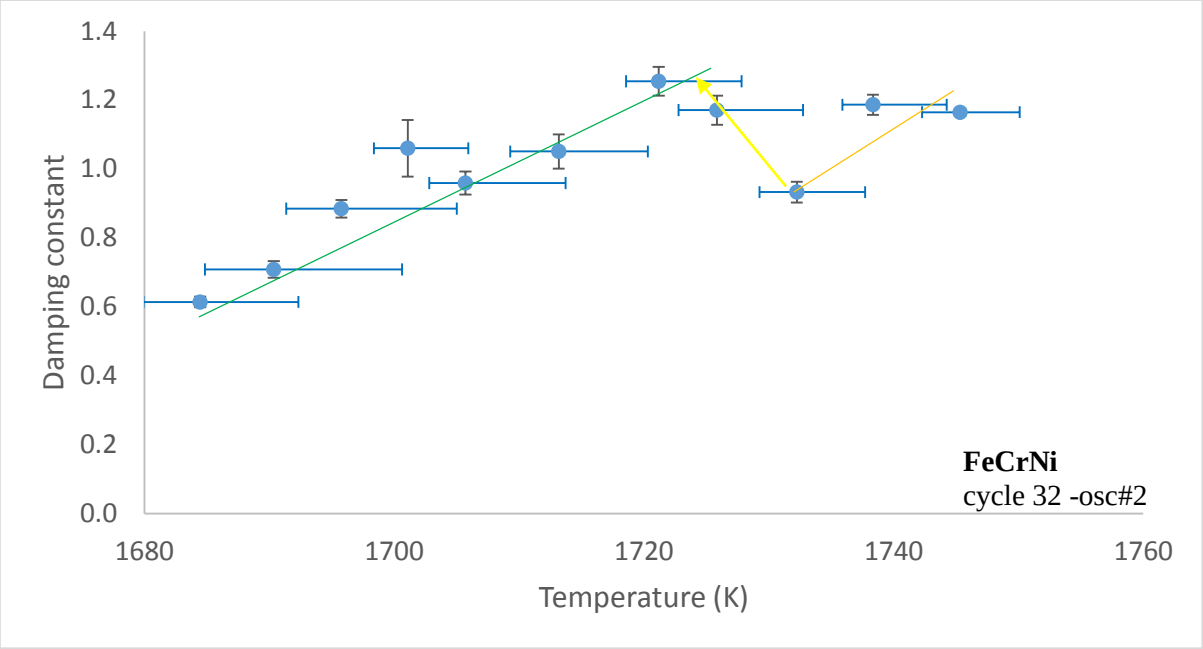

Figure 3.2.1: Damping constant vs. Temperature

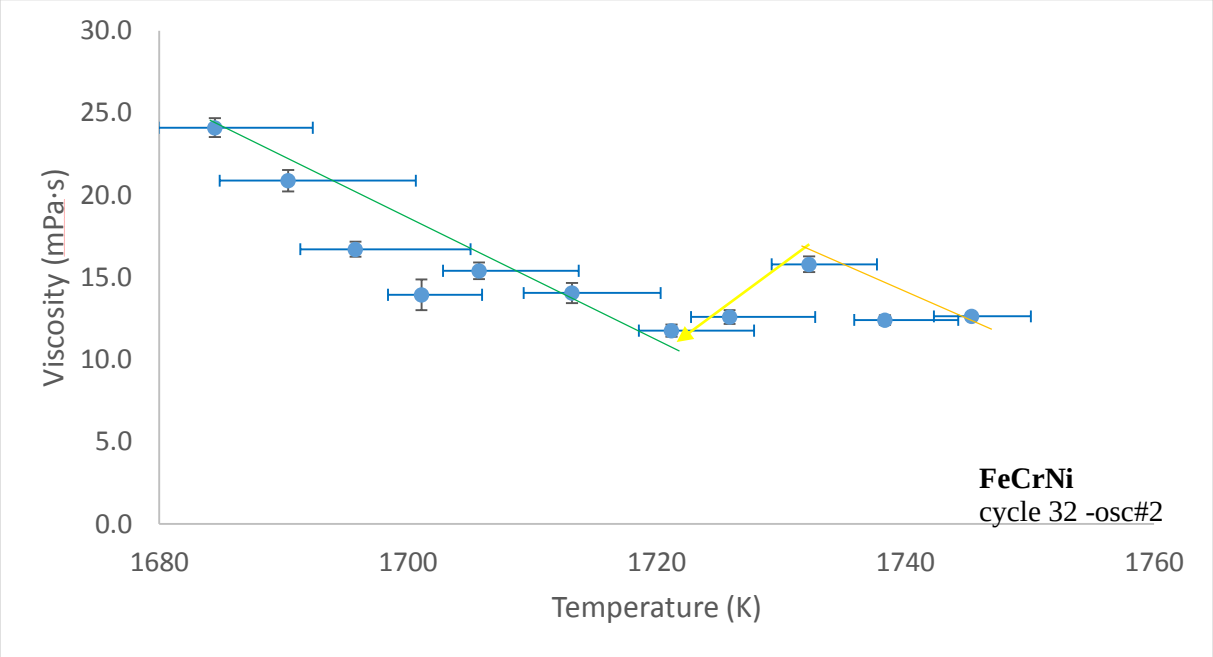

Figure 3.2.2: Apparent viscosity vs. Temperature

The molten alloy is expected to be more viscous at lower temperature, and the viscosity-temperature relation could be evaluated using an Arrhenius fit[8] in the form of,

$$\mu = e^{(\frac{C_1}{T} - C_2)} \tag{3.2.1}$$

Where μ is the dynamic viscosity, T is temperature, and $C_1,\ C_2 > 0$ is constant parameter.

For actual viscosity measurement in the ISS EML facility, the preliminary analysis would give apparent values due to the experimental parameter settings and limitation of camera capability. Unexpectedly, the measured apparent viscosity shows an increasing high apparent value near the beginning of a pulse excited oscillation which corresponds to the higher temperature region, and jumps to a relative low value in a short time. Values then increase again as the temperature decreases. This phenomenon can be universally observed for different alloy composition, testing temperature, and various heater/pulse power settings.

As shown in Figure 3.2.3, three different alloys including FeCrNi, LEK-94 and MC-2 was applied pulse excitation at various voltage to enable damped oscillation for viscosity measurement at different temperature, each showing a similar humped-increasing pattern at temperature from high to low, where the second half of the hump usually takes temperature change of 10-15K.

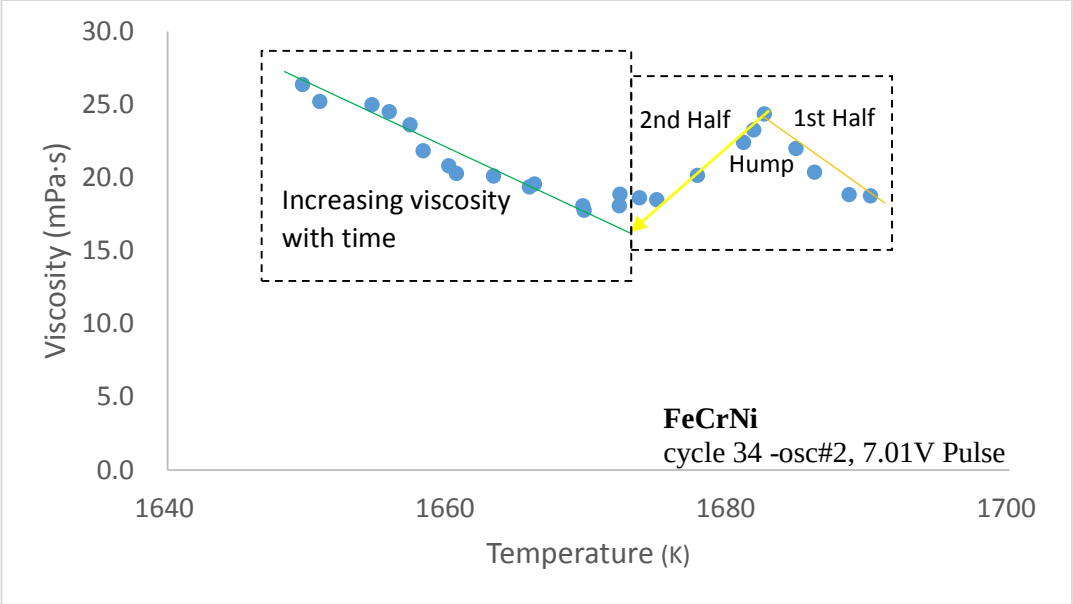
30.0
25.0
20.0
15.0
10.0
5.0
0.0
Viscosity (mPa·s)
1640
1660
1680
1700
Temperature (K)
Increasing viscosity
with time
2nd Half
1st Half
Hump
FeCrNi
cycle 34 -osc#2, 7.01V Pulse

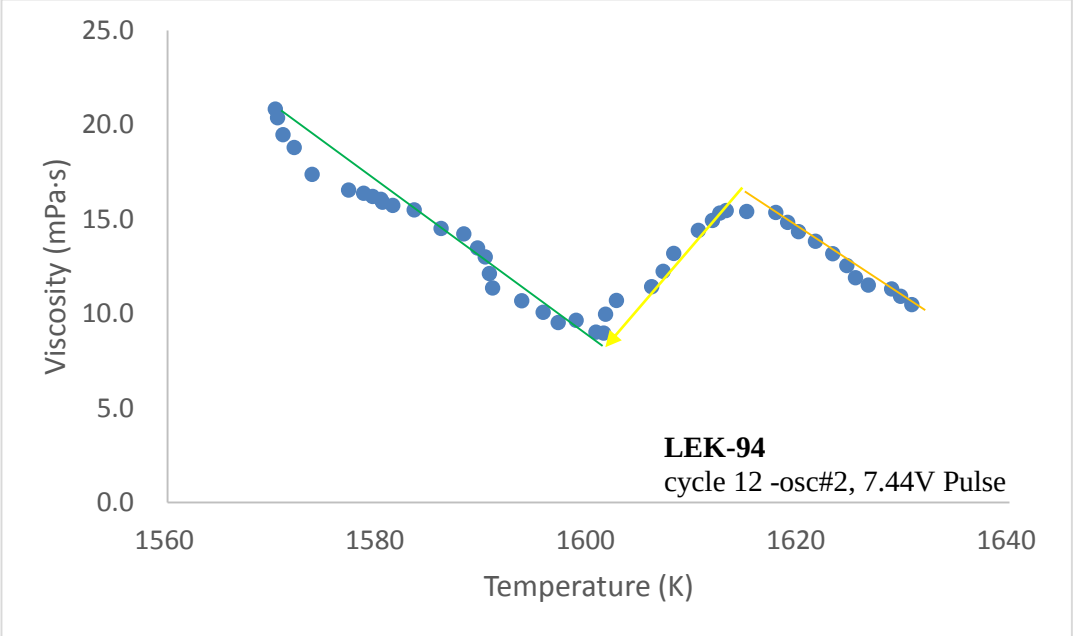
25.0
20.0
15.0
10.0
5.0
0.0
Viscosity (mPa·s)
1560
1580
1600
1620
1640
Temperature (K)
LEK-94
cycle 12 -osc#2, 7.44V Pulse

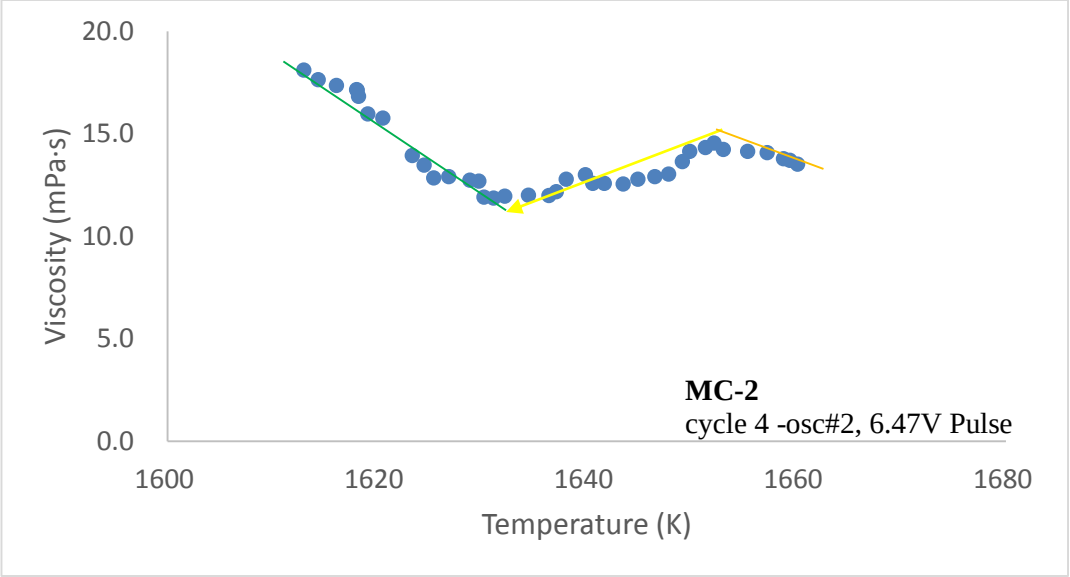

Figure 3.2.3: Measured apparent viscosity from preliminary analysis

The humped pattern can be divided into Phase-1 and Phase-2 regions. As shown in Figure 3.2.4, the apparent viscosity measured in phase-1 has a humped value as shown in Figure 3.2.3, and phase-2 is the region obtaining stable increasingly viscosity. In Phase-1, the first half of the hump indicates increased viscosity with decreased temperature, while the value is significantly higher than phase-2. For the second half of the hump, there is a transition between Phase-1 and Phase-2 as shown in Figure 3.2.4(b) and Figure 3.2.5, one segmentation in the damping constant analysis could usually take 0.5-1.5s corresponding to a 10-20K temperature change, thus with decreased temperature the fitted viscosity for segmentation across the higher apparent viscosity region Phase-1 and adjacent Phase-2 region with relatively lower viscosity value, would decrease as the portion of Phase-1 become less and Phase-2 become more for the damping constant fitting.

Thus, the Phase-1 and Phase-2 region could be explicitly defined as follows,

Beginning of Phase-1: The time of pulse application;

End of Phase-1/Beginning of Phase-2: The median timestamp within the segmentation that the measured apparent viscosity achieves a relatively low value and then subsequently starts to increase steadily;

End of Phase-2: The excited oscillation is damped out to levels obscured by noise.

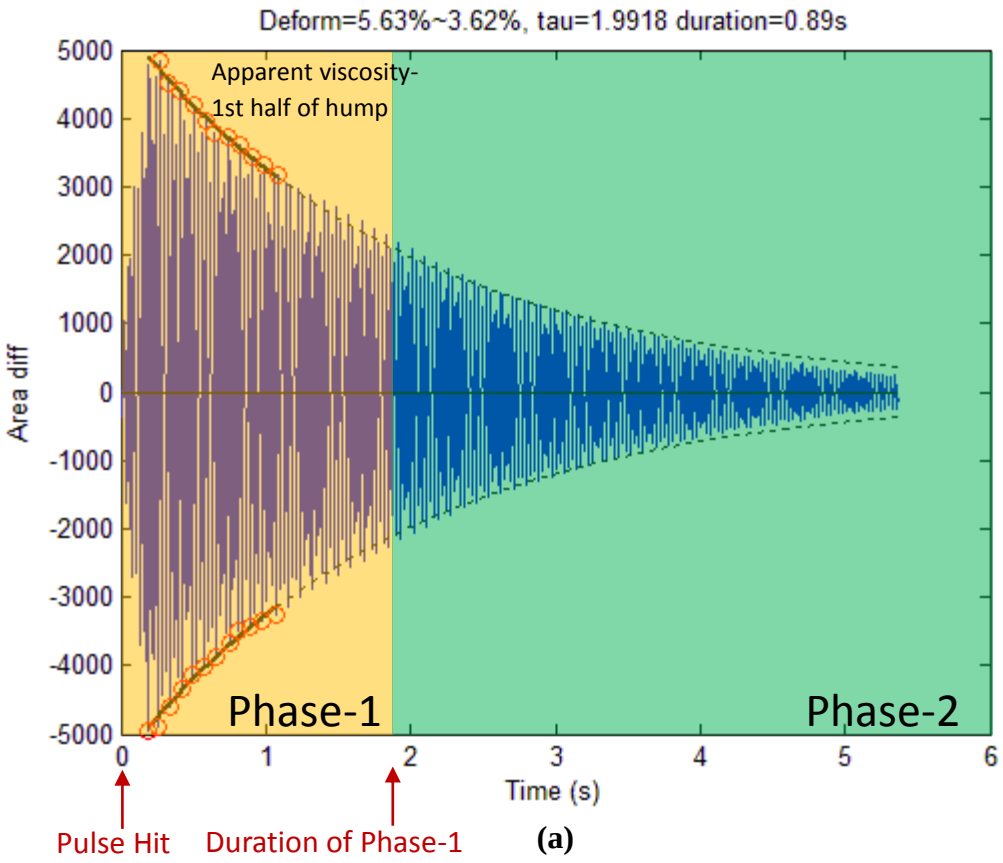
Deform=5.63%~3.62%, tau=1.9918 duration=0.89s
Apparent viscosity-
1st half of hump
Area diff
Time (s)
Phase-1
Phase-2
Pulse Hit
Duration of Phase-1

(a)

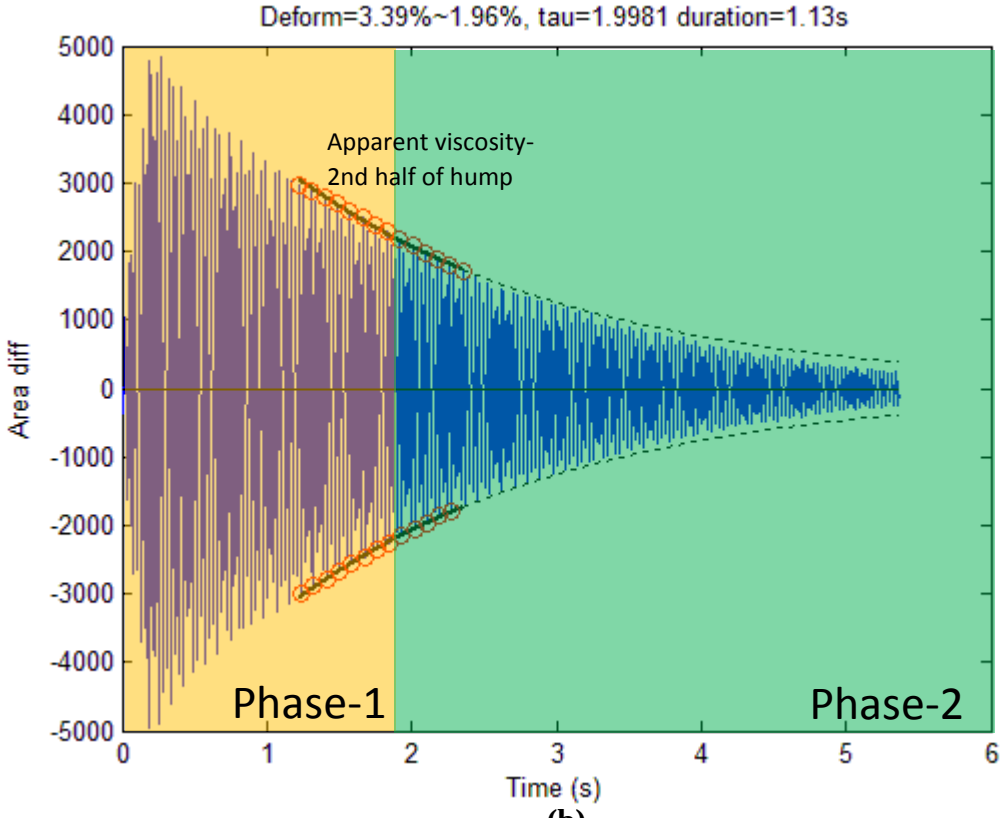
Deform=3.39%~1.96%, tau=1.9981 duration=1.13s
Apparent viscosity-
2nd half of hump
Area diff
Time (s)
Phase-1
Phase-2

(b)

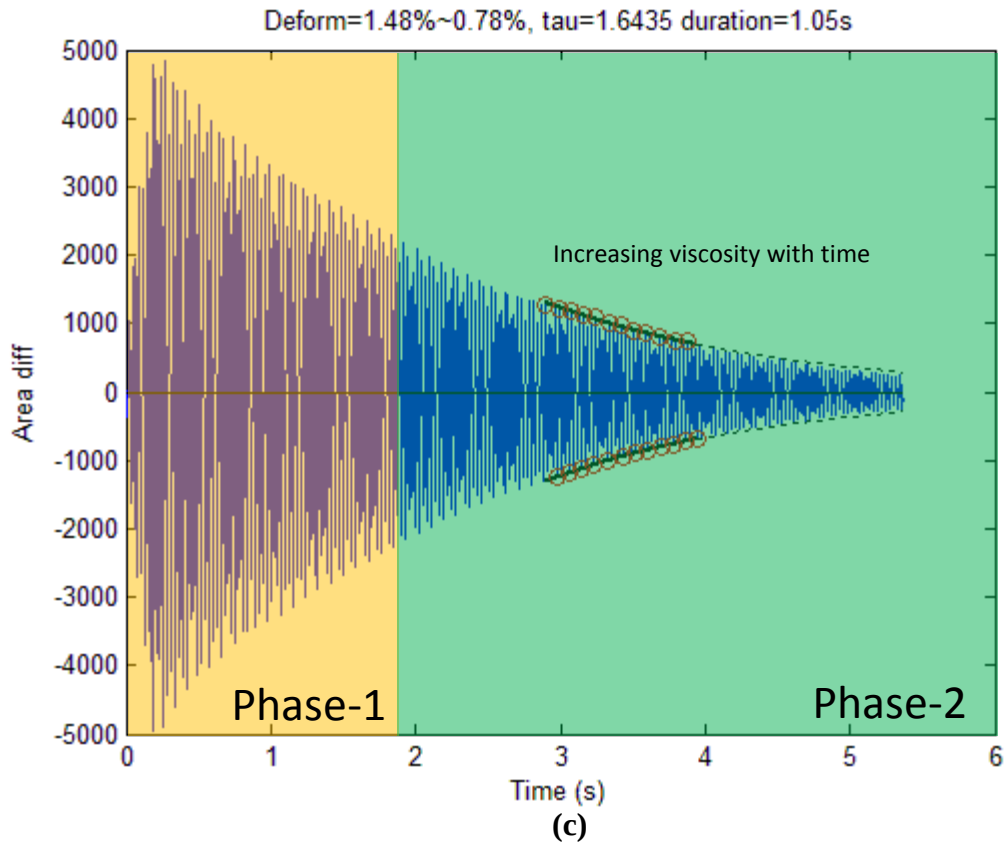

(c)

Figure 3.2.4: Phase-1 and Phase-2 region of pulse excited oscillation

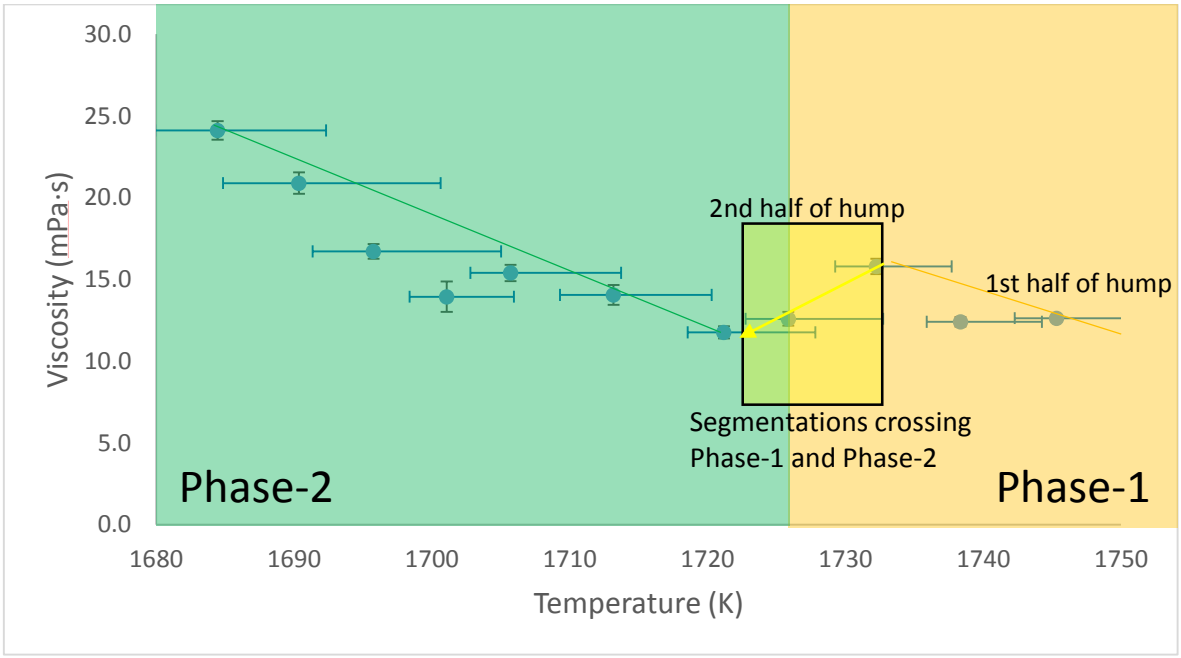

Figure 3.2.5: Phase-1 and Phase-2 region in viscosity analysis

3.3 Apparent Damping Analysis

3.3.1 Temperature and heater pulse settings

In the current oscillation drop method used in ISS EML, the heater pulse is necessary to excite the sample droplet to induce an oscillation that decays during viscosity measurement. During the thermal cycle, the positioner is maintained at constant voltage that has limited influence on the internal convective flow inside the droplet; the heater stays at 0V to larger than 2V to control the cooling rate of the sample, and the heater pulse is applied at levels between 5V to 9V for durations of 0.1 seconds to excite sample oscillation.

For constant heater less than 2V, the induced internal convection flow could be considered as laminar and has limited influence on the viscous damping; otherwise, turbulence could result with a concomitant increase in apparent viscosity. Stirring enhances eddy momentum transfer and hastens damping. Basically, 0.1 second of heater pulse is enough for the convection to develop turbulence, and a high apparent viscosity in the measurement is inevitable following the pulse application. The Phase-1 region with convective flow eventually slows and becomes laminar in Phase 2.

Conditions favoring an enhancement of Phase 1 occur for the sample at relatively high temperatures where the liquid is less viscous, or for application of large heater pulses to excite the sample. As shown in figure 3.3.1 for example, for LEK-94, a moderate 6.46V pulse was applied at superheated 156 K, and another large 8.42V pulse was applied at undercooled 33 K, either of which leads to a significantly high apparent viscosity from the preliminary analysis; the oscillation damped out before it could transition successfully to Phase-2. In both cases, the stirring induced under either high temperature or large pulse amplitude made the sample decay faster than the assumed duration of Phase-1, which could influenced by the viscous dissipation time scale. Further analysis regarding the MHD simulation of levitated molten droplets in the ISS EML facility quantitatively studied in Chapter 4 to show the relationship between internal convection condition and temperature/heater settings.

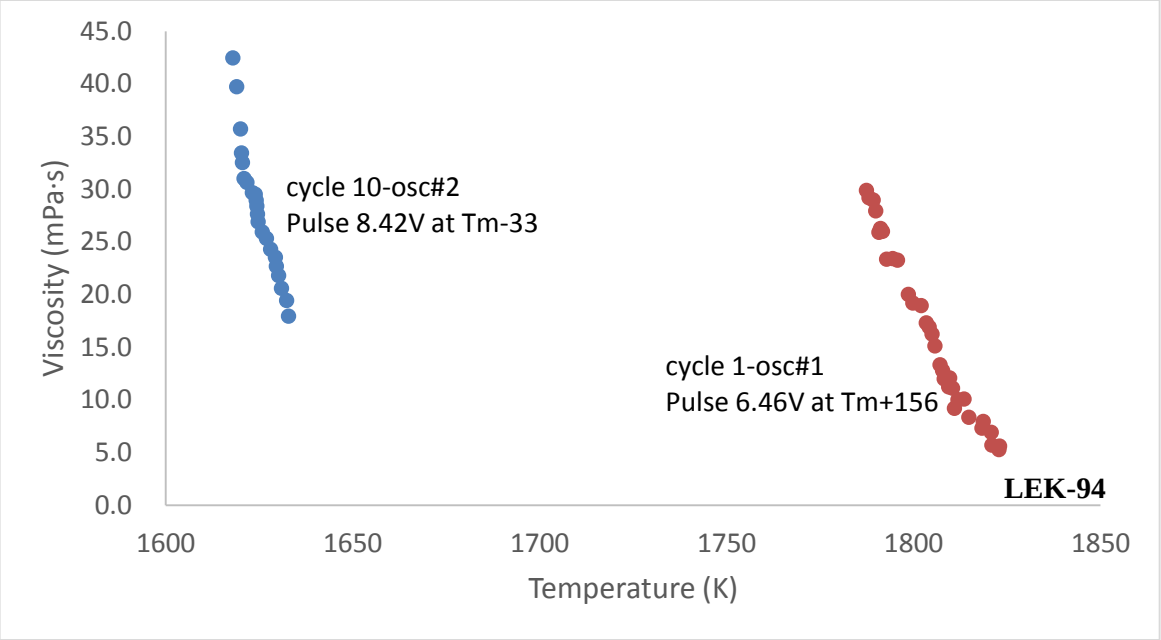

Figure 3.3.1: Apparent viscosity under high temperature/large pulse size

3.3.2 Magnitude of sample deformation

Following a pulse excitation, the sample is squeezed by the electromagnetic forces from the coil with forces primarily in the horizontal direction relative to the centerline of the coil. The sample will be deformed approximately into an ellipsoidal shape from the original spherical shape. The deformation achieves maximum extent immediately after the 0.1 second pulse is applied and released, and the initial deformation starts to decay from maximum to zero while the sample is oscillating freely. Based on the Top-view video reflecting the projection of the sample in the horizontal plane, define the degree of deformation as the ratio of initial length of maximum semi-axis R_1 derived in Equation 2.2.4 to the radius R_0 in the undeformed status,

$$\text{Maximum deformation\%: } \eta_0 = \frac{\max(R_1) - R_0}{R_0} \tag{3.3.1}$$

For the same sample, the degree of deformation would mainly rely on the pulse size. As shown in Figure 3.3.2 for tests of LEK-94, the initial deformation ranges from around 4% to 8%, which is increased with pulse set at 5.49V to 8.42V.

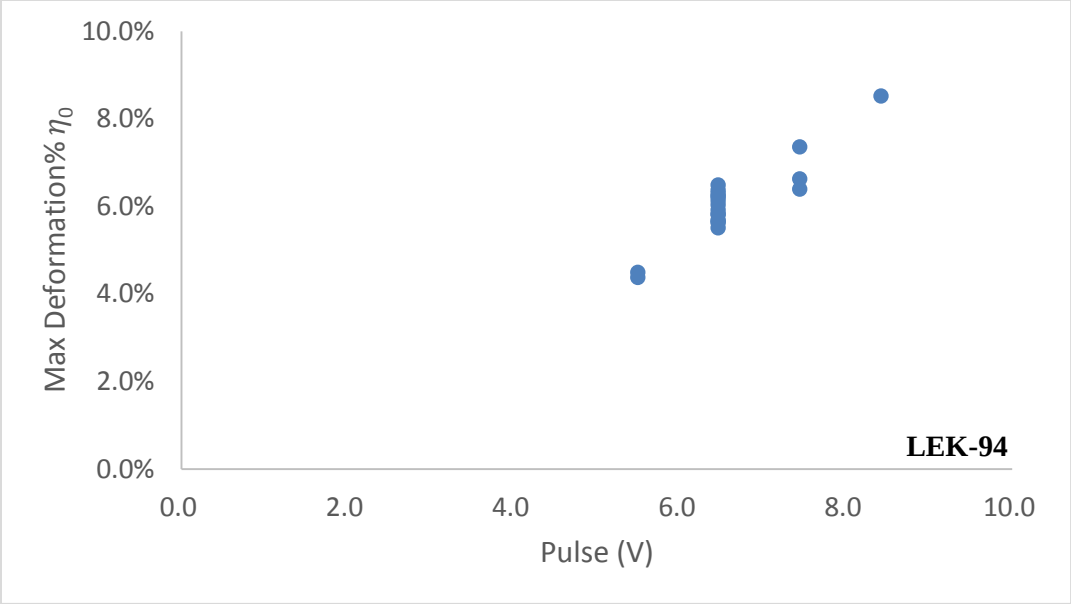

Figure 3.3.2: Maximum sample deformation vs. pulse size

For a viscous droplet which is oscillating with internal convection in the turbulent status, the degree of deformation of the sample would also impact the apparent viscosity. Etay et al. [17] utilized a pseudo-spectral method developed by Bojarevics et al. [49], to dynamically simulate the behavior of oscillating droplet with stirrings inside induced from alternating electromagnetic fields, which is governed by Navier-Stokes and k-ω turbulence equations.

While the droplet has more deformation, the distribution of effective viscosity inside the molten sample has higher intensity near the two poles that are perpendicular to the coil's centerline, and the sample's equator has lower effective viscosity. This unbalanced distribution sample with more deformation makes larger motion of the droplet near poles, and the droplet would damp faster than a sample with less deformation, thus presenting a higher value of apparent viscosity.

Etay *et al.* [17] defined a Relevant Reynolds number R_e^*, and an empirical formula estimating the measurement error was suggested based on the numerical simulation results,

$$R_e^* = 2\pi f \frac{\eta \rho {R_0}^2}{\mu} \tag{3.3.2}$$

$$\frac{\Delta\tau}{\tau} \approx 0.0036R_e + 0.1853 \quad \text{for} \quad {R_e}^* \leq 60 \tag{3.3.3}$$

Where $\frac{\Delta\tau}{\tau}$ is error of apparent damping constant to the theoretical value. For ${R_e}^*$ in the order of 10^2 to 10^3, $\frac{\Delta\tau}{\tau} \sim {R_e}^{*0.12}$; for ${R_e}^* > 10^3$, $\frac{\Delta\tau}{\tau} \gg 1$.

For molten FeCrNi with T_m=1715K, the suggested error of apparent viscosity $\frac{\Delta\tau}{\tau}$ and Relevant Reynolds Number ${R_e}^*$ is calculated as shown in Figure 3.3.3 and Figure 3.3.4. At the same temperature, the viscosity and density term is fixed and sample deformation η is dominated in Equation 3.3.2, measurement viscosity error $\frac{\Delta\tau}{\tau}$ is increased with larger deformation. For different temperatures, the deformation η corresponding to region with ${R_e}^* < 60$ allowing valid viscosity measurement is plotted in the shadowed area in Figure 3.3.4, and the suggested limits of deformation η vs. temperature are represented in Figure 3.3.5. Above the curve of limits in Figure 3.3.5, both deformation and viscosity dominate the Relevant Reynolds Number and therefore impact the viscosity evaluation; below the limits, the overestimation of apparent viscosity caused by deformation is acceptable, and only the viscosity term, which is inversely proportional to Relevant Reynolds Number, is the dominating factor.

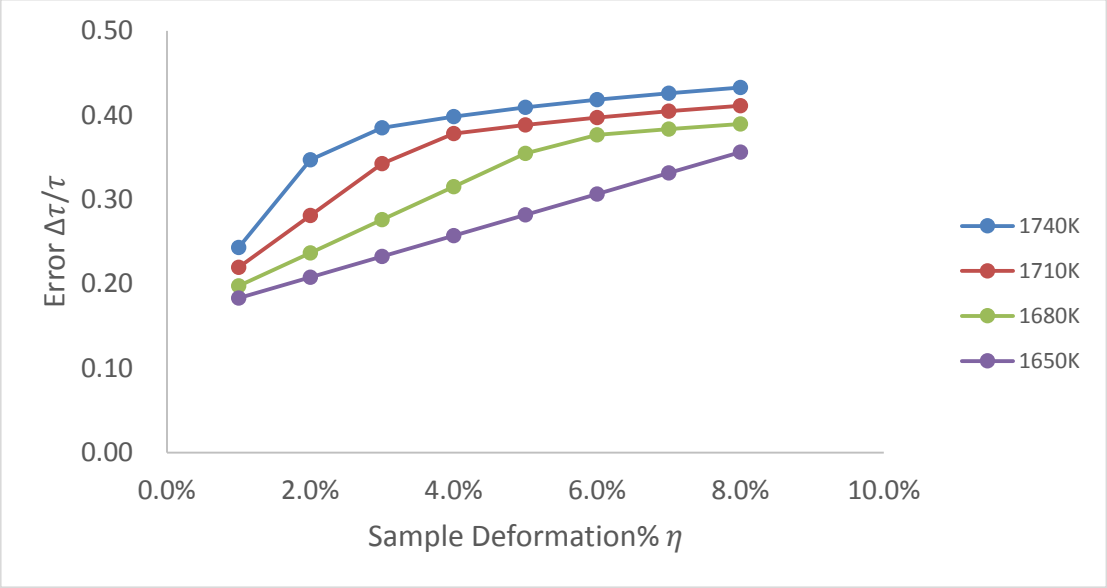

Figure 3.3.3: Error of apparent viscosity vs. sample deformation% for FeCrNi

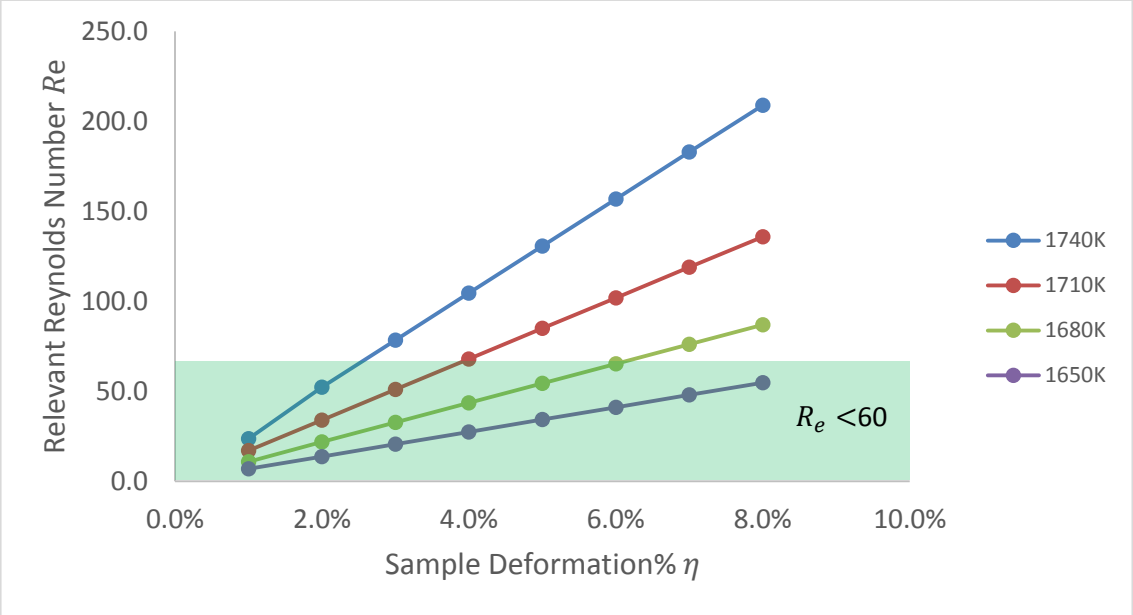

Figure 3.3.4: Relevant Reynolds Number vs. sample deformation% for FeCrNi

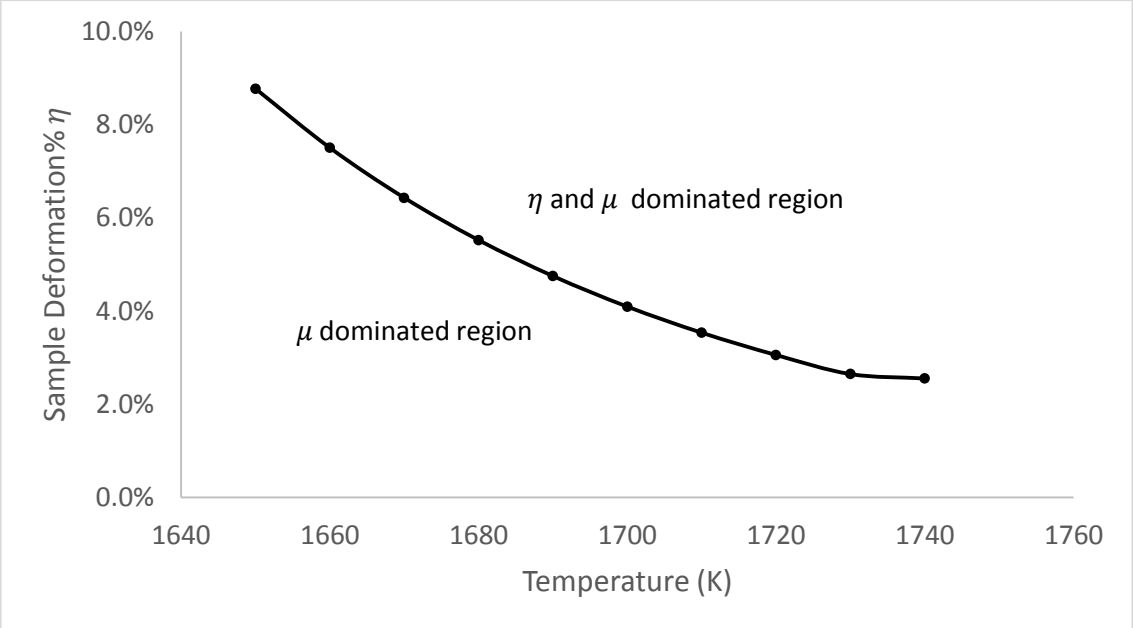

Figure 3.3.5: Deformation limits vs. temperature for FeCrNi

3.3.3 Oscillation modes

For an incompressible undeformed viscoelastic droplet of spherical shape with radius R_0, in the spherical coordinate (r, θ, φ), the sphere is defined as,

$$r(\theta, \varphi) = R_0 \tag{3.3.4}$$

Where r is the radial distance, θ is the polar angle ranges from 0 to π, and φ is the azimuth angle ranges from 0 to 2π.

When a deforming force is applied and released on the spherical droplet, the droplet will start to oscillate such that the oscillating frequency and damping rate are dependent on the surface tension and viscosity of the liquid. The relation between viscosity and damping is formulated in Equation 2.3.1. From Lamb's theory, the time-dependent deformed shape of the droplet can be described by the solution consisting of the superposition of a series of spherical harmonics where each representing a different oscillation mode[61], as follows,

$$r(t, \theta, \varphi) = R_0(1 + \sum_{\substack{l=1 \\ |m| \le l}}^{l=l_N} \varepsilon a_{l,m} Y_l^m(\theta, \varphi) e^{i\omega t - \frac{t}{\tau}}) \tag{3.3.5}$$

Where ε is a parameter representing a relative magnitude of the deformation[60], w is the oscillation frequency, τ is the damping constant, and $a_{l,m}$ is the proportion of each mode l subjected to $\sum a_{l,m}$=1.

$Y_l^m(\theta, \varphi)$ is the spherical harmonics in mode l and index m satisfying $|m| \le l$[62], usually $l_N \le 5$ in most cases.

$$Y_l^m(\theta, \varphi) = \sqrt{\frac{(2l+1)}{4\pi} \frac{(l-m)!}{(l+m)!}} P_l^m(\cos\theta) e^{im\varphi} \tag{3.3.6}$$

The spherical harmonics function is complete orthogonal and solved from classical Laplacian equation in the spherical form using separated-variable methods, which describes the oscillation behavior in both the θ and φ directions. It could be considered as an eigenfunction to the

eigenvalue problem of the Laplace operator where there are $2l+1$ eigenfunctions for each eigenvalue. In this circumstance, for each oscillation mode l, there are number of $2l+1$ types of oscillation behavior that the index m could be valued in the range$[-l,\ l]$.

In Equation 3.3.6, P_l^m is the associated Legendre functions; when m=0, P_l^m becomes the original l-th degree Legendre polynomial P_l,

$$P_l(x) = \frac{1}{2^l l!}\frac{d^l}{dx^l}(x^2-1)^l$$
$$P_l^m(x) = (-1)^m(1-x^2)^{\frac{m}{2}}\frac{d^m}{dx^m}P_l(x) \tag{3.3.7}$$

For the application of oscillating droplet, mode l=0 is independent of θ and φ which is not observed, mode l=1 describes the sample with pure translating movement, mode l=2 describes an oscillating sample subjected to deforming forces which reflects the real oscillation behavior of liquid droplet[36], as defined in Equation 3.3.8. For mode l=2, m=0, the oscillation is excited by a symmetric force, and the deformation is symmetric along the z-axis, usually for sample located in the centroid of the EML coil while the excitation pulse is applied; for mode l=2, m= ±1, the oscillation is excited by a shear force, and mirror symmetric about z-φ plane but the sample is deformed along the directions off the z-axis by an polar angle, which usually occurs for a sample located off the centerline of the coil or due to inhomogeneity introduced by a skewed coil; for mode l=2, m= ±2, the oscillation is similar to m= ±1, but has approximately twice the frequency and half the amplitude of m= ±1 and 0.2 times of the amplitude of m=0, which could be considered as lower order term in the overall oscillation defined in Equation 3.3.5. Thus, the oscillation mode l=2, m=0, ±1, which was also usually observed in the ISS EML experiments, is the dominating spherical harmonic that describes the oscillation behavior for the pulse excited sample experimentally.

$$Y_2^0(\theta,\varphi) = \sqrt{\frac{5}{4\pi}}\left(\frac{3}{2}cos^2\theta - \frac{1}{2}\right)$$

$$Y_2^{\pm 1}(\theta,\varphi) = \mp\sqrt{\frac{5}{24\pi}}3sin\theta cos\theta\ e^{\pm i\varphi} \tag{3.3.8}$$

$$Y_2^{\pm 2}(\theta,\varphi) = \sqrt{\frac{5}{96\pi}}3sin^2\theta\ e^{\pm 2i\varphi}$$

Thus, for oscillation of pure mode l=2, m=0,

$$r(t,\theta,\varphi) = R_0\left(1 + \varepsilon\sqrt{\frac{5}{4\pi}}\left(\frac{3}{2}cos^2\theta - \frac{1}{2}\right)e^{i\omega t - \frac{t}{\tau}}\right) \tag{3.3.9}$$

And for oscillation of pure mode l=2, m=±1,

$$r(t,\theta,\varphi) = R_0\left(1 \mp \varepsilon\sqrt{\frac{5}{24\pi}}3sin\theta cos\theta\ e^{\pm i\varphi}e^{i\omega t - \frac{t}{\tau}}\right) \tag{3.3.10}$$

Figure 3.3.6 and Figure 3.3.7 shows simulations of the sample deformation at continuously different time during single one oscillation period in mode l=2, m=0 and mode l=2, m=±1 separately. In each oscillation period, the sample droplet is initially a standard sphere which deforms consistently with the appropriate mode, and then reverts back to spherical shape at the end of the oscillation period.

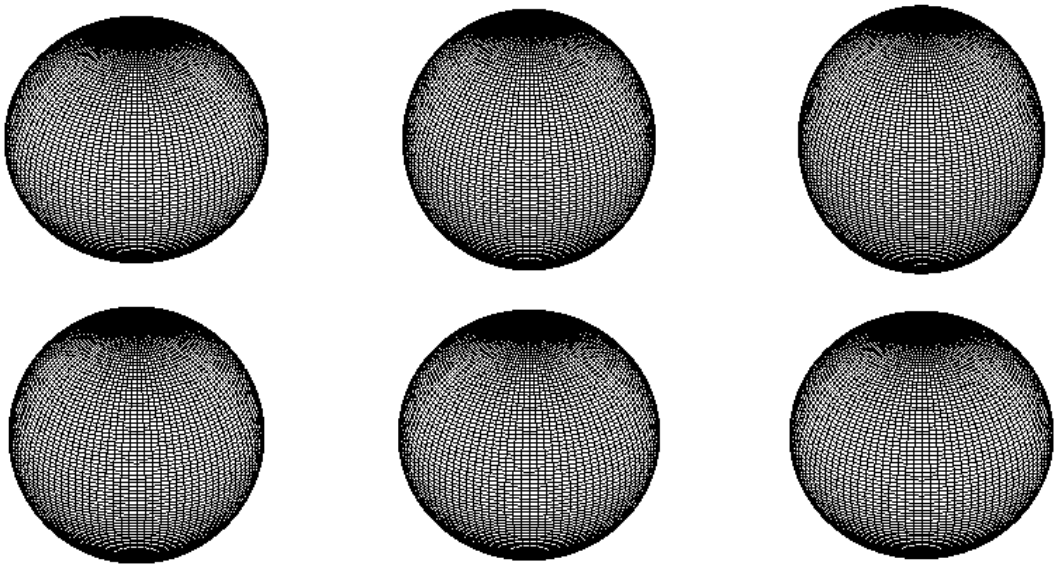

Figure 3.3.6: Oscillation mode l=2, m=0

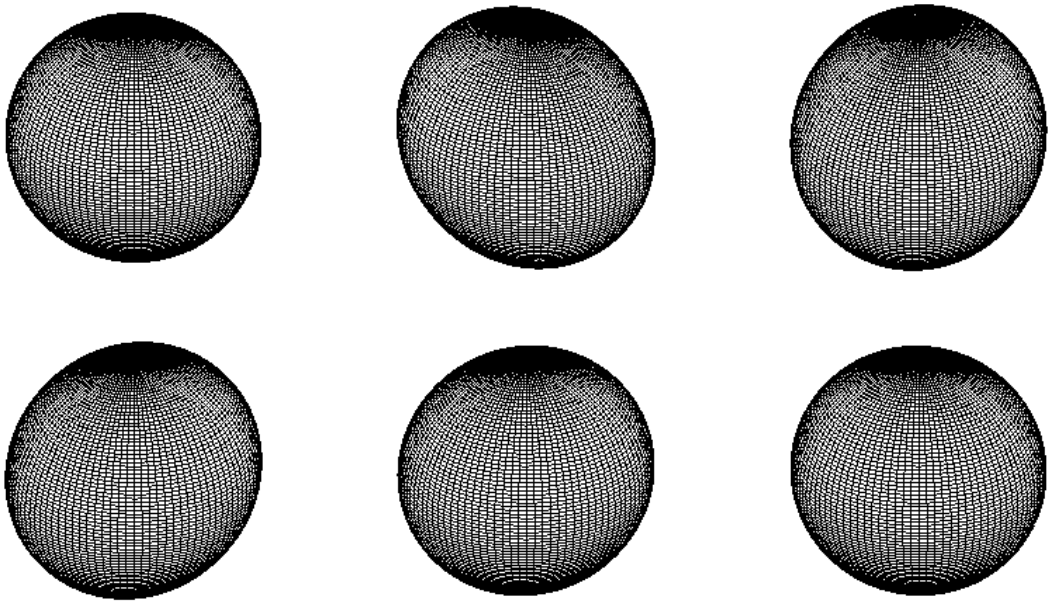

Figure 3.3.7: Oscillation mode l=2, m= ±1

In practice, the deformation of the damped oscillating sample is observed using the Top-view and Side-view cameras, which record the projection of the sample in the x-y plane and the x-z plane. The apparent damping constant/viscosity deformation is measured through an elliptical fitting of the projection that changes with time. When the oscillation has mixture of mode l=2, m=0, ±1, the measurement could be skewed from the theoretical damping constant τ defined in Equation 3.3.5. Thus, it is necessary to examine the skew factor of the measured values of two-dimensional projections to establish the true damping constant value.

For convenience, assume R_0 =1 in Equation 3.3.5, 3.3.9, and 3.3.10, and r becomes a dimensionless radius. In the Cartesian coordinates,

$$\begin{aligned} x &= r\,cos\varphi\,sin\theta \\ y &= r\,sin\varphi\,sin\theta \\ z &= rcos\theta \end{aligned} \tag{3.3.11}$$

And,

$$\begin{aligned} r &= \sqrt{x^2+y^2+z^2} \\ \theta &= \arccos\frac{z}{\sqrt{x^2+y^2+z^2}} \\ \varphi &= \arctan\frac{y}{x} \end{aligned} \tag{3.3.12}$$

Thus,

$$\begin{aligned} sin\,\theta &= \frac{\sqrt{x^2+y^2}}{\sqrt{x^2+y^2+z^2}} \\ cos\,\theta &= \frac{z}{\sqrt{x^2+y^2+z^2}} \end{aligned} \tag{3.3.13}$$

(i). For oscillation mode l=2, m=0, set $C_0 = \sqrt{\frac{5}{4\pi}}\varepsilon$, and Equation 3.3.9 can be rewritten as,

$$r = 1 + C_0\left(\frac{3}{2}cos^2\theta - \frac{1}{2}\right)e^{i\omega t-\frac{t}{\tau}} \tag{3.3.14}$$

In x-y plane where $\theta = \frac{\pi}{2}$, the cross section is bounded by a standard circle with equal radius,

$$R_{xy} = 1 - \frac{C_0}{2} \cos \omega t \, e^{-\frac{t}{\tau}} \tag{3.3.15}$$

In x-z plane where $\theta = 0$, the shape deformation has the maximum elongation/shortening along the z-axis,

$$R_z = 1 + C_0 \cos \omega t \, e^{-\frac{t}{\tau}} \tag{3.3.16}$$

Thus, the initial and maximum deformation is,

$$\begin{aligned} max\ R_x &= max\ R_y = 1 \mp \frac{C_0}{2} \\ max\ R_z &= 1 \pm C_0 \end{aligned} \tag{3.3.17}$$

For the maximum deformation η_0 defined in Equation 3.3.1, which is usually 4% to 10% in observation,

$$\eta_0 = \frac{C_0}{2} \approx 0.3154\varepsilon \tag{3.3.18}$$

Thus, the value of relative deformation magnitude ε is expected to be in the range from 0.12 to 0.32 in practice. The relation between ε and η_0 is shown in Figure 3.3.8.

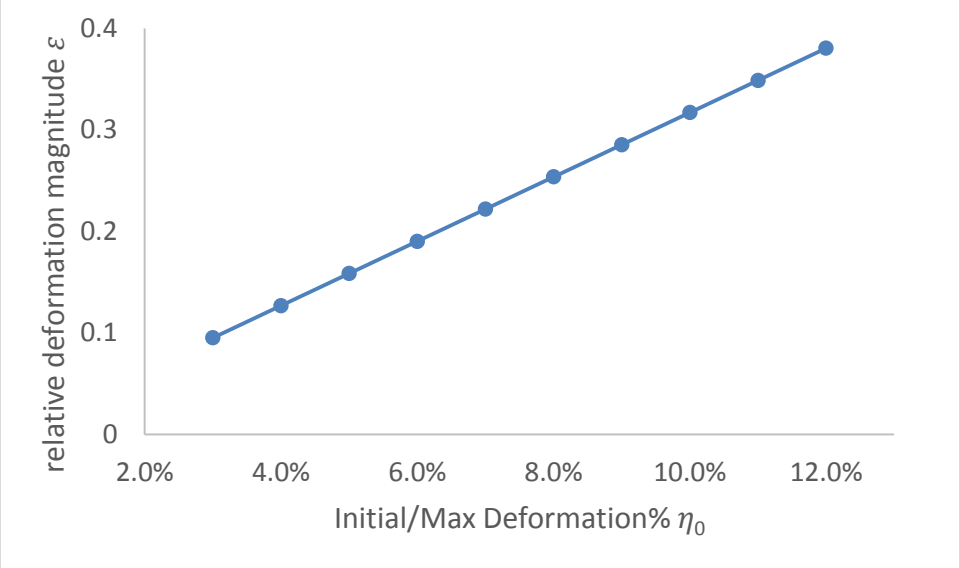

Figure 3.3.8: Relative deformation magnitude ε vs. deformation η_0

Convert the spherical coordinates to Cartesian coordinate:

In the x-y plane from Top-view, the projection of the sample is bounded by a circle,

$$\frac{x^2}{(1-\eta_0 \cos \omega t\, e^{-\frac{t}{\tau}})^2}+\frac{y^2}{(1-\eta_0 \cos \omega t\, e^{-\frac{t}{\tau}})^2}=1 \qquad (3.3.19)$$

In the x-z plane from Side-view where y=0, substitute Equation 3.3.13 into 3.3.14, the projection is bounded by the following closed curve,

$$\frac{x^2}{(1-\eta_0)R_{xz}}+\frac{z^2}{(1-\eta_0){R_{xz}}^2/(R_{xz}-3\eta_0)}=1 \qquad (3.3.20)$$

Where $R_{xz}=\sqrt{x^2+z^2} \in [1-2\eta_0,\ 1+2\eta_0]$.

Combine Equation 3.3.15 and 3.3.16, the ellipse with length of semi-axis R_x and R_z can be expressed as,

$$\frac{x^2}{(1-\eta_0 \cos \omega t\, e^{-\frac{t}{\tau}})^2}+\frac{z^2}{(1+2\eta_0 \cos \omega t\, e^{-\frac{t}{\tau}})^2}=1 \qquad (3.3.21)$$

Thus, the closed curve described by Equation 3.3.20 has the same form as Equation 3.3.21, and can be approximated by an ellipse while the deformation η_0 has a relatively small value. This indicates that the approach using an elliptical fit is valid in such circumstance. The error between the fitted ellipse area and actual projection area in the x-z plane is less than 5% for a deformation η_0<10%. Thus, for both Top-view and Side-view video, measurement of damping constant/viscosity deformations will obtain values indistinguishable from theory for an oscillation consisting only of mode l=2, m=0.

Based on the simulation, Figure 3.3.9 and 3.3.10 shows the projection of the oscillating sample in the x-y plane and the x-z plane separately, with an initial deformation η_0=6%. From the Top-view, the projection area changes from large to small then back and forth, while the projection in Side-view elongates in the x-axis and then the z-axis. After a certain period, the projections in both planes will be convergent to unit sphere when the oscillation is damped out.

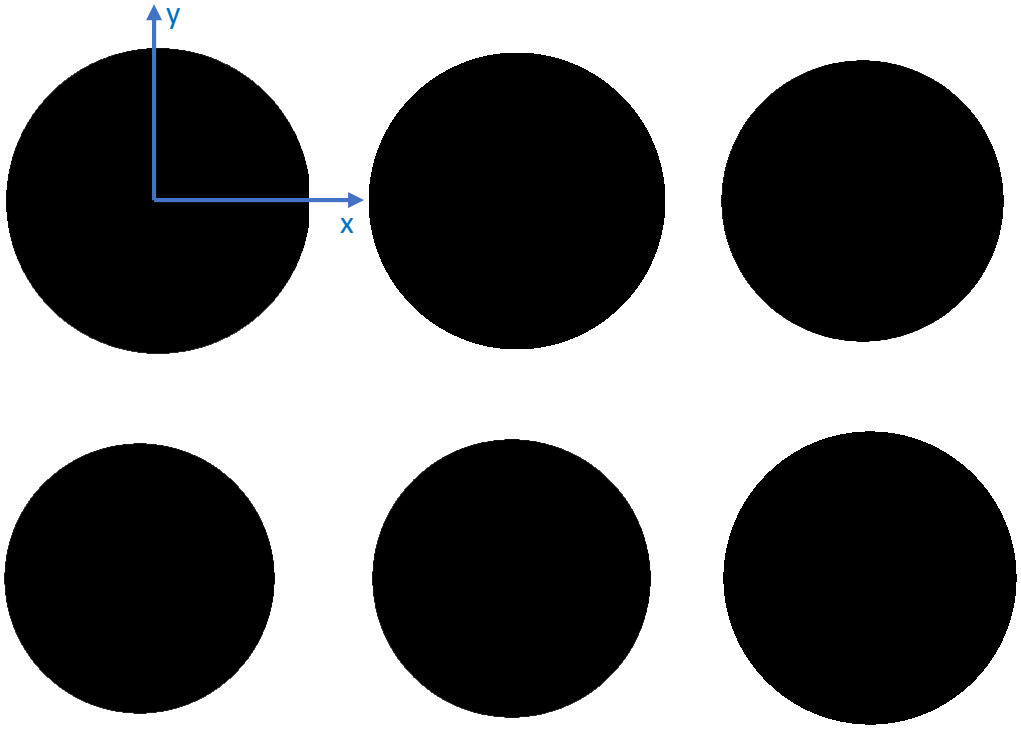

Figure 3.3.9: Oscillation mode *l*=2, *m*=0 projection in x-y plane (Top-view)

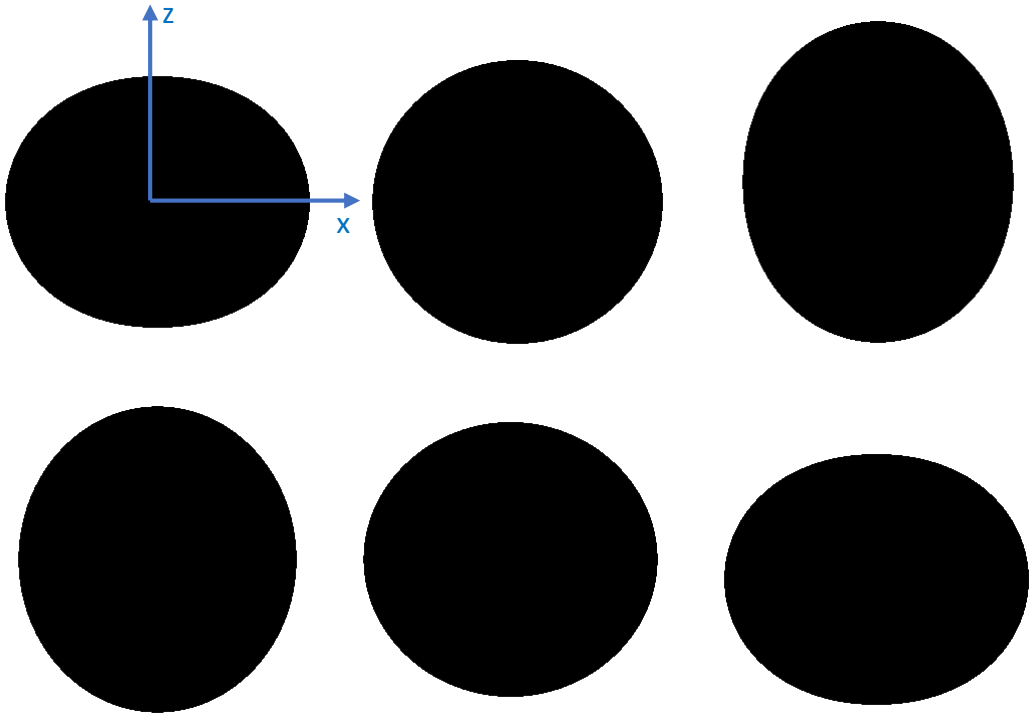

Figure 3.3.10: Oscillation mode *l*=2, *m*=0 projection in x-z plane (Side-view)

Define the length of maximum/minimum semi-axis for projection in the x-z plane as,

$$R_1 = \max(R_x, R_z) = \max(1 - \eta_0 \cos \omega t \, e^{-\frac{t}{\tau}}, 1 + 2\eta_0 \cos \omega t \, e^{-\frac{t}{\tau}})$$
$$R_2 = \min(R_x, R_z) = \min(1 - \eta_0 \cos \omega t \, e^{-\frac{t}{\tau}}, 1 + 2\eta_0 \cos \omega t \, e^{-\frac{t}{\tau}}) \quad (3.3.22)$$

For the x-y plane, the length of semi-axis equals the radius of circle,

$$R_1 = R_2 = R_{xy} = 1 - \eta_0 \cos \omega t \, e^{-\frac{t}{\tau}} \quad (3.3.23)$$

Figure 3.3.11 and 3.3.12 shows the converging R_1 and R_2 in the x-y plane and the x-z plane. The radius deformation in the x-z plane is twice of that observed in the x-y plane, which is expected from evaluation of Equation 3.3.17 due to the double elongation in the z-axis.

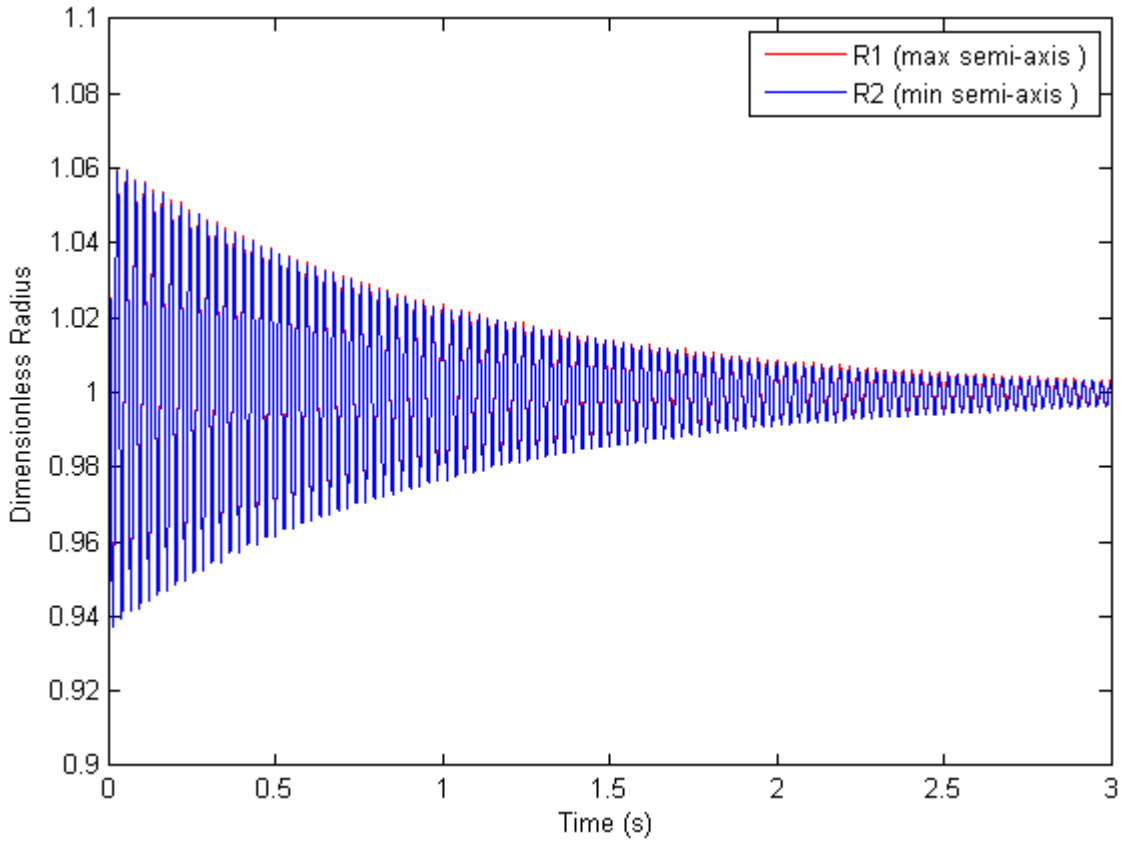

Figure 3.3.11: Damping under oscillation mode l=2, m=0 in x-y plane (Top-view)

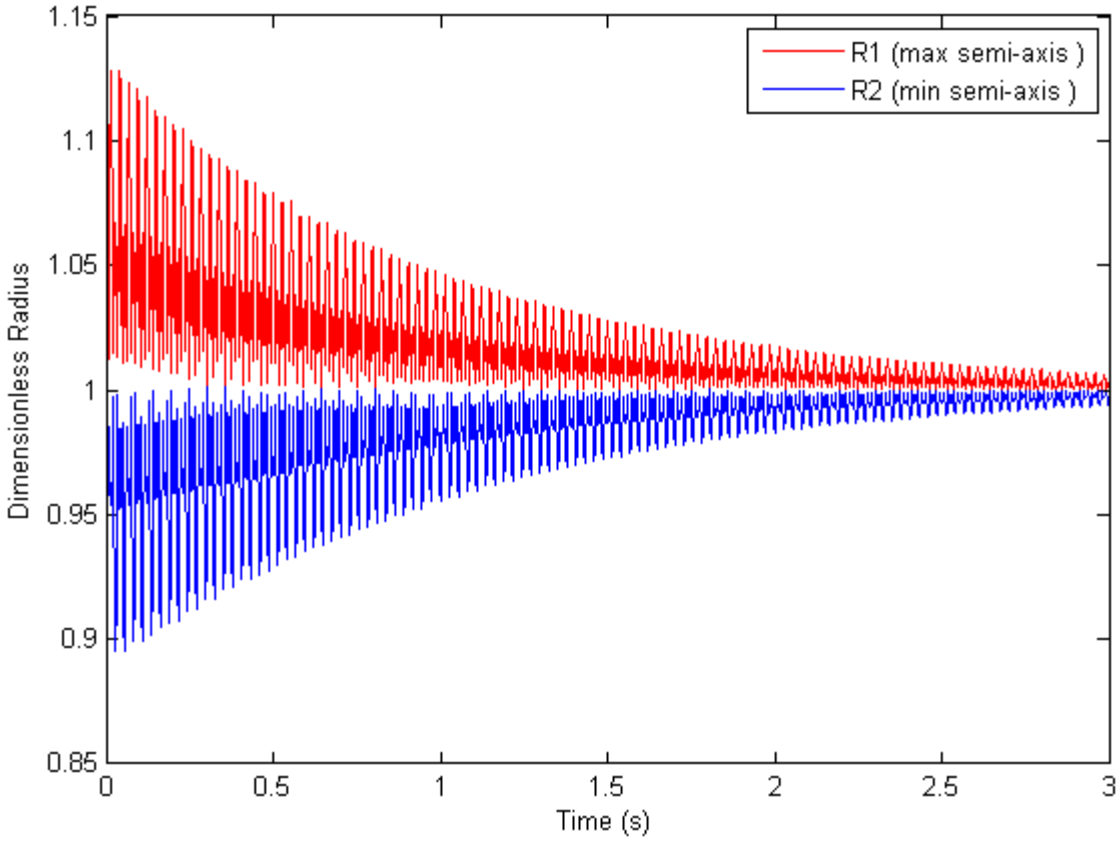

Figure 3.3.12: Damping under oscillation mode l=2, m=0 in x-z plane (Side-view)

(ii). For oscillation mode l=2, m=±1, set $C_1 = 3\sqrt{\frac{5}{24\pi}}\varepsilon = \sqrt{6}\eta_0$. Due to the symmetry, only m=1 is discussed here for convenience, and Equation 3.3.10 can be rewritten as,

$$r = 1 - C_1 \sin\theta \cos\theta \, e^{i\varphi} e^{i\omega t - \frac{t}{\tau}} \tag{3.3.24}$$

When the sample has the maximum deformation,

$$r = \sqrt{1 - C_1 \sin 2\theta \cos\varphi + \frac{{C_1}^2}{4}\sin^2 2\theta} \tag{3.3.25}$$

For projection in the x-z plane from Side-view where φ=0,

$$r = 1 - \frac{C_1}{2}\sin 2\theta \tag{3.3.26}$$

At $\theta = \pm\frac{\pi}{4}$, the sample has maximum/minimum radius,

$$\begin{aligned} \max R_1 &= 1 + \frac{C_1}{2} = 1 + \frac{\sqrt{6}\eta_0}{2} \\ \min R_2 &= 1 - \frac{C_1}{2} = 1 - \frac{\sqrt{6}\eta_0}{2} \end{aligned} \tag{3.3.27}$$

For any time at $\theta = \pm\frac{\pi}{4}$, the length of maximum/minimum semi-axis is,

$$\begin{aligned} R_1 &= \max(1 - \frac{\sqrt{6}\eta_0}{2}\cos\omega t\, e^{-\frac{t}{\tau}}, 1 + \frac{\sqrt{6}\eta_0}{2}\cos\omega t\, e^{-\frac{t}{\tau}}) \\ R_2 &= \min(1 - \frac{\sqrt{6}\eta_0}{2}\cos\omega t\, e^{-\frac{t}{\tau}}, 1 + \frac{\sqrt{6}\eta_0}{2}\cos\omega t\, e^{-\frac{t}{\tau}}) \end{aligned} \tag{3.3.27}$$

In the Cartesian coordinates where y=0, substitute Equation 3.3.13 into 3.3.26, the projection is bounded by the following closed curve, where $R_{xz} = \sqrt{x^2 + z^2} \in [R_2,\ R_1]$.

$$\frac{x^2 + z^2}{R_{xz}} + \frac{zx}{{R_{xz}}^2/\sqrt{6}\eta_0} = 1 \tag{3.3.28}$$

While $\cos\omega t \geq 0$, $R_1 = 1 + \frac{\sqrt{6}\eta_0}{2}\cos\omega t\, e^{-\frac{t}{\tau}}$ and $R_2 = 1 - \frac{\sqrt{6}\eta_0}{2}\cos\omega t\, e^{-\frac{t}{\tau}}$. Consider an ellipse with semi-axis R_1 and R_2 in the x'-z' coordinates as shown in Figure 3.3.13.

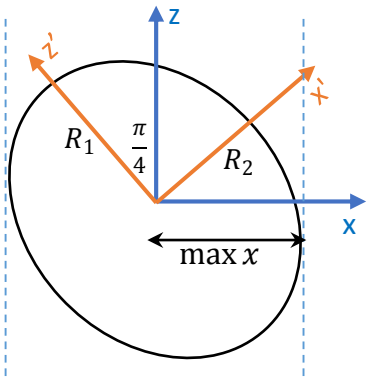

Figure 3.3.13: Ellipse Rotated by angle of $\frac{\pi}{4}$

The equation of the ellipse in the x'-z' coordinates is,

$$\frac{x'^2}{(1-\frac{\sqrt{6}\eta_0}{2}\cos\omega t\, e^{-\frac{t}{\tau}})^2}+\frac{z'^2}{(1+\frac{\sqrt{6}\eta_0}{2}\cos\omega t\, e^{-\frac{t}{\tau}})^2}=1 \tag{3.3.29}$$

With rotation of the coordinate by $\pi/4$,

$$\begin{bmatrix}x'\\z'\end{bmatrix}=\begin{bmatrix}\cos\pi/4 & \sin\pi/4\\-\sin\pi/4 & \cos\pi/4\end{bmatrix}\begin{bmatrix}x\\z\end{bmatrix} \tag{3.3.30}$$

Hence, the equation of the ellipse in the x-z coordinates can be expressed as,

$$\frac{x^2+z^2}{[1-(\frac{\sqrt{6}\eta_0}{2}\cos\omega t\, e^{-\frac{t}{\tau}})^2]^2/[1+(\frac{\sqrt{6}\eta_0}{2}\cos\omega t\, e^{-\frac{t}{\tau}})^2]}+\frac{zx}{[1-(\frac{\sqrt{6}\eta_0}{2}\cos\omega t\, e^{-\frac{t}{\tau}})^2]^2/2\sqrt{6}\eta_0\cos\omega t\, e^{-\frac{t}{\tau}}}=1 \tag{3.3.31}$$

Thus, the closed curve described by Equation 3.3.31 has the same form as and could be approximated to the Equation 3.3.28 of ellipse, for small η_0. The error between fitted ellipse area and actual projection area in x-z plane is less than 7% for deformation η_0<10%.

For projections in the x-y plane from Top-view, the radius in y-axis is constant at $\theta=\frac{\pi}{2}$,

$$R_y=r(t,\frac{\pi}{2},\varphi)=1 \tag{3.3.32}$$

The radius in the x-axis has the same value of $\max x$ solved from Equation 3.3.31 which is also shown in Figure 3.3.13. Using the method of Lagrange multipliers,

$$\begin{aligned}&Maximize\ f(x,z)=x\\&s.t.\ g(x,z)=0\end{aligned} \tag{3.3.33}$$

Where the constraint $g(x,z)$ is defined from Equation 3.3.31.

The Lagrange function is defined as,

$$L = f + \lambda g$$
$$s.t.\ \frac{\partial L}{\partial x} = 0,\ \frac{\partial L}{\partial z} = 0,\ \frac{\partial L}{\partial \lambda} = 0 \tag{3.3.34}$$

The maximum x can be found as,

$$R_x = \max x = \sqrt{1 + \frac{\sqrt{6}\eta_0}{2} \cos \omega t\, e^{-\frac{t}{\tau}}} \tag{3.3.35}$$

Thus, the projection of the sample in the x-y plane is approximately bounded by an ellipse as shown in Figure 3.3.14, with length of maximum/minimum semi-axis as follows,

$$R_1 = R_x = \sqrt{1 + \frac{\sqrt{6}\eta_0}{2} \cos \omega t\, e^{-\frac{t}{\tau}}}$$
$$R_2 = R_y = 1 \tag{3.3.36}$$

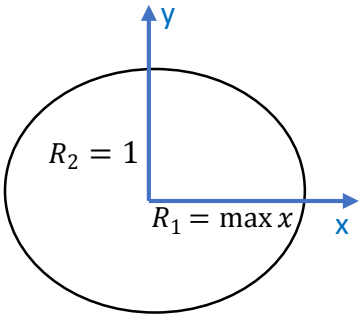

Figure 3.3.14: Ellipse projected in x-y plane for mode l=2, m=±1

As shown in Figure 3.3.15–3.3.16 and Figure 3.3.18–3.3.19, for the sample projection in the x-y plane from Top-view with initial η_0=6%, the deformation regarding to R_1 is limited and decreased monotonously; from Side-view, the oscillating sample is deformed along the x'-axis and z'-axis in the directions of $\theta = \pm\frac{\pi}{4}$. Both damped out and converges to the standard sphere for a certain decaying time.

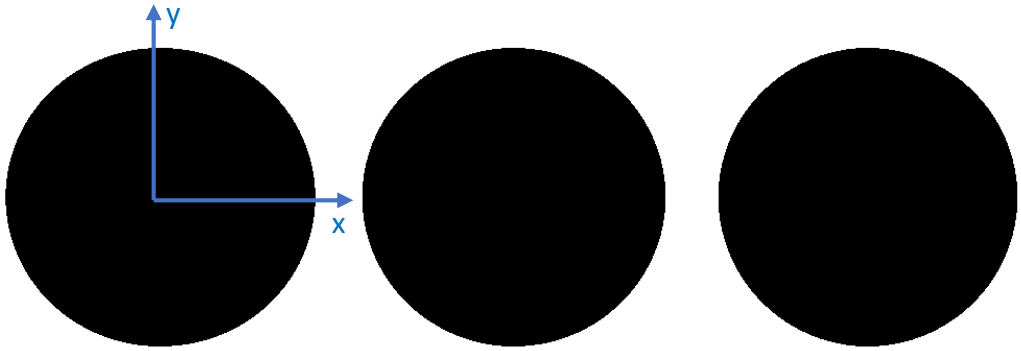

Figure 3.3.15: Oscillation mode l=2, m= ±1 projection in x-y plane (Top-view)

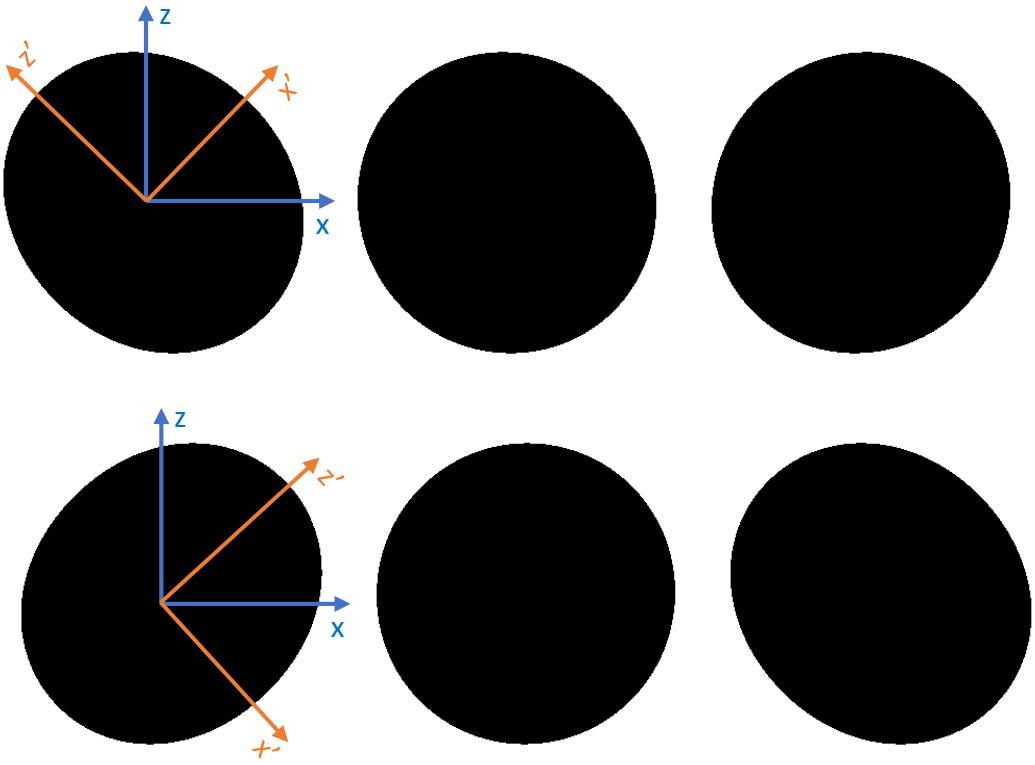

Figure 3.3.16: Oscillation mode l=2, m= ±1 projection in x-z plane (Side-view)

The Side-view high-speed camera is also used to capture the solidification phenomenon of levitated molten alloy and provides an ultra-high frame rate. When the Side-view camera is set to 30 kHz acquisition rate, it would sometimes capture the oscillation motion of the molten droplet a few seconds before solidification during recalescence. Figure 3.3.17 clearly shows a sample oscillation under mixed mode of m=0 and m= ±1 at 30 kHz from the Side-view camera, and the oscillation pattern shows agreement with the current theoretical predictions.

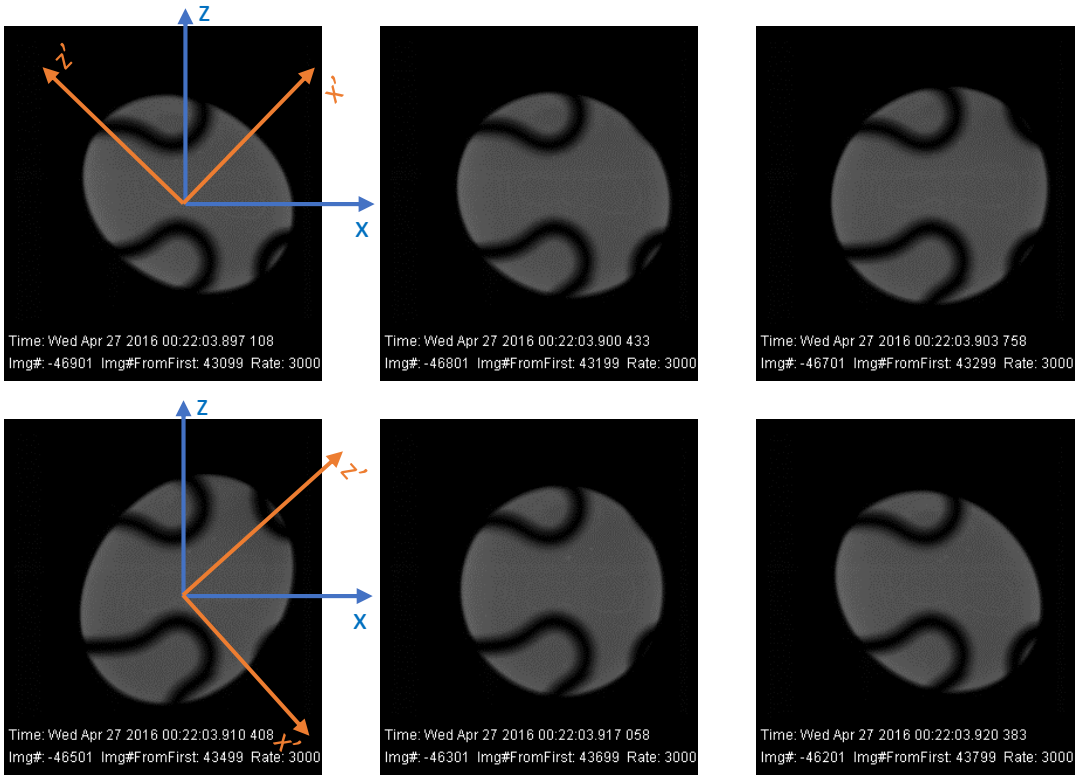

FeCrNi cycle 25

Figure 3.3.17: Side-view 30 kHz video showing mixed oscillation mode m=0, ±1

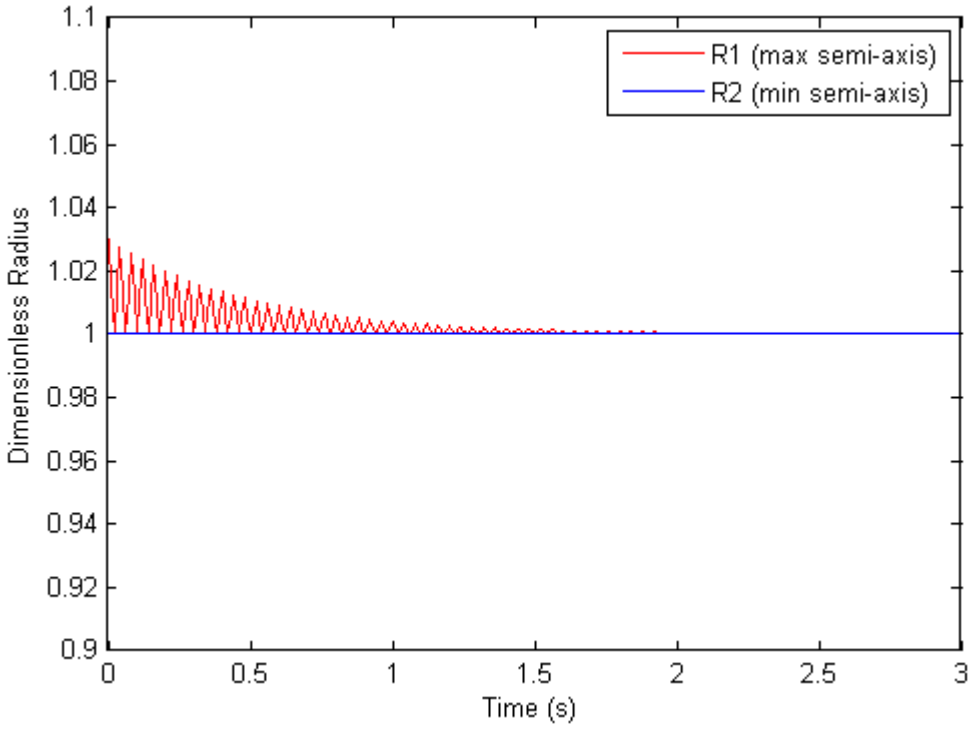

Figure 3.3.18: Damping under oscillation mode l=2, m= ±1 in x-y plane (Top-view)

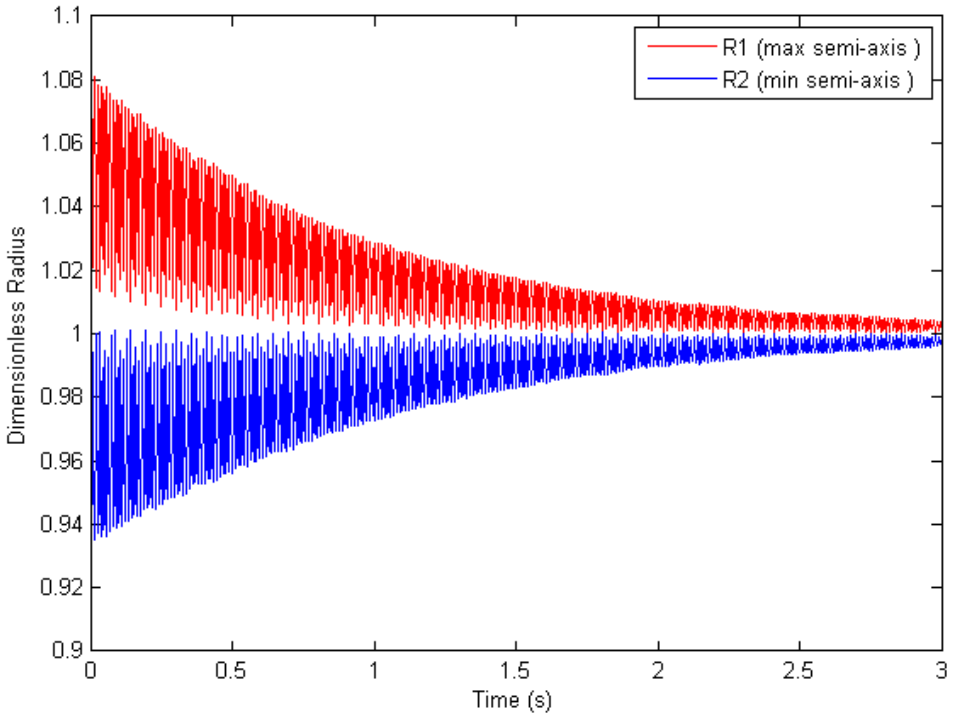

Figure 3.3.19: Damping under oscillation mode l=2, m=±1 in x-z plane (Side-view)

Consider the ratio of length of maximum and minimum semi-axis for sample projections on x-y plane and x-z plane in each oscillation mode l=2, m=0, ±1.

When deformation $\eta_0 < 10\%$, we have the following predictions,

(i). For mode l=2, m=0,

In the x-y plane from Top-view, $\frac{R_1}{R_2} = 1$

In the x-z plane from Side-view, $\frac{R_1}{R_2} < \frac{1+2\eta_0}{1-\eta_0} < 1.35$

(ii). For mode l=2, m=±1,

In the x-y plane from Top-view, $\frac{R_1}{R_2} < 1.04$

In the x-z plane from Side-view, $\frac{R_1}{R_2} < \frac{1+\frac{\sqrt{6}}{2}\eta_0}{1-\frac{\sqrt{6}}{2}\eta_0} < 1.30$

Thus, in either oscillation mode with a reasonable degree of maximum/initial deformation η_0, the radius ratio R_1/R_2 in the x-z plane from the Side-view is expected to be less than 1.35 in theory, and the observations from video analysis of ISS EML experiments are usually in the same range. The radius ratio R_1/R_2 in the x-y plane from the Top-view is expected to be near 1.0 or slightly higher when oscillation mode l=2, m=0 is dominated; for oscillation dominated by mode l=2, m=±1 or with large η_0, the theoretical radius ratio is still expected to be a small value less than 1.04, which also agrees with the experiments in most circumstances. In some cases, the x-y plane radius ratio could be far larger than the 1.05 limit especially after a rapid heater voltage change is applied. Other than the freely damped oscillation, the sample could have an inclination angle when the sample is subjected to an immediate unbalanced force, it would be inclined and the movement would be similar to a rigid body over a short time interval. After a brief recovery period, the influence of the EML positioner coil will stabilize the sample and it will turn back to the orientation vertical to the coil's centerline. Thus, for a thermal cycle consisting of multiple pulse excitations, the sample will be usually more stable for the latter pulse. The Top-view projection has smaller radius ratio for a better viscosity measurement.

Figure 3.3.20 and 3.3.21 shows a typical cycle performing pulse excited oscillation, from Top-view and Side-view separately. In 0.2 and 5.8 seconds, two pulses were applied to excite the oscillation, and Figure 3.3.20(a) and 3.3.21(a) shows the responds of radius change through the ellipse fitting of projections in x-y plane and x-z plane. The changing radius shows agreement with the oscillating pattern analyzed above. In Figure 3.3.20(b) and 3.3.21(b), the radius ratio in each plane is plotted. In the x-y plane, the radius ratio is maximized at 1.04 for the first pulse, and decreases to less than 1.01 and become stable for the second pulse. In the x-z plane, the radius ratio is maximized at around 1.3 and converges to 1.0 as the sample damped out.

During the oscillation process, the sample may be rotating along the z-axis or mis-oriented by an inclination angle. These conditions make it difficult to track a fixed semi-axis of the sample especially when the sample is also undergoing mode m=±1 oscillation. Thus, all the successful analyses using elliptical fitting use the length of the maximum semi-axis R_1 and the length of the minimum semi-axis R_2 for explicit computational convenience.

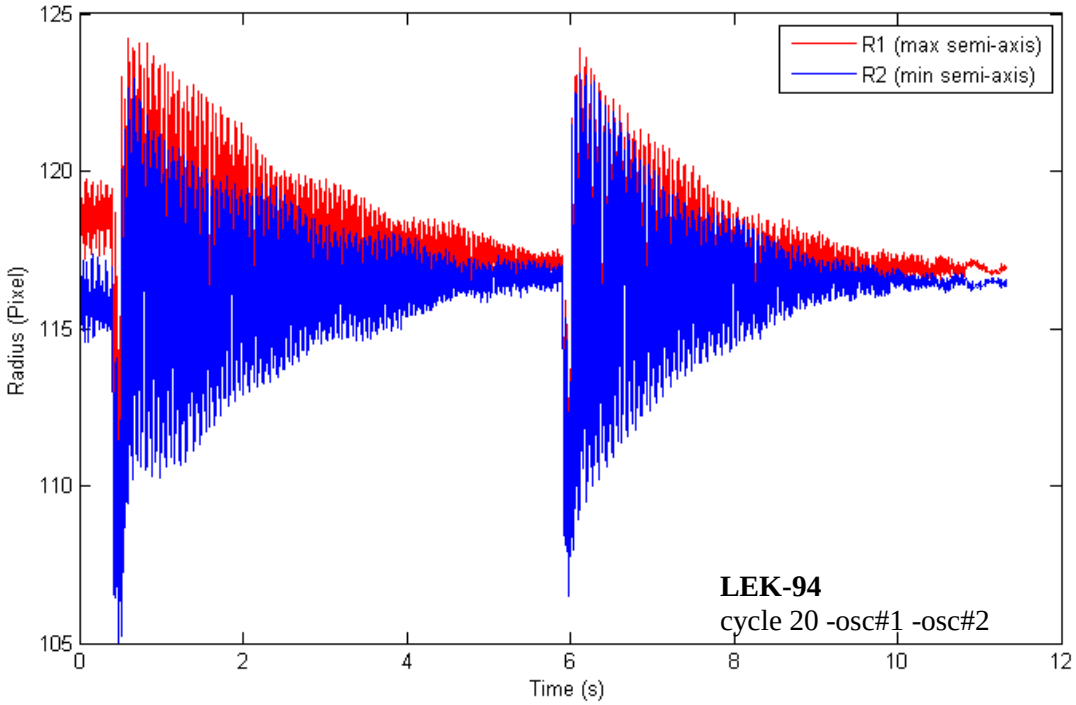

(a) Top-view length of radius vs. time

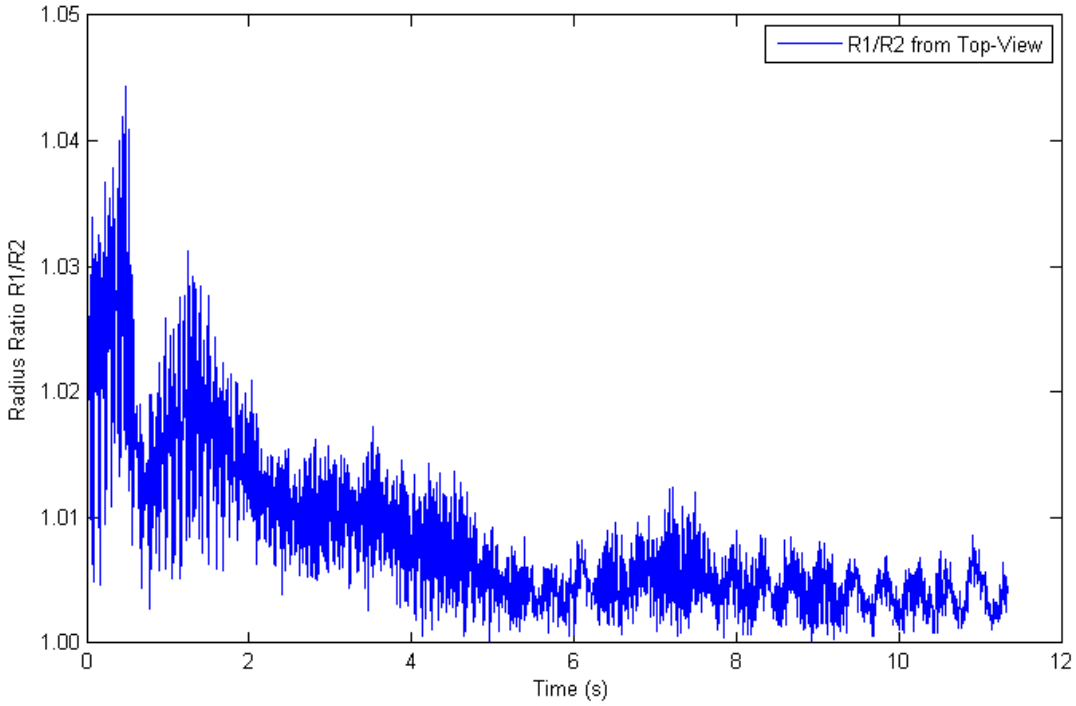

(b) Top-view radius ratio vs. time

Figure 3.3.20: Decaying oscillation analysis from Top-view video

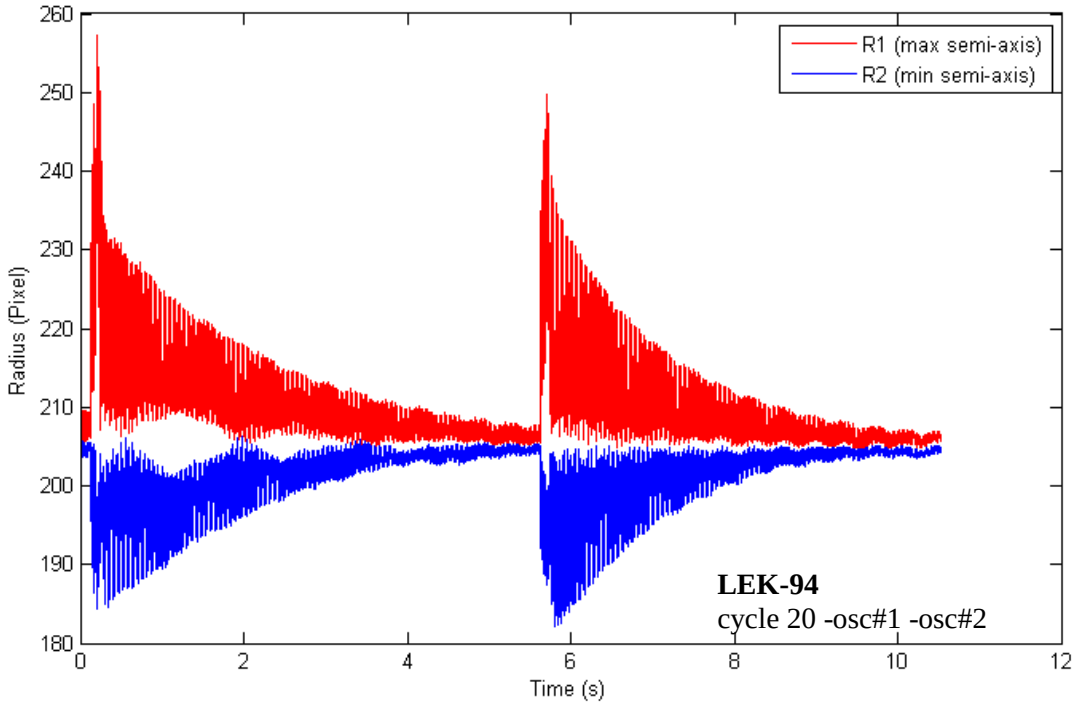

(a) Side-view length of radius vs. time

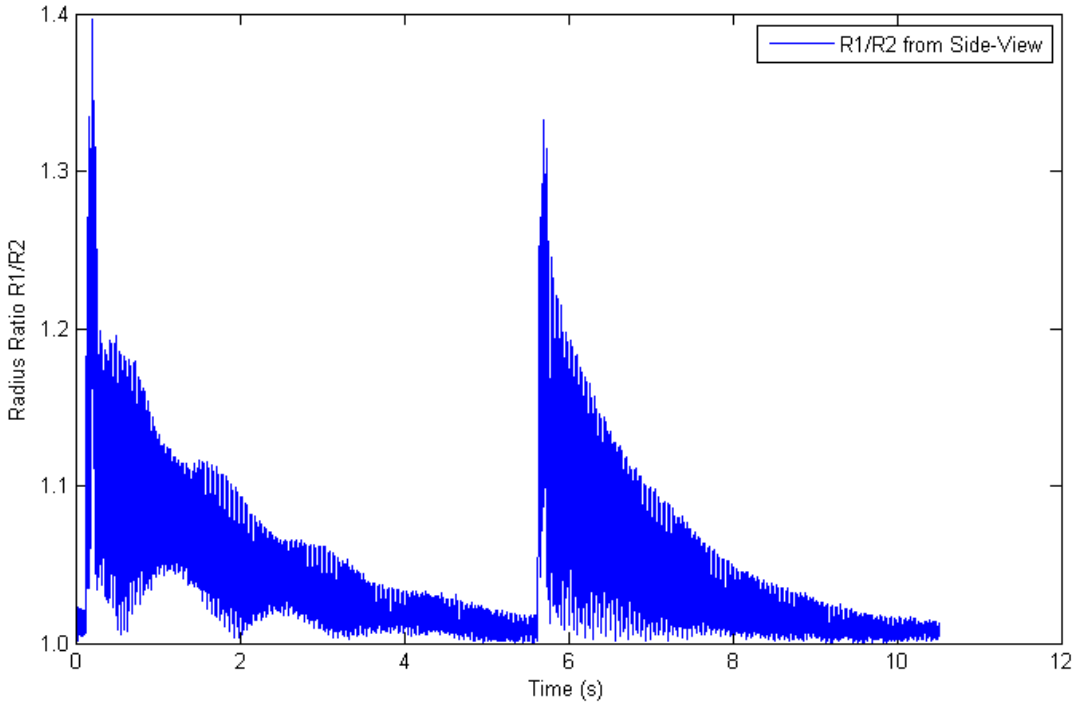

(b) Side-view radius ratio vs. time

Figure 3.3.21: Decaying oscillation analysis from Side-view video

The radius ratio R_1/R_2 in the x-y plane is more sensitive to oscillations mixed with mode $m=\pm1$. Referring to Equation 3.3.36 that describes the radius of a fitted ellipse in the x-y plane subjected to oscillation mode $l=2$, $m=\pm1$, the damping term is nonlinear and the measurement of damping constant will be skewed, and thus an apparent viscosity would be obtained for oscillation mixed with $m=\pm1$ from Top-view. Otherwise, the measurement of damping constant in the x-z plane from Side-view is subjected to oscillation mode $m=\pm1$, would have limited influence due to linearity of the damping term in Equation 3.3.27, or in either the x-y plane or the x-z plane subjected to oscillation mode $m=0$, the damping term is linear in Equation 3.3.15 and Equation 3.3.16, which is directly reflected in the oscillating signal.

During actual oscillation processes excited by a pulse, the result is usually a mixture of mode $l=2$, $m=0$ and mode $l=2$, $m=\pm1$. Based on the radius ratio R_1/R_2 in both the x-y plane and the x-z plane, the proportion of each mode could be estimated and used to predict the skewness of the apparent viscosity measurement.

Based on Equation 3.3.5 describing the droplet deforming shape, various values of $a_{l,m}$ are selected to represent the mixture of different oscillation mode, from proportion of $a_{l=2,m=0}=1$, $a_{l=2,m=\pm1}=0$ to $a_{l=2,m=0}=0$, $a_{l=2,m=\pm1}=1$, and the apparent damping constant τ is measured from simulation with a preset $\tau=1$. As shown in Figure 3.3.22, the damping constant is measured through pure oscillation mode $l=2$, $m=0$ to pure mode $l=2$, $m=\pm1$ at different sample deformation levels. Figure 3.3.22(a) and Figure 3.3.22(b) shows the measurement from the Top-view and the Side-view separately. In line with this approach, for an oscillation only subjected to mode $l=2$ without any other sample movement the simulation shows that the measured τ from the Side-view stays at $\tau=1$ with less than 5% error regardless of the oscillation mode; for measurement from the Top-view, the apparent $\tau\approx1$ from 100% mode $m=0$ to mixture of 50% mode $m=0$ and 50% mode $m=\pm1$, then the apparent τ decreases as the proportion of mode $m=\pm1$ increases to 100%. An error of 30% to 40% is introduced and results in an overestimation of the apparent value of for the measured apparent viscosity.

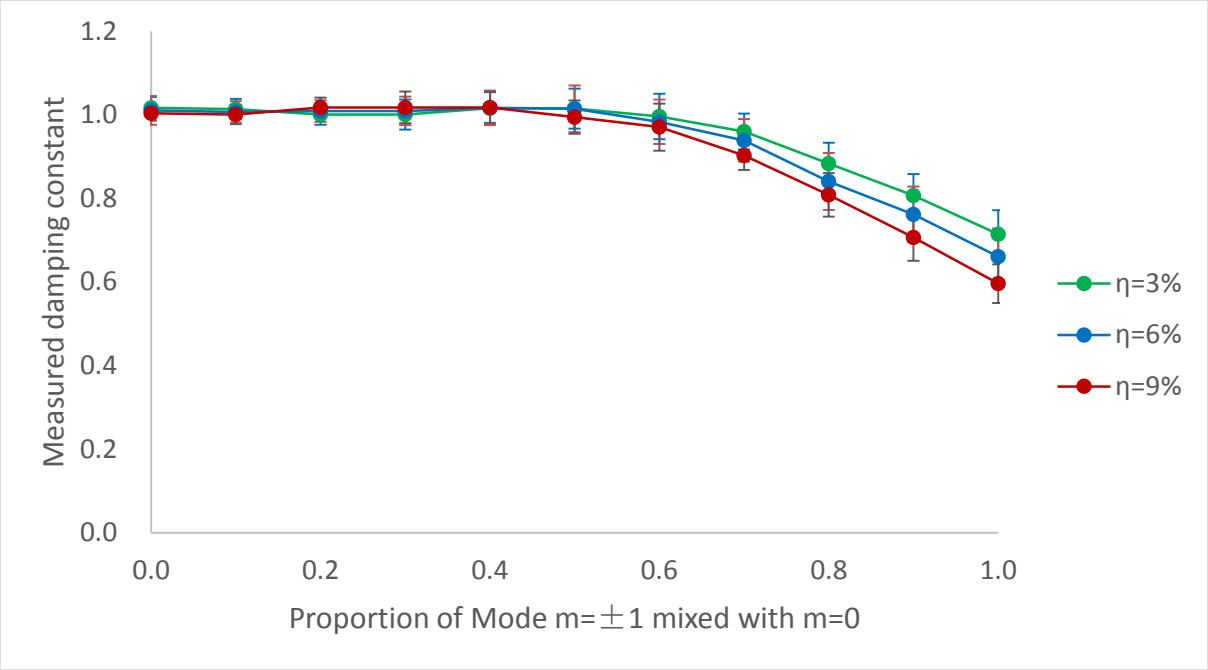

(a) Measurement damping value from Top-view

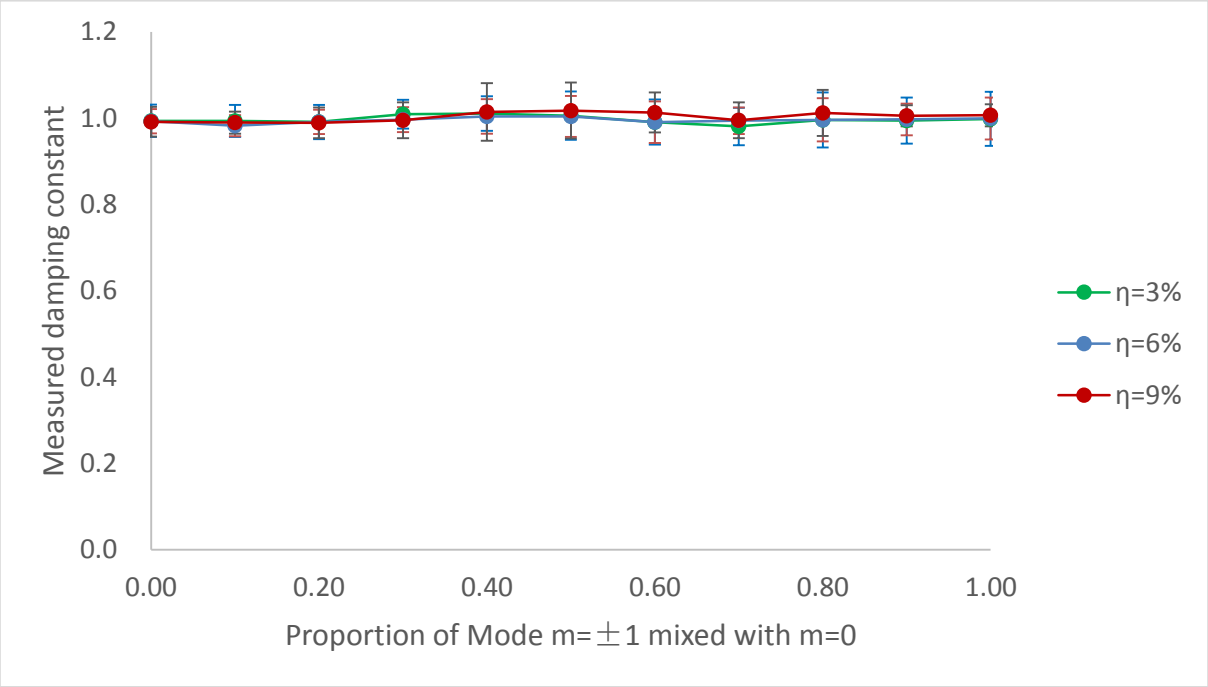

(b) Measurement damping value from Side-view

Figure 3.3.22: Measured damping constant in mixed oscillation mode

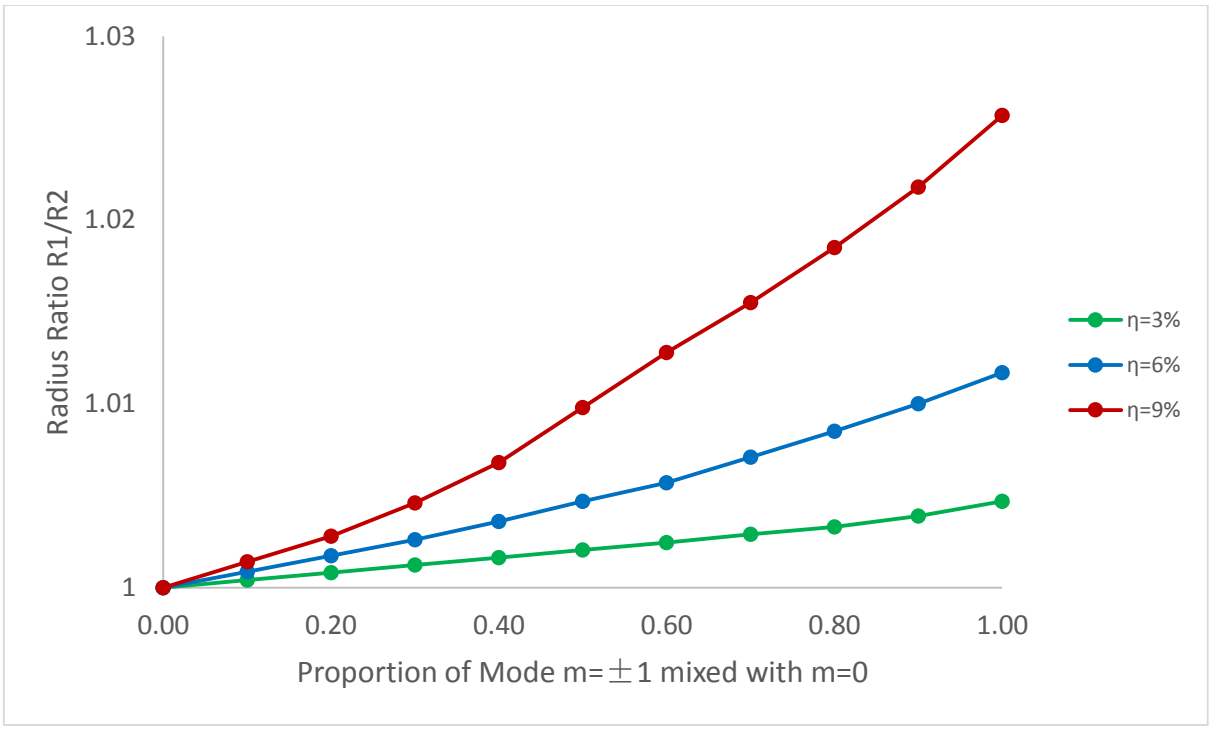

(a) Radius Ratio R_1/R_2 from Top-view

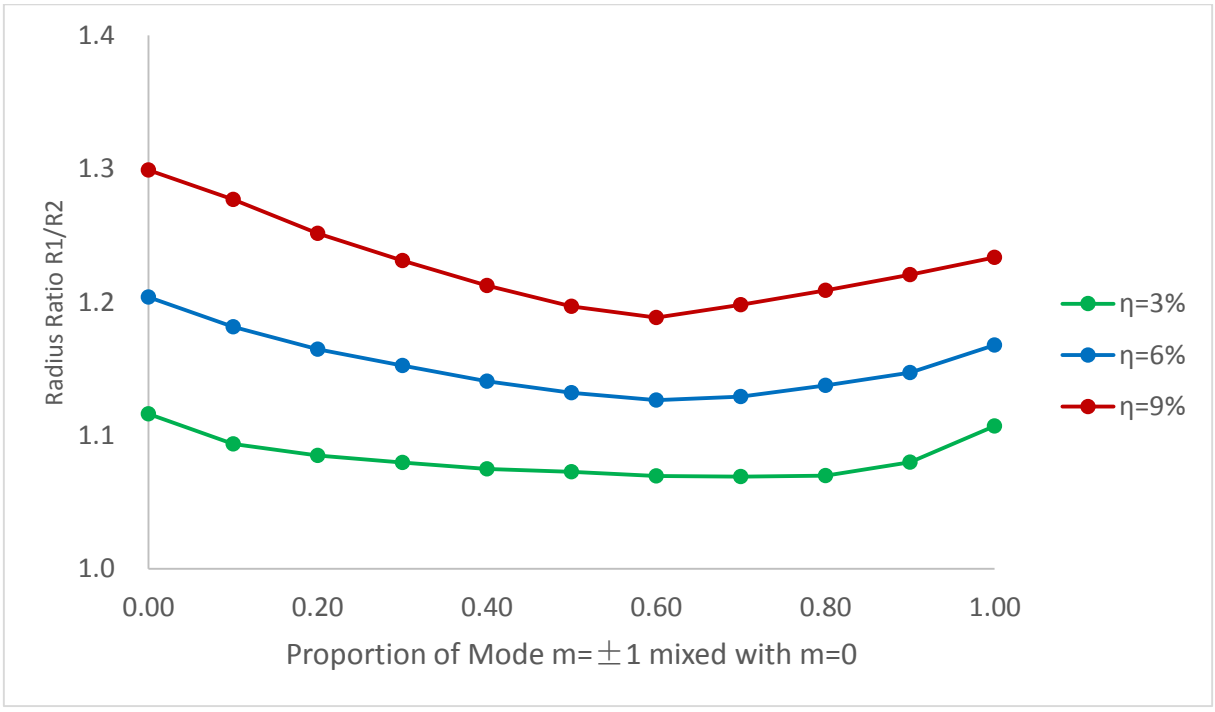

(b) Radius Ratio R_1/R_2 from Side-view

Figure 3.3.23: Radius Ratio R_1/R_2 in mixed oscillation mode

Figure 3.3.23 shows the predicted Radius Ratio R_1/R_2 subjected to the mixture of oscillation modes. From the Top-view, R_1/R_2 is expected to be 1.0 and increased as more proportion of $m=\pm1$ introduced, the behavior is more obvious for larger sample deformation; from the Side-view, R_1/R_2 has significant higher value while the deformation is large, since the fitted maximum radius R_1 represents the dynamic longer z'-axis that has more elongation than R_2.

During a typical pulse excited oscillation, the radius ratio R_1/R_2 from the Side-view is usually around 1.2 to 1.3 immediately following the pulse, and quickly drop below 1.1 to 1.2 then gradually decreased to 1.0 for the damping process, while the Top-view R_1/R_2 usually has a larger than 1.04 value following the pulse, then decreases below 1.03 and is stabilized near 1.0. As shown in Figure 3.3.2 and Figure 3.3.24, pulse size has significant influence on the initial and/or maximum deformation of the sample, either the radius deformation in the x-y plane from the Top-view and radius ratio in the x-z plane from the Side-view increases linearly with the pulse volts, where the Top-view initial and/or maximum radius deformation is in the range of 4.3% to 8.5%, and the Side-view initial and/or maximum radius ratio R_1/R_2 is in the range of 1.19 to 1.34 upon the analysis from ISS EML experiments.

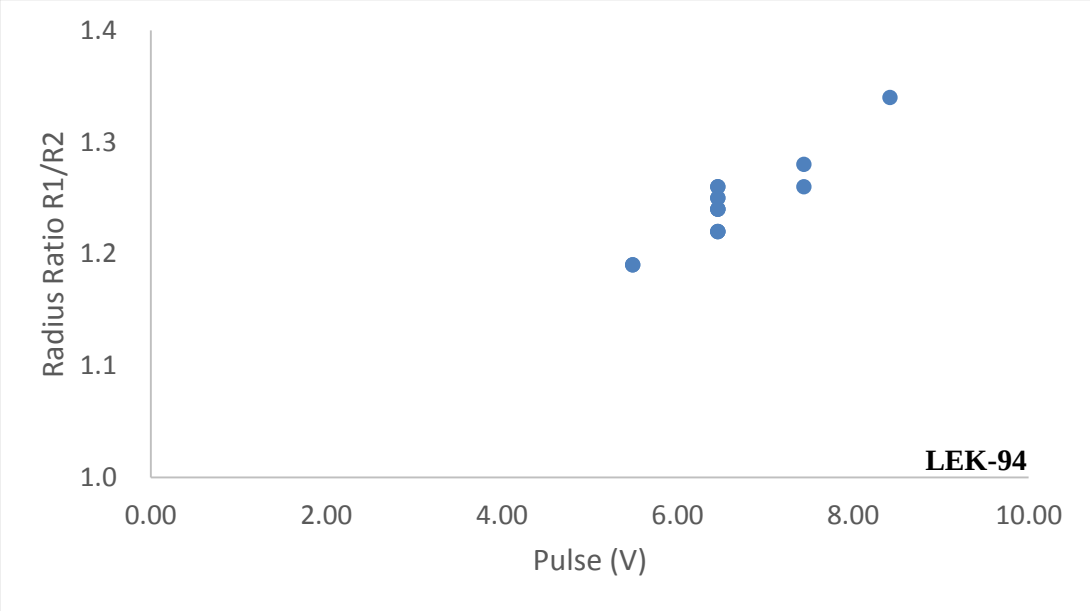

Figure 3.3.24: Maximum Radius Ratio R_1/R_2(Side-view) vs. pulse size

As mentioned above, in practice the Top-view initial and/or maximum radius ratio R_1/R_2 could exceed the theoretical limit of 1.04 following a pulse excitation. The sample was subjected to unbalanced force that makes the deformed droplet inclining or rotating in addition to the self-oscillation. For a deformed sample with a large inclination angle to vertical z-axis, the projection of the sample on the x-y plane that is recorded using the Top-view camera would be approximately of elliptical shape with relatively smaller eccentricity, i.e. the radius ratio R_1/R_2 could be higher than ideal situation. The unbalanced force is assumed to be from a pulse that hit the sample inhomogeneously. During an ISS EML experiment, due to the stabilization function of coil positioner, the sample would move periodically such that it is offset from the centroid of the coil in a steady frequency about 1-2 Hz, and the sample could be in any arbitrary offset position relative to the centroid of the coil at the instant the heater pulse is applied. We define the magnitude of the offset as the percentage of distance from the centroid of the sample to the centroid of the coil relative to the radial size of the sample in an undeformed status.

Figure 3.3.25 shows a typical pattern representing sample movement from the Side-view during nominal operations. The magnitude of the offset is plotted in the x-axis and the z-axis separately, and the specific position of the sample is denoted at the time when the pulse was applied. The offset magnitude in the z-axis, vertical to the centerline of the coil, is the dominating factor for the inhomogeneous pulse force on the sample where the sample would be subjected to more force near the pole of its longer semi-axis. The induced force is much stronger in the horizontal direction than the vertical direction and thus inducing an inclined angle relative to the z-axis is easy. Figure 3.3.26 shows the Top-view radius ratio vs. magnitude of the offset in the z-axis from the Side-view. The measured radius ratio from the Top-view shows an increasing trend with the offset magnitude between sample and the centerline of the coil. While the sample is located at a longer distance from the coil's centerline, there would be more imbalance of the pulse force on a single pole of the longer semi-axis of the ellipsoid shaped droplet sample, and the torque on the sample would become larger thus causing the sample to incline and rotate further. It should be noted that the measured radius ratio is nominal and exaggerated which can be also be influenced by the deflection due to pulse application, thus the ratio might be larger than the predicted limits of 1.04. Figure 3.3.27 shows how the fraction of oscillation mode m=±1 will be increased with larger offset from centerline of coil

at the time of pulse application. When the offset is larger than 4%, mixed-mode oscillations result with a proportion greater than 50% $m = \pm 1$.

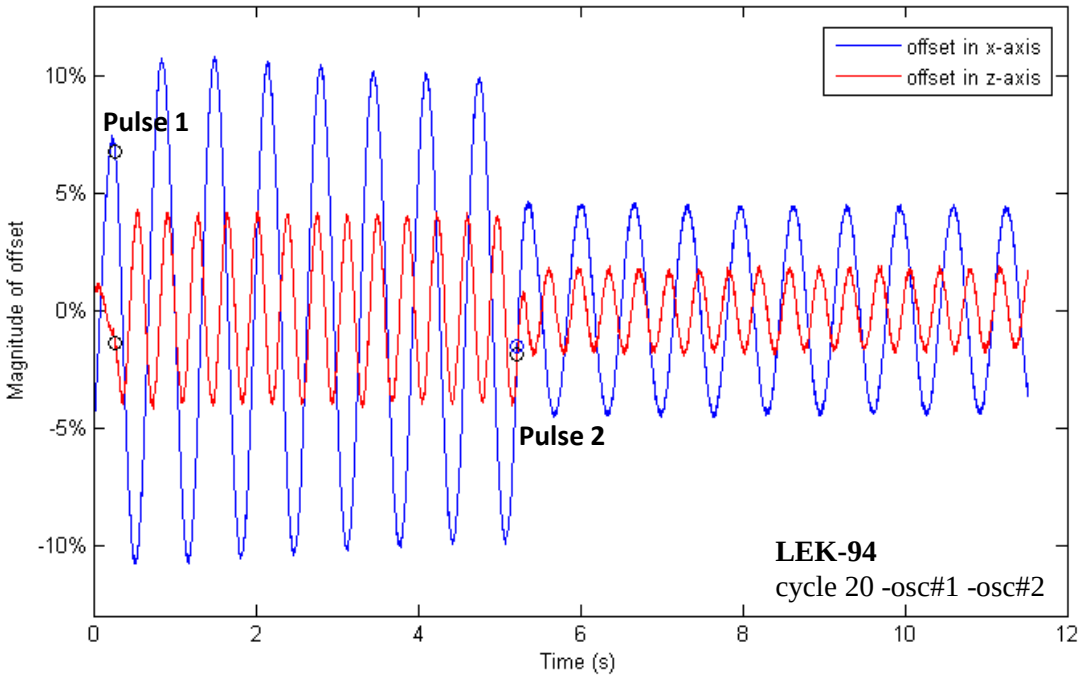

Figure 3.3.25: Magnitude of the offset between sample and coil vs. time

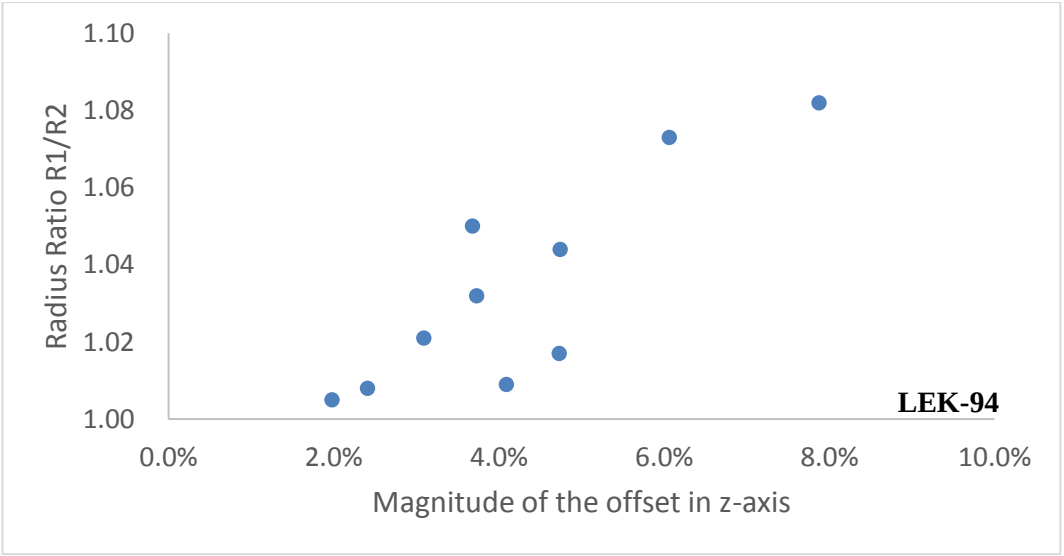

Figure 3.3.26: Radius ratio (Top-view) vs. magnitude of the offset between sample centroid and coil's centerline (Side-view)

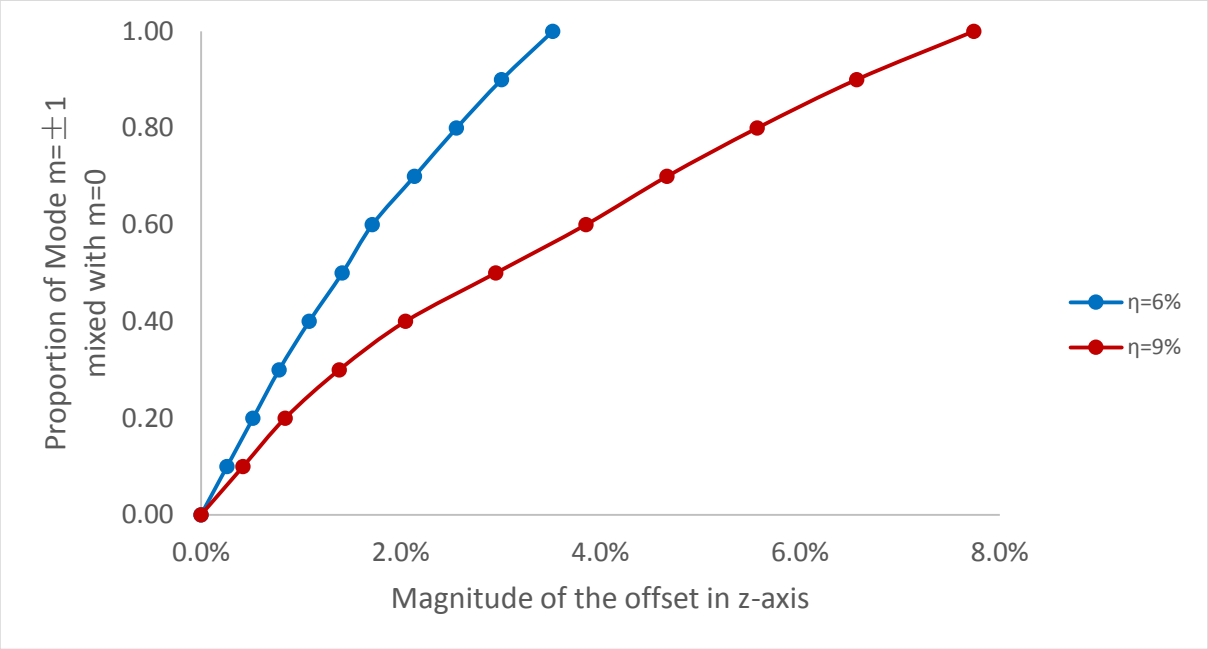

Figure 3.3.27: Mixed oscillation mode vs. magnitude of the offset between sample centroid and coil's centerline (Side-view)

Usually after a short recovering time less than 0.5 to 1.0 seconds, the inclination of the sample caused from the inhomogeneous pulse force would be suppressed by the positioner. However, the sample might still keep rotating along the z-axis at a level of around a few Hertz. The damping constant/viscosity measurement from the Top-view would not influenced by this rotation, since the shape of the sample projection in the x-y plane is unchanged. In contrast, the projection of the sample on the x-z plane from the Side-view would have a distinctive shape change over time that skews the oscillation signal and generates a wavy pattern for the fit of R_1 and R_2 superimposed on the original oscillation curve. This effect introduces difficulty in interpreting the signals used for viscosity measurement from the Side-view videos.

3.3.4 Anharmonic oscillation

The damped oscillation of a levitated viscoelastic droplet could be considered as a spring-mass-damper system[32]. The harmonic oscillation of the ellipsoidal droplet is governed by the classical 2nd ordinary differential vibrating equation as follows,

$$\frac{d^2R}{dt^2} + 2\delta\frac{dR}{dt} + {\omega_0}^2 R = h\cos(\omega_{ext}\, t) \tag{3.3.37}$$

Where R is the deformable radius of the droplet, the damper $\delta = 1/\tau$ is governed by damping constant τ of the liquid which is usually in range of 0.2 to 5.0, and δ has the corresponding value of 5.0 to 0.2, the spring elastic term $\omega_0 = 2\pi f_0$ is governed by the surface tension of the droplet where the oscillation frequency f_0 is usually in the range of 30 to 40 Hz for most sample alloy with 6.5mm in diameter, and the term $h = F/m$ for external force F and mass m. The oscillation is a free vibration when $h = 0$, and for $h \neq 0$ the oscillation is a forced vibration subjected to external periodical forces at angular frequency ω_{ext}. For electromagnetic levitated droplet, the external force is induced from positioner that stabilizes the sample, where ω_{ext}=150 kHz for the SUPOS coil.

For $\delta \ll \omega_0$ and $\omega_0 \ll \omega_{ext}$, the analytical solution to Equation 3.3.37 is,

$$R(t) = A_0 e^{-\frac{t}{\tau}}\cos(\sqrt{{\omega_0}^2 - \delta^2}\cdot t + \varphi_0) + b_0\sin(\omega_{ext}t + \varphi_{ext}) \tag{3.3.38}$$

Where $A_0 = \sqrt{R(t_0)^2 + \frac{\delta R(t_0)^2}{{\omega_0}^2 - \delta^2}} \approx R(t_0)$ is the amplitude subjected to initial deformation, and $b_0 = \frac{h}{\sqrt{({\omega_{ext}}^2 - {\omega_0}^2)^2 + 4\delta^2{\omega_{ext}}^2}} \approx 0$.

Thus, the solution could be approximately expressed in Equation 3.3.39, which has the same form in Equation 2.3.2 that is used to the damping constant fitting and viscosity fitting.

$$R(t) = R(t_0)e^{-\frac{t}{\tau}}\cos(\omega_0 t + \varphi_0) \tag{3.3.39}$$

Consider ellipse area $A = \pi R_1 R_2$, where R_1 and R_2 is the radius of the maximum and minimum semi-axis. Assume $R_2 = cR_1$ for $c \leq 1$, substitute A into Equation 3.3.37, and the equation becomes,

$$\frac{d^2R_1}{dt^2} + 2\delta\frac{dR_1}{dt} + \frac{{\omega_0}^2}{2}R_1 + \frac{1}{R_1}(\frac{dR_1}{dt})^2 = \frac{h}{2\pi cR_1}\cos(\omega_{ext}\, t) \qquad (3.3.40)$$

Here, the lower order term $(\frac{dR_1}{dt})^2$ could be neglected, and Equation 3.3.40 has the similar form as Equation 3.3.37 with the same damping term. Thus, it is feasible to use either the time dependent radius or area of an ellipse as the oscillating signal to fit the damping constant and measure the viscosity.

During an oscillation subjected to mixed-mode or large deformation, there would exist anharmonic nonlinear effects. For a deformed ellipsoidal droplet, it has less surface energy near the poles of the shorter semi-axis where the curvature is smaller, than the longer semi-axis, and such droplet is prone to elongate along the z-axis as a spring that is easier to expand than suppress[32]. For the anharmonic oscillation, it may behave as the spring-mass-damper system consisting of multiple frequencies in the modal analysis. Introducing the high order nonlinear terms to Equation 3.3.37, Equation 3.3.41 represents the nonlinear anharmonic oscillations,

$$\frac{d^2R}{dt^2} + 2\delta\frac{dR}{dt} + {\omega_0}^2R + {\omega_1}^2R^3 + \cdots = h\cos(\omega_{ext}\, t) \qquad (3.3.41)$$

From the ISS EML experiments, secondary or multiple frequencies could sometimes be observed from the FFT analysis of the oscillation signal. Figure 3.3.28 represents an example showing the oscillation subjected to two frequencies. For molten FeCrNi, the primary oscillation frequency is around f_0=37.5 Hz, and occasionally the secondary frequency is around f_1=37.5 Hz. Thus, it is necessary to examine the influence of the anharmonic nonlinear effects on the oscillating signal for damping fitting and viscosity measurement.

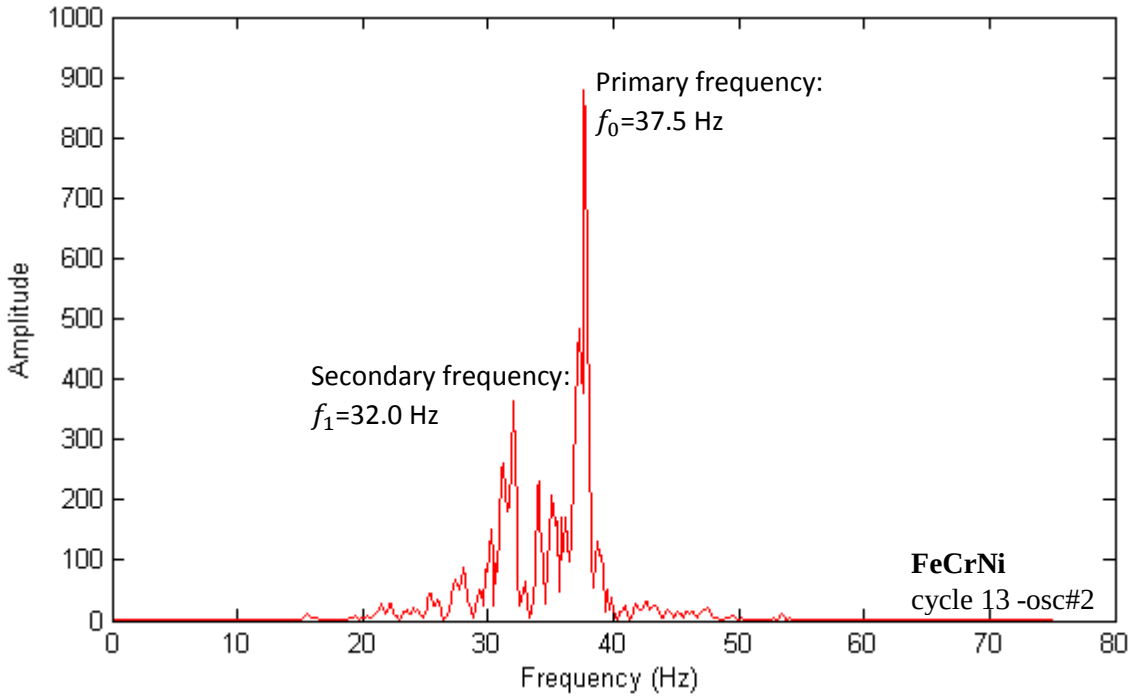

Figure 3.3.28: Oscillation subjected to primary and secondary frequency

The 'ode45' method in Matlab[63] is used to solve Equation 3.3.41 numerically. For the simulated oscillation, the dimensionless radius R=1, damping constant τ=1, the primary frequency f_0=37.5 Hz, and secondary frequency f_1=32.0 Hz. Figure 3.3.29 shows the numerical simulation of the anharmonic oscillation, and compared to harmonic oscillation. Under current experimental parameters, there is no significant variance between the two types of oscillation, and the nonlinear effect of this type could considered to be negligible for the application of damping constant fitting and viscosity measurement.

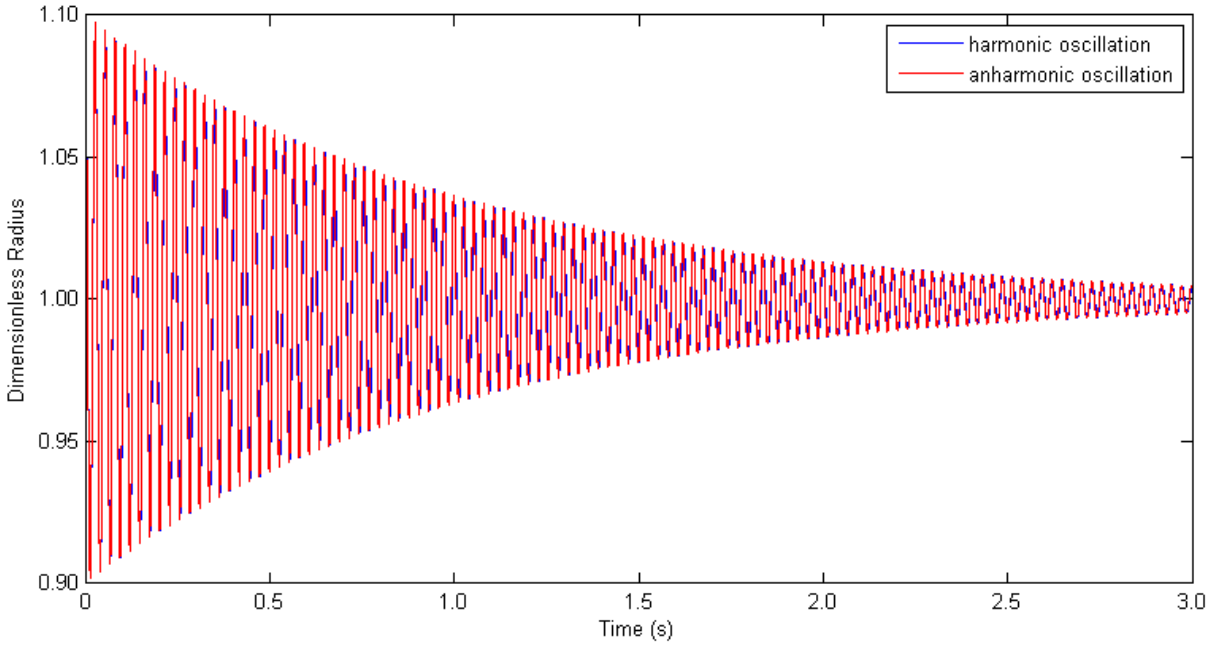

Figure 3.3.29: Simulation of harmonic and anharmonic oscillation

4 Magnetohydrodynamic Simulation

4.1 Magnetohydrodynamic Modeling

Magnetohydrodynamics (MHD) of the electromagnetically levitated (EML) molten alloy droplet is the interacting phenomenon consisting of the electromagnetic field through the conductive liquid induced from the EML coil and the convection flow inside the droplet that is stirred from the induced electromagnetic force[47]. The predications of the convection velocity and flow pattern inside the levitated droplet is essential for thermophysical properties measurement and investigations of alloy solidification which depends on the velocity and status of the internal convection flow during the experiment.

The flow inside the levitated droplet could be assumed as compressible and viscous, which is governed by the dimensionless variable Navier-Stokes equations,

$$\nabla \cdot \vec{u} = 0$$
$$\frac{\partial \vec{u}}{\partial t} + \vec{u} \cdot \nabla \vec{u} = -\nabla p + \frac{1}{Re} \nabla^2 \vec{u} + \vec{F} \tag{4.1.1}$$

where $\vec{u}$ is the velocity vector, p is the pressure, μ and ρ is the viscosity and density of the liquid, and $\vec{F}$ is the momentum source. For the EML coil, the momentum source term $\vec{F}$ is the electromagnetic force per unit volume. The Navier-Stokes equations above could be solved using appropriate numerical methods.

The boundary conditions are assumed to be a slip wall, where there is no shear stress on the free surface, and no flux across the surface,

$$\tau \cdot \hat{\imath}_t|_{r=1} = 0$$
$$u_r|_{r=1} = 0 \tag{4.1.2}$$

Where τ is the shear stress, and $\vec{\imath}_t$ is the tangent unit vector.

The convection flow could be characterized by the Reynolds number (Re) indicating the ratio of inertial effects to viscous effects. Based on the Reynolds number, the laminar or turbulent

status of the internal convection flow could be evaluated and support further analysis of the thermophysical properties or solidification data. The Reynolds number is defined as,

$$Re = \frac{\rho u d}{\mu} \tag{4.1.3}$$

where μ is the viscosity, ρ is the density, u is the convection velocity, and d is the diameter of the sample droplet.

4.1.1 Simulation methodology

The electromagnetic forces in the molten alloy droplet induced from the EML coil could be solved through use of Maxwell's equations.

In the EML simulation, the induced eddy current in the levitated sample is responsive to the change in the coil current, and the system could be treated as magnetoquasistatic and a reduced form of Maxwell's equations could be defined in Equation 4.1.4, where the time derivative of the electric displacement field term in the third equation of Maxwell's could be neglected[36].

$$\begin{aligned} \nabla \times \vec{B} &= 0 \\ \nabla \times \vec{E} &= -\frac{\partial \vec{B}}{\partial t} \\ \nabla \times \vec{H} &= \vec{J} \end{aligned} \tag{4.1.4}$$

where $\vec{J}$ is the induced current, $\vec{H}$ is the magnetic field, $\vec{B}$ is the magnetic flux density, and $\vec{E}$ is the electric field.

The electromagnetic force which is also known as Lorentz force is written as,

$$\vec{F} = \vec{J} \times \vec{B} \tag{4.1.5}$$

The reduced Maxwell's equations could be solved numerically and the Lorentz forces per unit volume could be calculated using the method of mutual inductances[5]. A subroutine was

developed[41] to calculate the electromagnetic force, and the calculated force field could be implemented into the Navier-Stokes equations as the momentum source term.

The MHD model is developed using the commercial package ANSYS Fluent[65] to simulate the internal fluid flow and predict the convection velocity in the electromagnetic levitated droplet under different thermophysical conditions and power settings of coil. The model was validated with the experimental data of an EML $Co_{16}Cu_{84}$ droplet by the flow velocity on the surface of the sample[46].

The geometry of two-dimensional axisymmetric semi-sphere with radius of 3.25 mm is used, and the mesh consists of optimized number of 550 cells and 591 nodes as shown in Figure 4.1.1. The electromagnetic force is calculated using the subroutine and implemented into the mesh as shown in Figure 4.1.2. The estimated skin depth is about 2.5mm[66] where the electromagnetic force dominates around 77% of the sample's depth from its surface.

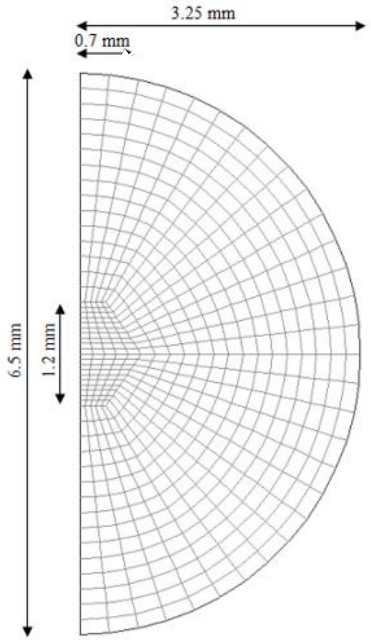

Figure 4.1.1: Two-dimensional axisymmetric model for levitated droplet

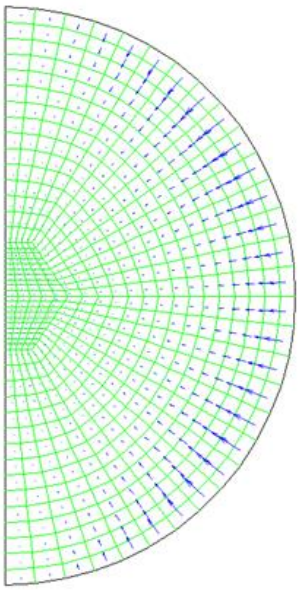

Figure 4.1.2: Implemented electromagnetic momentum force

For a typical pattern of the convection flow inside the liquid droplet in a heater dominated electromagnetic field, there are two circulation loop near the stagnation lines at the equator of the sphere, where the induced electromagnetic force has the maximum magnitude. Figure 4.1.3 shows the distribution of the electromagnetic force and vector of convection velocity on the left and right of the sphere separately.

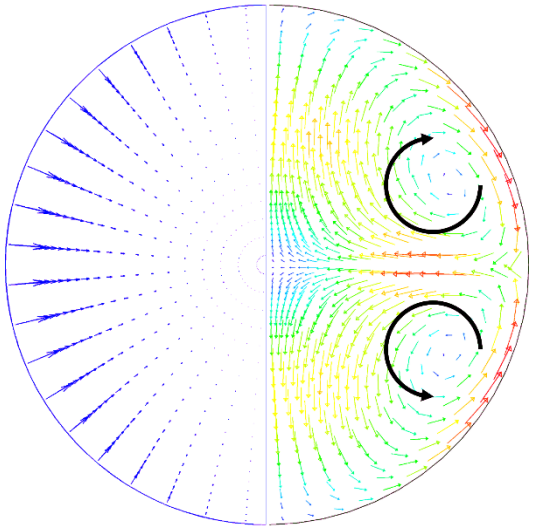

Figure 4.1.3: Electromagnetic force and convection flow inside the droplet

4.1.2 Laminar and turbulent model

With the introduced electromagnetic force as the momentum source term, both of laminar and turbulent model is used in the simulation to predict the convection velocity.

For the convection flow of Newtonian fluid with relative low velocity and Reynolds number, the laminar model is appropriate and accurate. The ANSYS fluent solves the Navier-Stokes equations using the finite volume method. For a levitated molten droplet, when the Reynolds number as defined in Equation 4.1.3 is larger than 500 to 600, the internal flow could be considered as developed to be turbulence upon observation of experiments[45].

For turbulence simulation, many models were developed including the approaches of Reynolds-averaged Navier–Stokes equations (RANS), direct numerical simulation (DNS), and Large eddy simulation (LES). The DNS method directly computes the turbulent eddies at all the scales which requires very fine mesh grid and tremendous computing resources. The LES method filters out the small scale eddies and computes the large scale eddies only, and uses a universal model to characterize the smaller scale eddies that are filtered out, based on the assumption that the turbulence has certain similarity in the scales that are small enough. Actually, the turbulence at intermediate scale may have some similarities when it has a relative high Reynolds number, and this type of scale could be defined as the inertial subrange. In practice, it is feasible to filter the eddies at the inertial subrange to reduce computing intensity, however the inertial subrange is usually still quite small in the near wall region where also requires very fine mesh grid and large computing intensity. Instead of computing the turbulent eddies directly, the RANS method solves the Navier–Stokes equations for multiple times and averages the results statistically. The RANS method actually convert the non-steady state turbulence problem to a steady-state problem with an extra Reynolds stress term, and only seeks the time-averaged results for a rough estimation, while it has loose requirement for the mesh grid and moderate computing intensity.

The RANS method which requires less computing resources is used in the turbulence model for a preliminary estimation of the turbulence status of the convection flow inside the droplet. The renormalization group (RNG) k-ε turbulence model is one of the RANS methods which

is effective for the simulation of levitated molten alloy droplets[43]. The vector of turbulence velocity u consists of the time-averaged velocity $\bar{u}$ and the fluctuation $\bar{u}'$,

$$\begin{aligned} u &= \bar{u} + u' \\ \bar{u} &= \lim_{T\to\infty} \frac{1}{T} \int_0^T u \, dt \end{aligned} \tag{4.1.6}$$

And Equation 4.1.1 becomes the time-averaged Navier–Stokes equations,

$$\frac{\partial \bar{u}}{\partial t} + \bar{u} \cdot \nabla \bar{u} = -\nabla \bar{p} + \frac{\mu}{\rho} \nabla^2 \bar{u} + F - \nabla \cdot (\overline{u'u'}) \tag{4.1.7}$$

where $\bar{p}$ is the averaged pressure, and $\overline{u'u'}$ is the Reynolds stress term describing the additional stresses generated from turbulent fluctuations.

Additional two equations are included in the k-ε turbulence model, including the turbulent kinetic energy equation and energy dissipation equation representing the dissipation rate of the turbulent kinetic energy,

$$\begin{aligned} \frac{\partial k}{\partial t} + \bar{u} \cdot \nabla k &= \left(u + \frac{u_t}{\sigma_k} \right) \nabla^2 k + P_k - \varepsilon \\ \frac{\partial \varepsilon}{\partial t} + \bar{u} \cdot \nabla \varepsilon &= \left(\frac{\mu}{\rho} + \frac{u_t}{\sigma_\varepsilon} \right) \nabla^2 \varepsilon + C_{1\varepsilon} \frac{\varepsilon}{k} P_k - C_{2\varepsilon} \frac{\varepsilon^2}{k} \end{aligned} \tag{4.1.8}$$

With additional boundary conditions,

$$\begin{aligned} \left. \frac{\partial k}{\partial r} \right|_{r=1} &= 0 \\ \left. \frac{\partial \varepsilon}{\partial r} \right|_{r=1} &= 0 \end{aligned} \tag{4.1.9}$$

Where the turbulent kinetic energy is defined as $k = \frac{1}{2}\overline{u_i{}'u_i{}'}$, $P_k = \tau_{ij}\left(\partial \bar{u}_i/\partial x_j\right)$ is the kinetic energy production, $u_t = C_\mu(k^2/\varepsilon)$ is the kinematic eddy viscosity, and $\varepsilon = \frac{\mu}{\rho}\frac{\partial \overline{u_i{}'}}{\partial x_j}\frac{\partial \overline{u_i{}'}}{\partial x_j}$ is the dissipation rate.

In Equation 4.1.8, the RNG k-ε model uses the following coefficients,

$$\begin{aligned} C_{1\varepsilon} &= 1.42 \\ C_{2\varepsilon} &= 1.68 \\ C_\mu &= 0.085 \\ \sigma_k &= 0.72 \\ \sigma_\varepsilon &= 0.72 \end{aligned} \qquad (4.1.10)$$

4.2 Simulation Results

4.2.1 Steady-state model

For the levitated droplet subjected to a constant heater power or positioner only, the internal convection flow will achieve and maintain at a steady-state status in a short time after the electromagnetic force is imposed on the sample. With a fixed positioner power, the convection velocity inside the droplet is predicted for various heater power levels and different thermophysical propriety values that depends on the temperature. Based on the magnitude of the corresponding Reynolds number, the flow conditions are evaluated to be either laminar, turbulence, or laminar-turbulence transition status.

Figure 4.2.1 shows the simulation results of the convection velocity of FeCrNi molten droplet with T_m=1715K, the positioner is maintained at 5.21V, the heater voltage is set from 0.0V to 6.5V, under the temperature from T_m-200 to T_m+200. There is a heat limit that the sample could never achieve certain lower temperature while the heater is constant on. Figure 4.2.2 shows the corresponding Reynolds number, the laminar flow starts to transit to turbulence from Re = 450, and considered as fully developed turbulence above Re = 600.

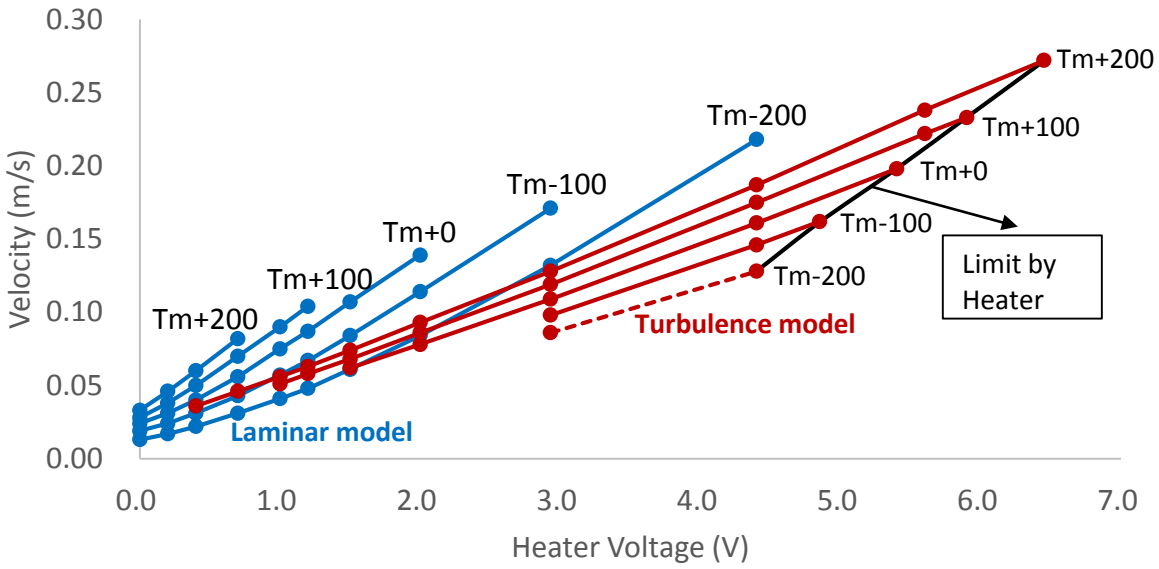

Figure 4.2.1: Convection velocity vs. Heater voltage for FeCrNi

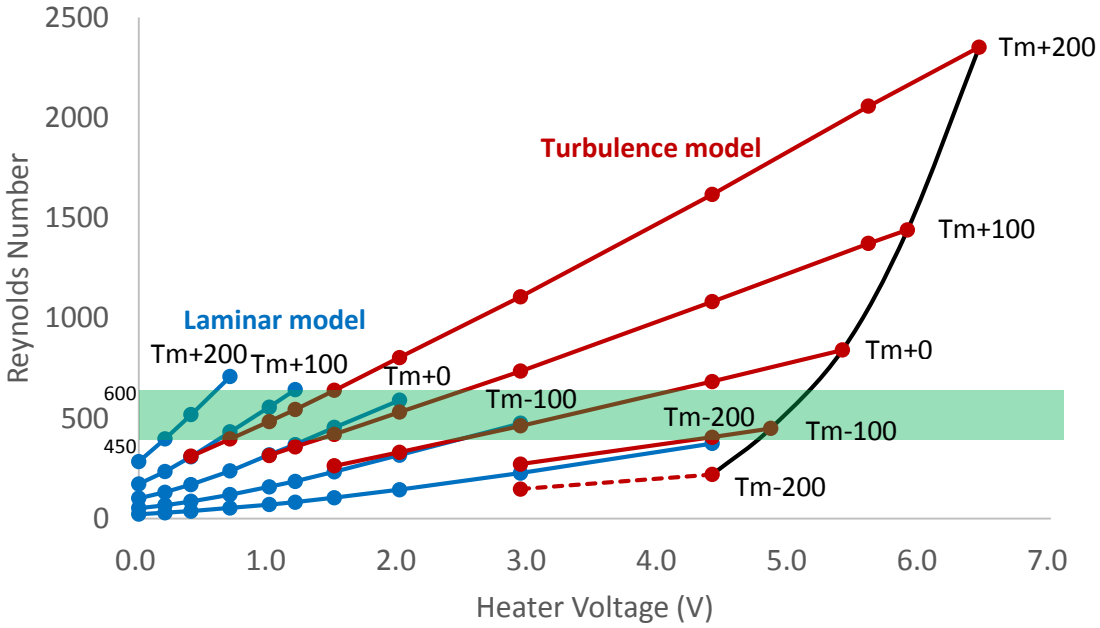

Figure 4.2.2: Reynolds Number vs. Heater voltage for FeCrNi

Both the laminar and turbulent models are utilized in the simulation. While the results from the k-ε turbulence model is time-averaged with less accuracy, it is feasible to use the results from the laminar model to calculate the Reynolds number for convective flow in the laminar or transitional states. In Figure 4.2.3, the critical heater voltage versus different droplet temperature is plotted where the flow is considered as turbulent above the critical curve and it is laminar or transitional below the curve. This provides a guideline for recommending heater power settings when quiescent/laminar flow is desired such as during viscosity measurement.

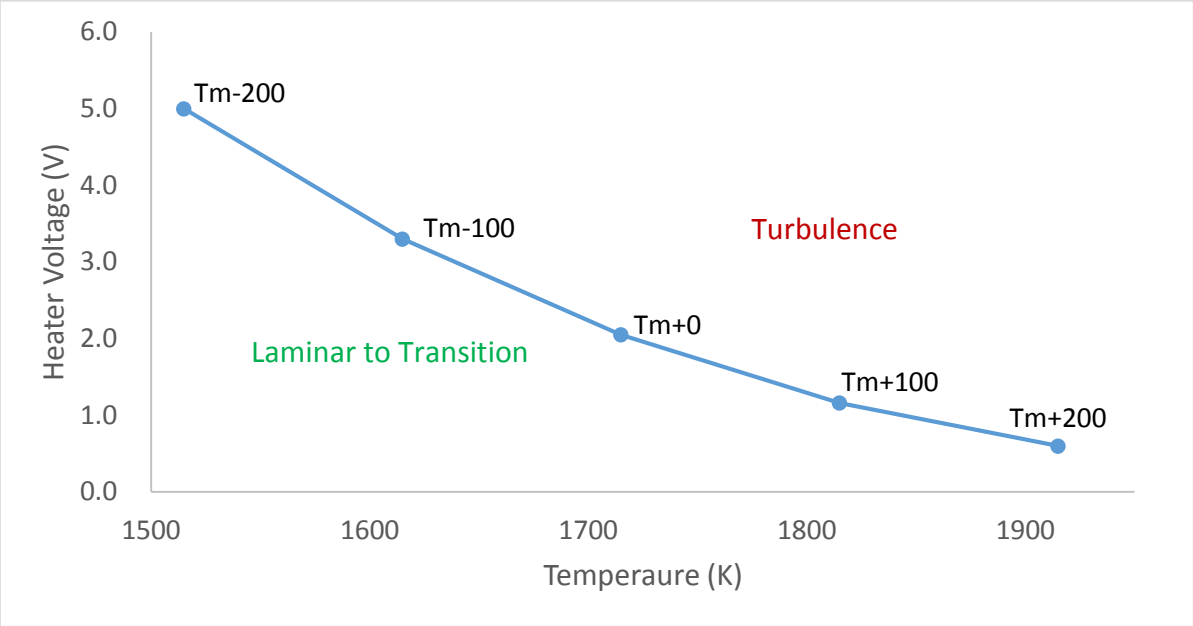

Figure 4.2.3: Critical Heater voltage vs. Temperature for FeCrNi

4.2.2 Transient model

During the ISS EML thermal cycles designed for thermophysical property measurement, the heater is usually off or maintained at a small voltage to allow the sample to freely cool down with minimal flow. For viscosity measurement, the molten droplet is excited by a heater pulse for a duration of 0.1 seconds with pulse size varying from 5V to 9V. It is necessary to examine the internal flow status after the heater pulse is applied to determine if residual turbulence induced by the heater pulse is sufficient to influence the viscosity measurement significantly.

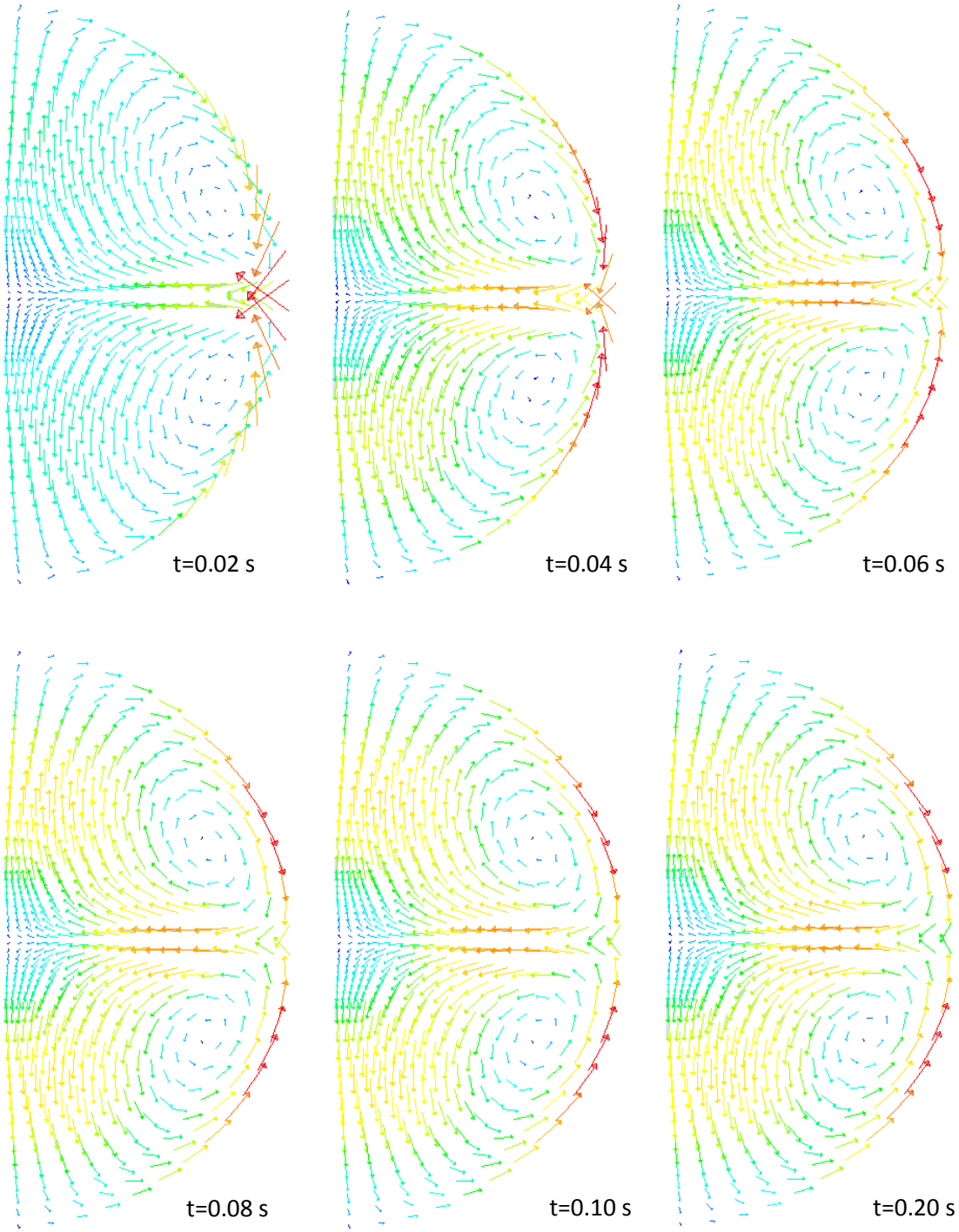

Figure 4.2.4: Developing convection flow inside levitated droplet

In the transient model, we assume the application of a heater voltage pulse which is not subsequently released. Figure 4.2.4 shows the convective flow as a function of time after pulse application. The flow initiates on the droplet surface and transitions to the inside of the droplet as the two circulation loops near the surface develop and move towards the interior; during this process, the stagnation line at the equator gradually becomes clear. The convective velocity is maximized near the droplet surface and below refers to this extreme value as the toroidal loop causes internal recirculation.

For a molten FeCrNi droplet at T_m, Figure 4.2.5 shows the increasing recirculation velocity versus the elapsed time from the heater on with voltage of 5.0V to 8.0V. The recirculation flow achieves equilibrium after 0.2 seconds, and the transient velocity achieves 80% to 90% of the steady-state velocity in 0.1 seconds depending on the power level. After 0.1 seconds, the corresponding Reynolds number is increased to well above the critical value of 600, indicating that the heater pulse could introduce fully turbulent conditions in only 0.1 seconds. As shown in Figure 4.2.6, for FeCrNi at T_m, the Reynolds number at 0.1 seconds elapsed time is plotted versus different applied pulse voltage magnitudes.

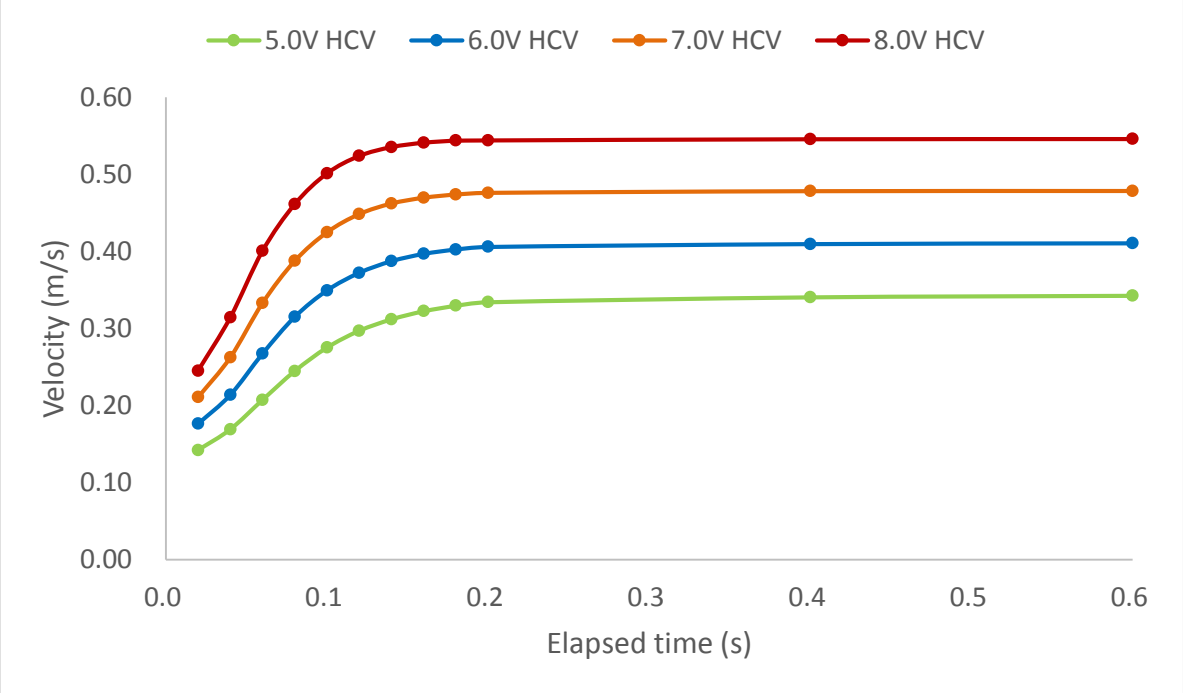

Figure 4.2.5: Convection velocity vs. time for FeCrNi at T_m

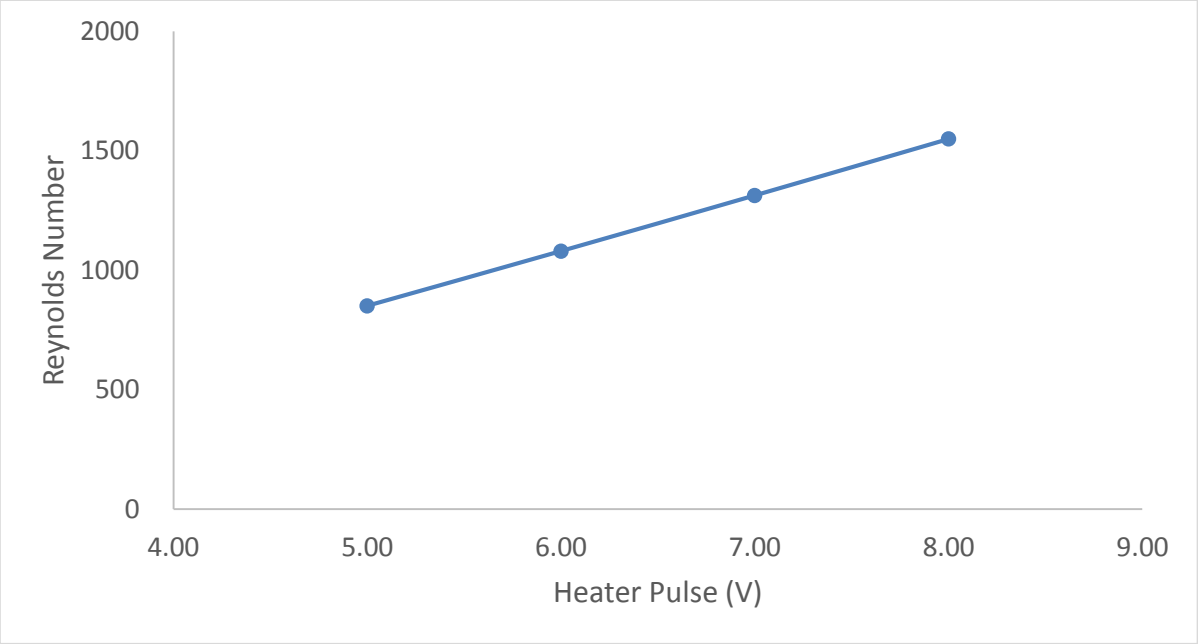

Figure 4.2.6: Reynolds number vs. 0.1s Pulse for FeCrNi at T_m

For sample droplet subjected to a 0.1 seconds heater pulse, the droplet will be squeezed in the equator by the electromagnetic momentum forces induced from the coil. As discussed previously, the squeezed sample will shrink in the x-y plane, and elongate along the z-axis accordingly. When the pulse is released after 0.1 seconds, the sample will achieve the maximum/initial deformation of the equator radius, which is usually from 4% and up to 9%, and then it will start the damped oscillation process.

Additionally, consider the influence of the shape of droplet on the convection velocity by comparing flow in the spherical state versus the deformed shape. Compared to the spherical droplet, the maximum recirculation velocity in the squeezed droplet will be reduced due to the decrease in electromagnetic momentum forces. As shown in Figure 4.2.7, the simulation predicts that the recirculation velocity along the surface of a squeezed droplet with a 6% radial deformation is approximately 8% less than in the undeformed droplet.

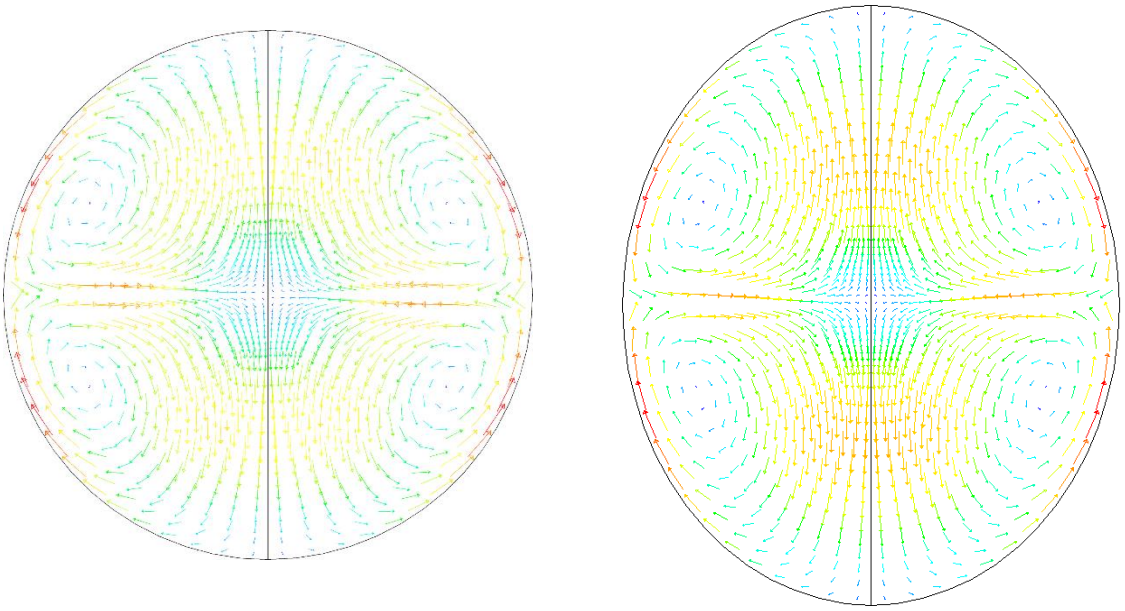

(a) Undeformed droplet **(b) Squeezed droplet**

Figure 4.2.7: Convection flow inside undeformed and squeezed droplet

4.3 Turbulence Decaying Time

For viscosity measurement using oscillating droplet technique in space, the sample is excited by a heater pulse to start the damped oscillation. Application of the 0.1 seconds heater pulse inevitably induces turbulent flow. The magnitude of the turbulence can be characterized using the Reynolds number calculated from the convection velocity and thermophysical properties that depend on temperature.

Turbulent stirring inside the molten droplet can significantly influence the overall damping behavior of the droplet oscillation, such that the droplet would damp out much quicker than under quiescent conditions due to the added momentum transfer from the turbulent eddies, and the measured apparent viscosity from the damped oscillating signal would be overestimated while the turbulence exists. Thus, for a valid viscosity measurement, the induced turbulence from the pulse should be allowed to decay, and it is necessary to evaluate the time required to achieve appropriate laminar flow conditions.

For each oscillation of a molten FeCrNi droplet with 0.1 seconds pulse excitation, the Reynolds number is calculated based on its maximum recirculation velocity from the transient MHD simulation at different pulse application temperatures, and the duration of the Phase-1 region is evaluated from the oscillating signals as described in Section 3.2. Figure 4.3.1 plots the Phase-1 duration time for FeCrNi oscillations subjected to 0.1 seconds of 6.01V and 7.01V pulse at temperature from 1680K to 1840K, and compared with the estimated turbulence decay timescale reported in the references.

Hyers [41] defined time scale for viscous relaxation where the viscous drag reduces the internal flow inside the droplet to zero, which is also shown as the dash curve in the figure,

$$t = \frac{\rho l^2}{\mu} \tag{4.3.1}$$

Where ρ and μ is the temperature dependant density and viscosity of the liquid, l is the characteristic length of the flow, for levitated droplet $l \approx \frac{R}{3}$ for the droplet radius R.

Vassilicos [68-70] developed a theory of turbulent decay through evaluation of flow energy reduction based on the von Karman-Howarth turbulence equation[67], derived from the Navier-Stokes Equation, and developed a correlation which is also shown as a dotted curve in Figures 4.3.1 – 4.3.4.

$$u'^2 = {u_0}'^2(1 + ct)^n \tag{4.3.2}$$

Where u' is the fluctuating velocity as defined in Equation 4.1.6, and could be estimated as square root of two times of the turbulence kinetic energy $u' = \sqrt{2k}$, $c > 0$ is a constant coefficient, n lies between 1.2 and 1.43, and t is the elapsed time.

Here, ${u_0}'$ is the fluctuating velocity at the time pulse is applied and released, and the internal convection reaches a maximum, u' has the value corresponding to when the Reynolds number leaves the turbulence region just below the value of 500-600, and the elapsed time t required for turbulence decay could be estimated accordingly under different pulse and temperature settings,.

Figure 4.3.2 and Figure 4.3.3 shows the Phase-1 duration time versus temperature for LEK-94 and MC-2 subjected to different pulse sizes. The duration of Phase-1 region has increased value with both pulse voltage and temperature, and shows agreement with the theoretical estimation.

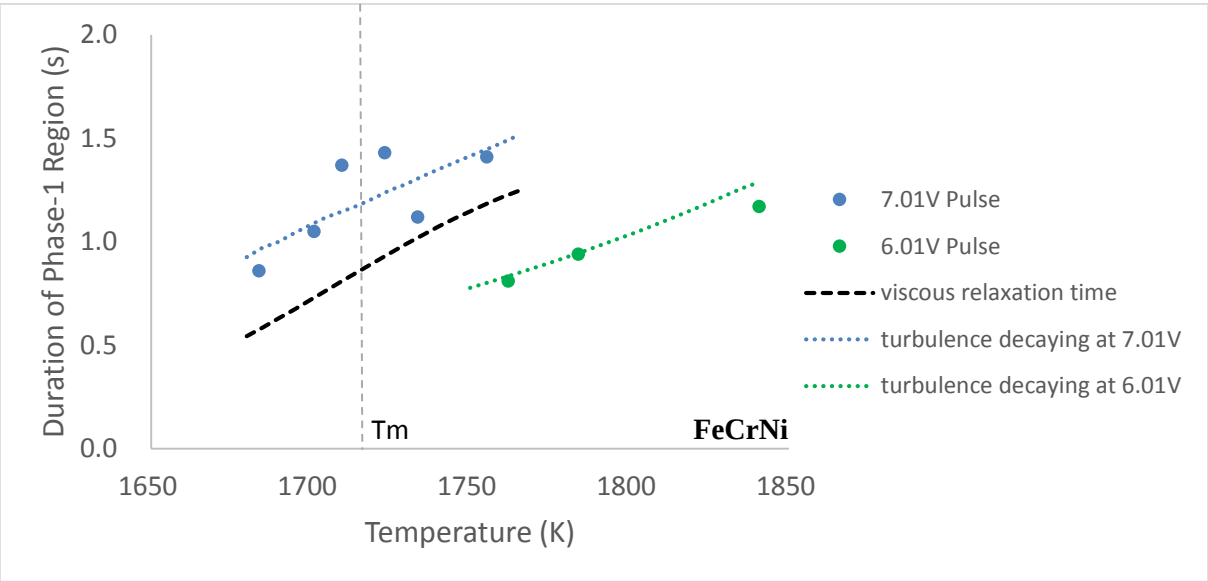

Figure 4.3.1: Phase-1 duration time vs. Temperature/Pulse voltage for FeCrNi

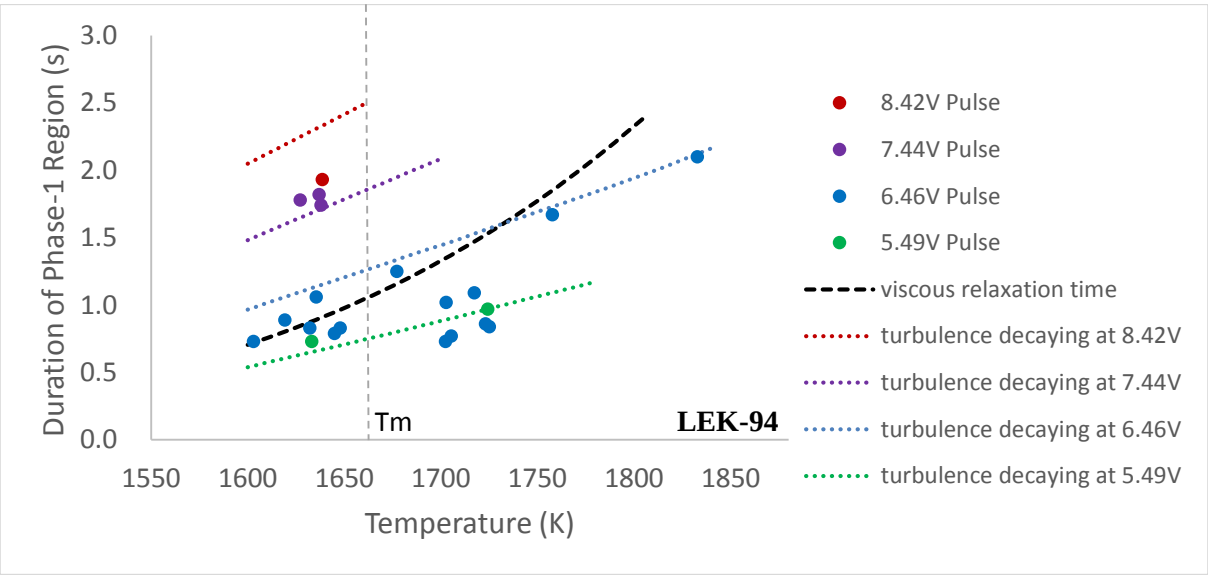

Figure 4.3.2: Phase-1 duration time vs. Temperature/Pulse voltage for LEK-94

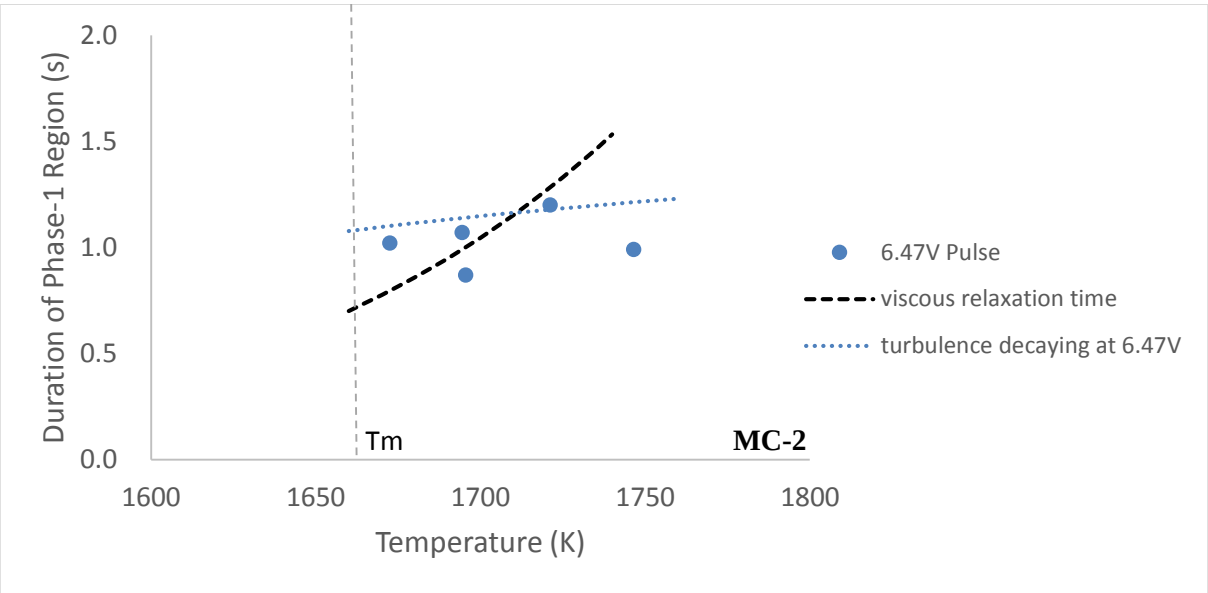

Figure 4.3.3: Phase-1 duration time vs. Temperature/Pulse voltage for MC-2

Figure 4.3.4 shows the Phase-1 duration time versus different values of Reynolds number for all of the different compositions (note that previous figures were plots as a function of temperature). By selecting the Reynolds number, which includes the effects of both temperature dependent thermophysical properties and pulse size that would introduce different level of turbulence, a summary of normalized behavior is apparent. The duration of the Phase-1 region increases approximately linearly with the magnitude of Reynolds number, indicating that the turbulent decay time is the dominating factor in the Phase-1 region of the pulse excited oscillation. Finally, an empirical formula could be given to estimate the turbulence decay time as a function of Reynolds number.

Turbulence decaying time:

$$t = 1.413 \cdot \log_{10}(Re) - 3.317 \qquad (4.3.3)$$

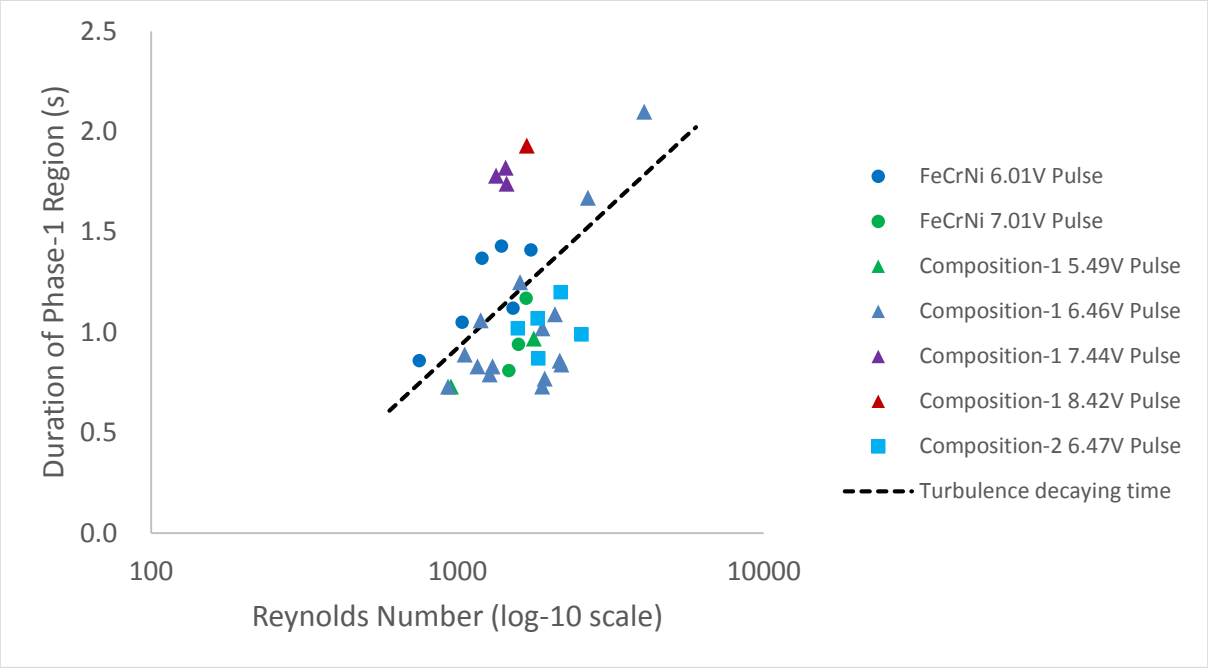

Figure 4.3.4: Phase-1 duration time vs. Reynolds Number

5 Results and Discussions

5.1 Viscosity Analysis

Section 3.1-3.2 discussed the damping-transition for the pulse-excited sample droplet. This transition which could be divided into two distinct behavioural regimes - Phase-1 and Phase-2. The damping of the sample in Phase-1 region is assumed to be significantly influenced by the internal turbulent convection induced by the excitation pulse and to a lesser extent by the large shape-deformation which occurs during the initial stages of surface oscillation and sample motion. When the droplet is subjected to a 5V to 9V heater pulse, the sample showed an apparent viscosity 2-4 times larger than the reference values. As shown in Figure 5.1.2, the k-ε turbulence model shows a ratio of 2-9 of the turbulence effective eddy viscosity to the molecular viscosity with an average value around 5.5. This is on the same order of magnitude as for the present work. Prior to the decay of turbulence, the oscillation will have a faster damping rate. Thus, an overestimated apparent viscosity would be introduced in the Phase-1 region while the turbulence exists, and the time length of Phase-1 region could be considered as the same time scale for turbulence decay which as discussed in Section 4.3. In the Phase-2 region, the droplet becomes quiescent with an associated reduction in deformation with conditions favoring accurate measurement of viscosity.

Figure 5.1.1 and 5.1.3 shows the measured viscosity in the Phase-1 and the Phase-1 regions, respectively. In the Phase-1 region, the measured viscosity is overestimated which could be up to two times larger than the viscosity measured in the Phase-2 region. After the transition from Phase-1 to Phase-2 oscillation, the damping rate steadily increases as well as the viscosity. In a limited number of cases the heater was turned on to a desired constant voltage setting to control the cooling rate of the sample during oscillations. As discussed in Section 4.2.1, during a thermal hold with constant heater voltage, the internal convection of the sample droplet will achieve and maintain a steady-state value. Specifically, for FeCrNi cycle 12, the 2.01V constant heater would induce fully turbulent conditions during all oscillations based on predictions using MHD simulations. While the sample transitions from Phase-1, with pulse-induced turbulence at elevated levels, it continues to maintain a relatively smaller-scale turbulence level induced from the heater constantly throughout the Phase-2 region. The viscosity measured in Phase-2

also shows an overestimated value and thus should be considered as an invalid measurement result.

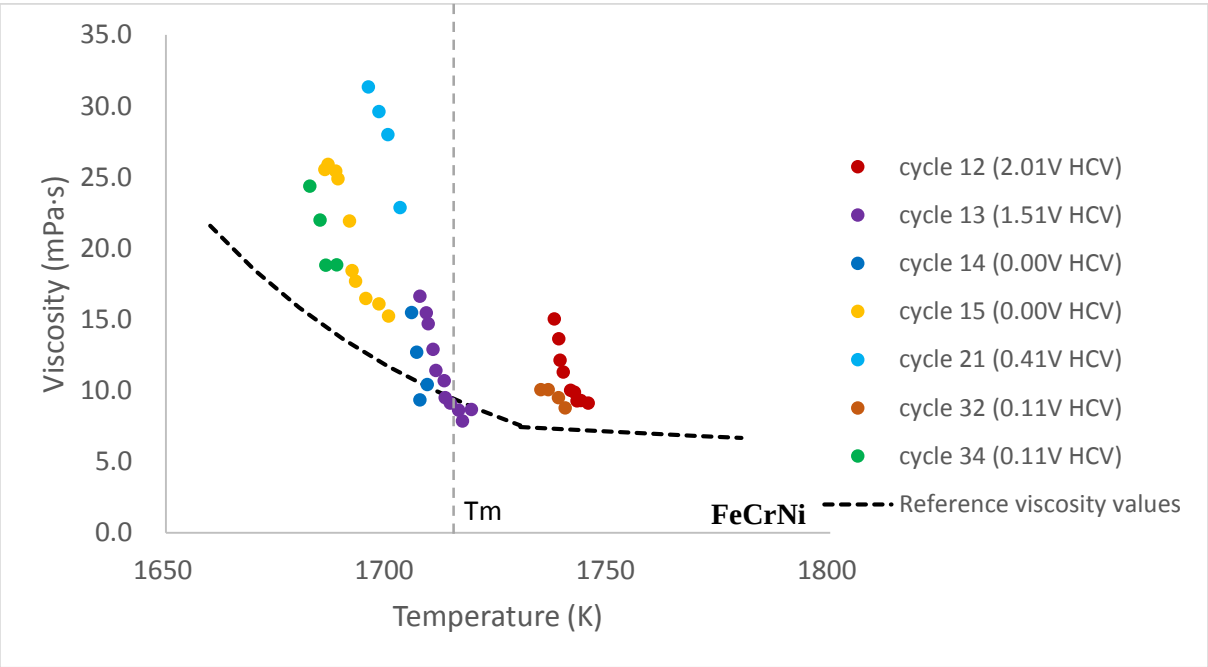

Figure 5.1.1: Measured viscosity in Phase-1 region for FeCrNi

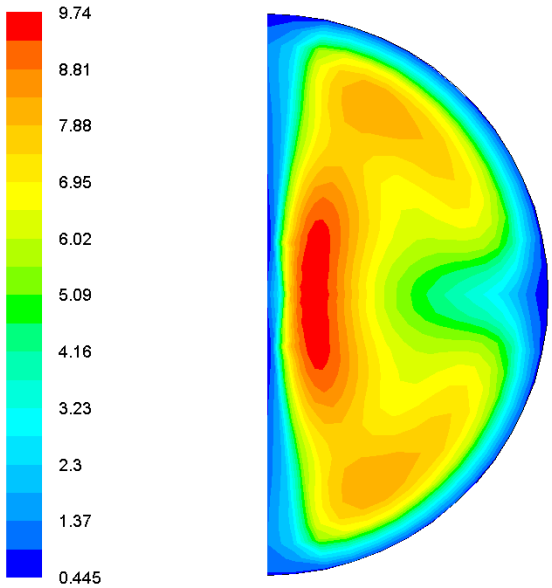

Figure 5.1.2: Turbulent viscosity ratio in MHD simulation for FeCrNi

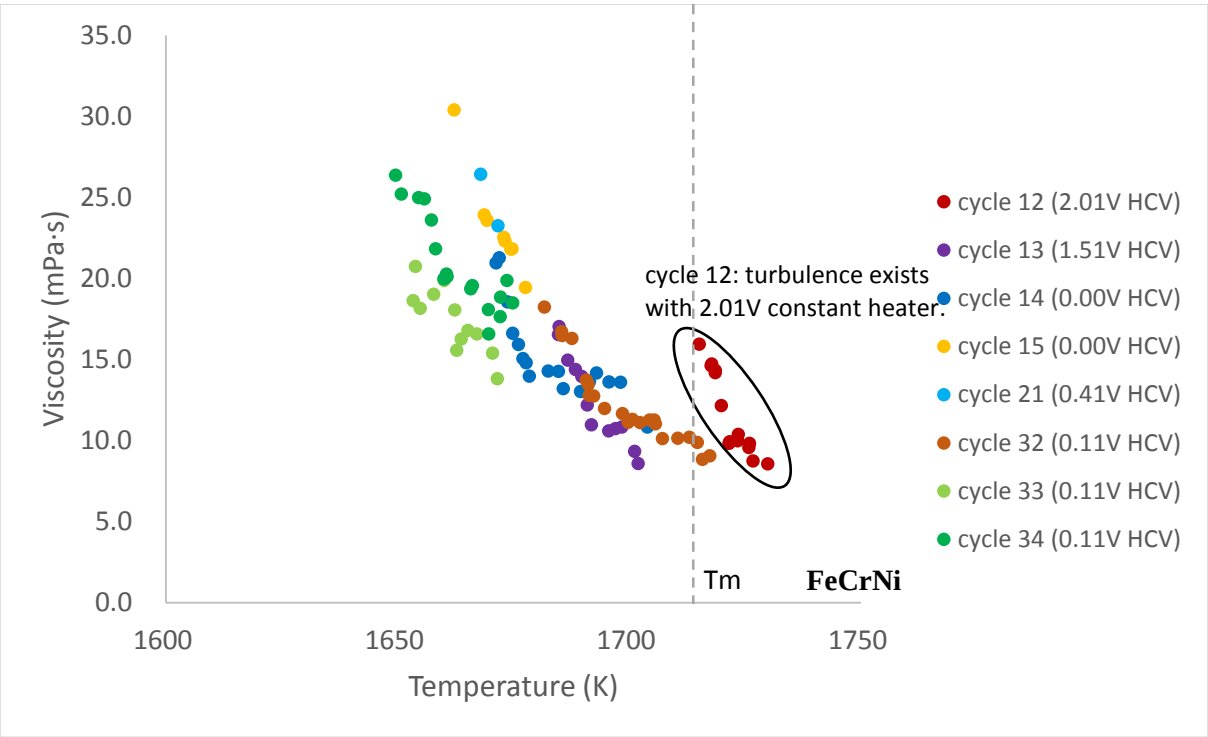

Figure 5.1.3: Measured viscosity in Phase-2 region for FeCrNi

As discussed in Section 3.3.2, larger deformation of the sample induces internal turbulent convection which would dampen oscillation faster and skew the viscosity measurement. Referring to the estimation from Etay [17], for a droplet with motion-varying Relevant Reynolds number R_e^* as determined by thermophysical properties and the magnitude of the deformation, certain critical limits are suggested for a moderate R_e^* value. The viscosity is significantly overestimated above the limits due to errors introduced by the changing shape and these conditions render analysis result to be viewed as an invalid measurement. The measured viscosity has acceptable error below the limits.

The Relevant Reynolds number R_e^* defined in Equation 3.3.2 is inversely proportional to the temperature dependent viscosity. The R_e^* value increases significantly with rising temperature as the viscosity decreases exponentially as temperature is increased. Thus, the R_e^* is sensitive to viscosity when the deformation is small, and the region below the critical limits is dominated by the viscosity term only. In contrast, the region above the critical limits is dominated by both viscosity and deformation terms if the deformation is high.

Figure 5.1.4 shows the viscosity and deformation dominated regions for FeCrNi at different temperatures, and compares the transition limit with experimental data including the magnitude of the deformation and the temperature at the end of the Phase-1 region. The suggested deformation limit is between 5% to 1% for temperatures from T_m-40 to T_m+10, and between 3% and 1% for temperatures from T_m+10 to T_m+100. The deformation at the end of Phase-1 region is basically observed to be in-line with or below the critical deformation limits, indicating that the sample would already have damped to a state characterized by relatively small deformations before the turbulence fully decayed.

Figure 5.1.5 and Figure 5.1.6 shows the deformation limits for priority LEK-94 and MC-2 respectively, which represents similar observations. For LEK-94, the deformation limit is between 4.5% to 3% for temperature from T_m-75 to T_m+10, and between 3% to 1.5% for temperature from T_m+10 to T_m+100. For MC-2, the deformation limit is between 7.5% to 3% for temperature from T_m-60 to T_m+40, and between 3% to 2.0% for temperature from T_m+40 to T_m+100.

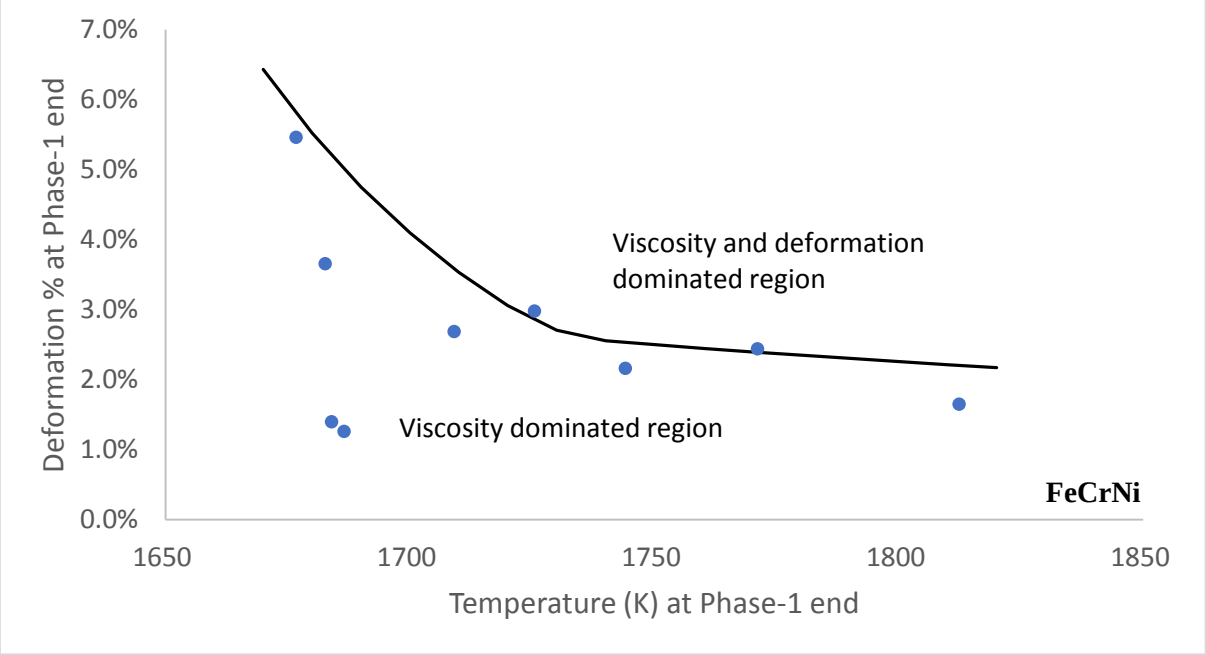

Figure 5.1.4: Viscosity and deformation dominated region for FeCrNi sample droplet

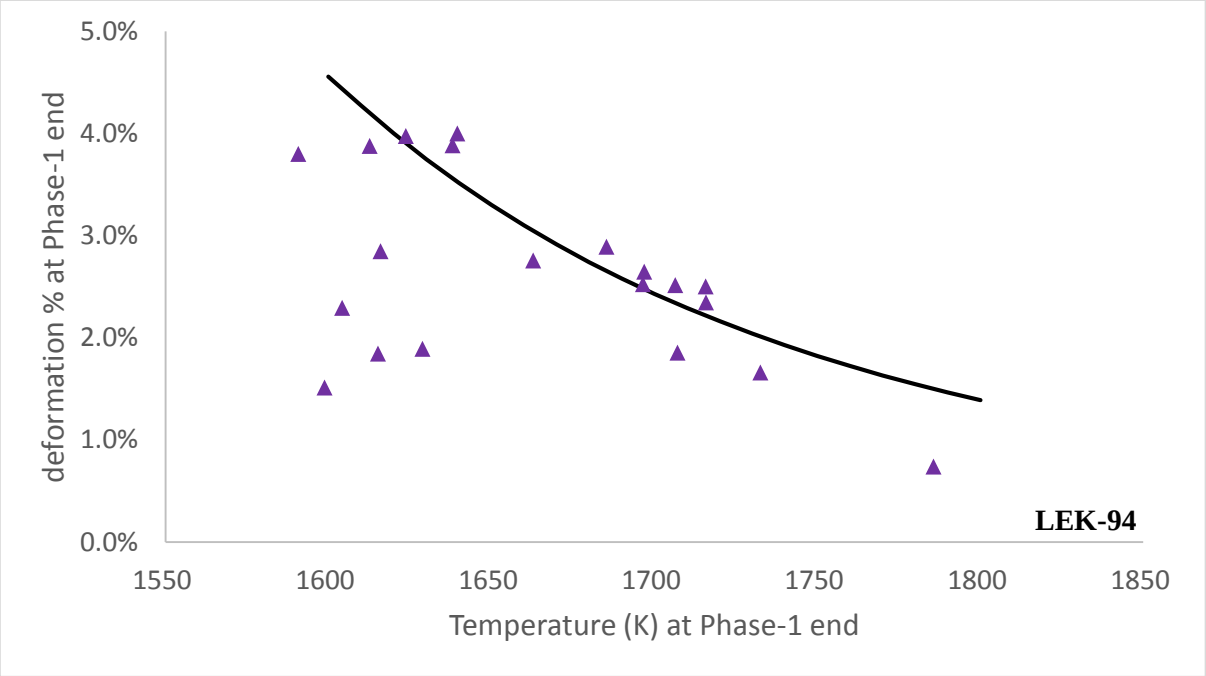

Figure 5.1.5: Viscosity and deformation dominated region for LEK-94 sample droplet

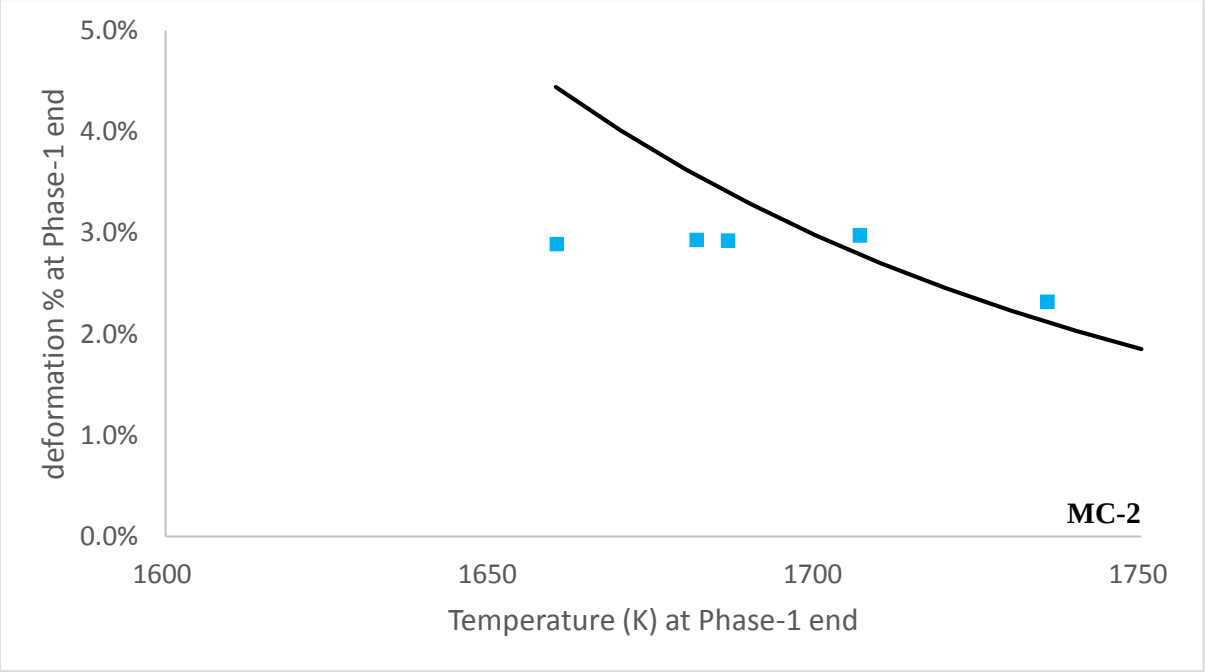

Figure 5.1.6: Viscosity and deformation dominated region for MC-2 sample droplet

Figure 5.1.7 shows the sample deformation at end of Phase-1 region versus the Phase-1 duration time. The deformation shows linearly decreasing behavior with the duration of the Phase-1 region indicating that the transition of the damping from Phase-1 to Phase-2 is not bounded by a specific magnitude for the deformation and could happen at an arbitrary deformation in a wide range – from 5% to below 1%. Since the length of the Phase-1 region is basically related to the pulse induced turbulence decay time, the critical sample deformation at the transition point could be assumed to be primarily determined by the turbulence intensity, which could also be characterized from the corresponding Reynolds number (determined by the thermophysical properties and applied heater pulse power). The Phase-1 duration time could be estimated from empirical formula defined in Equation 4.3.2 representing the turbulence decay time scale.

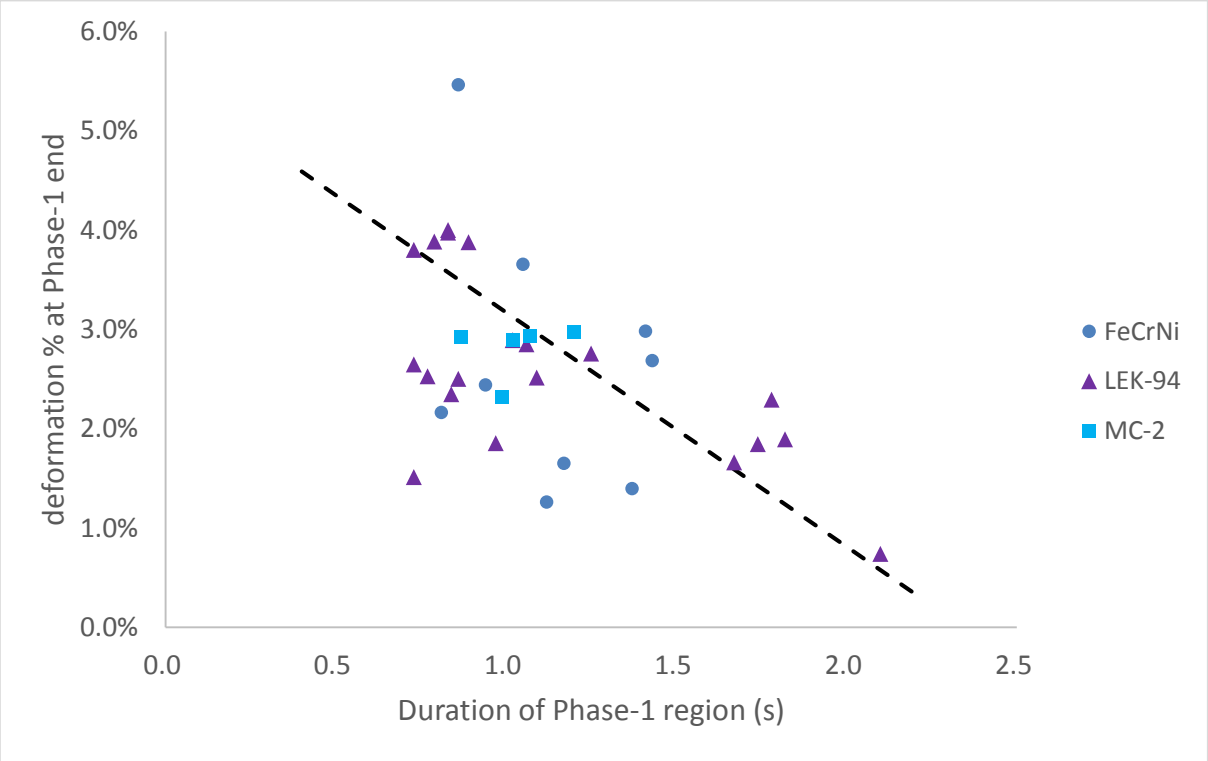

Figure 5.1.7: Deformation vs. duration time at end of Phase-1 region

It is worth noticing that the different oscillation modes influence initial droplet deformation and subsequent decay of the oscillating signals. As discussed in section 3.3.3, deformation of the droplet as observed in the Top-view becomes less with an increase in mixed mode $m=\pm 1$ oscillations. As shown in Figure 5.1.8 (a modification of Figure 3.3.2) the maximum droplet

deformation increases linearly with pulse voltage if oscillations are dominated by mode m=0. If mode m=±1 dominates, the deformation behaviour is significantly different. Although there were only two data points for 9.4V pulses, the difference in initial deformation was strikingly different due to a change from mode m=0 to m=±1. When mode m=±1 dominates, as seen in thermal cycle 7 of the LEK-94, initial deformation was limited to 4.6% which is well below the expected value of around 10%. Thermal cycle 8 of the LEK-94 alloy at the same 9.4V pulse application showed m=0 behavior and the initial deformation followed the expected trend with excitation voltage. As more oscillation mode m=±1 is added, the apparent viscosity will display up to 35% error as predicted in section 3.3.3 – which is not appropriate for viscosity measurement.

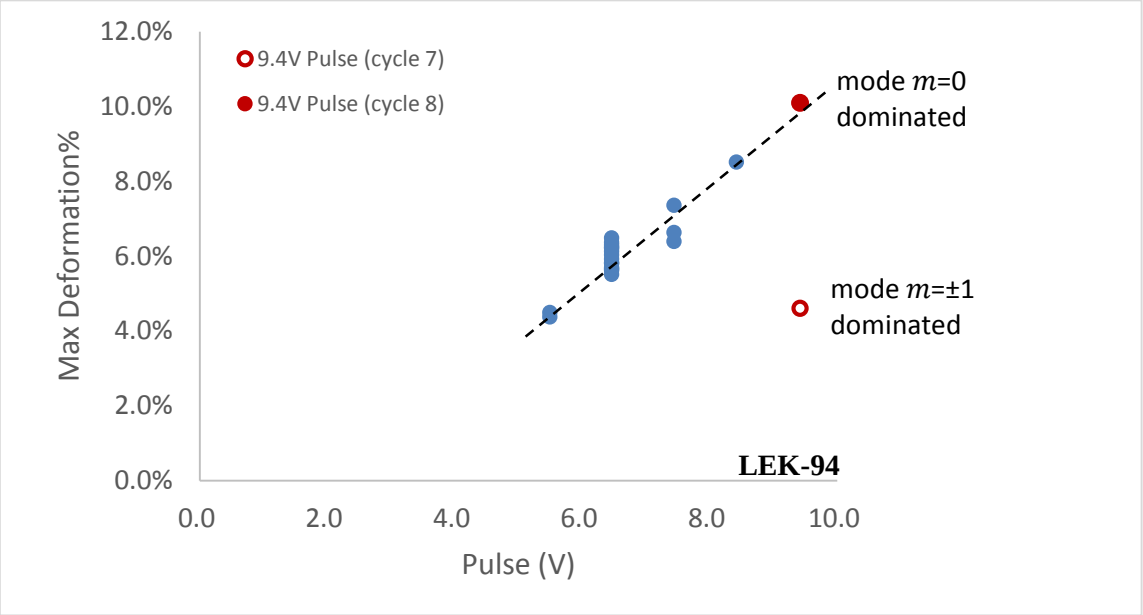

Figure 5.1.8: Maximum sample deformation vs. pulse size (oscillation modes)

5.2 Viscosity Results

The viscosities of molten $Fe_{72}Cr_{19}Ni_{21}$, LEK-94, MC-2 are measured based on the described methodology above and each is fit with an Arrhenius function as defined in Equation 3.2.1. The viscosity results are compared with ground based Electrostatic Levitation (ESL) data,

Wunderlich's data[27][71] from parabolic flight, and Brillo's data[24] using high-temperature oscillating cup viscometer, and show good agreement near the melting point T_m. For either composition, most of the measurements well above T_m are invalid due to the pulse induced turbulence, large shape deformation, and mixture of oscillation modes due to sample offset from the coil center when the pulse excitation is applied. In the Phase-2 region, the droplet is quiescent and stable allowing for valid viscosity measurements as low as from 50K to 100K undercooling.

The temperature dependent viscosity and density data are used to calculate Reynolds number and for MHD simulation in previous sections. The density (kg/m^3) relationships are summarized as,

$FeCr_{19}Ni_{21}$ (ESL data[31]): $\rho = -0.71 \cdot T + 8209$

LEK-94[28]: $\rho = -0.95 \cdot T + 8712$

MC-2[28]: $\rho = -1.30 \cdot T + 9721$

Table 5.2.1 lists the Arrhenius fit for viscosity for each composition from ISS EML experiments using the standard form of the equation such that $\mu = e^{(\frac{C_1}{T} - C_2)}$ (mPa s),

Table 5.2.1: Viscosity of $FeCr_{19}Ni_{21}$, LEK-94, and MC-2

Composition	$T_{liquidus}$ ***(K)***	C_1	C_2	***Temperature range (K)***
$FeCr_{19}Ni_{21}$	1715	$4.303 \pm 0.487 \cdot 10^4$	22.85 ± 2.9	1650-1715
LEK-94	1666	$1.743 \pm 0.068 \cdot 10^4$	8.39 ± 0.4	1560-1690
MC-2	1661	$2.849 \pm 0.165 \cdot 10^4$	14.60 ± 1.0	1610-1680

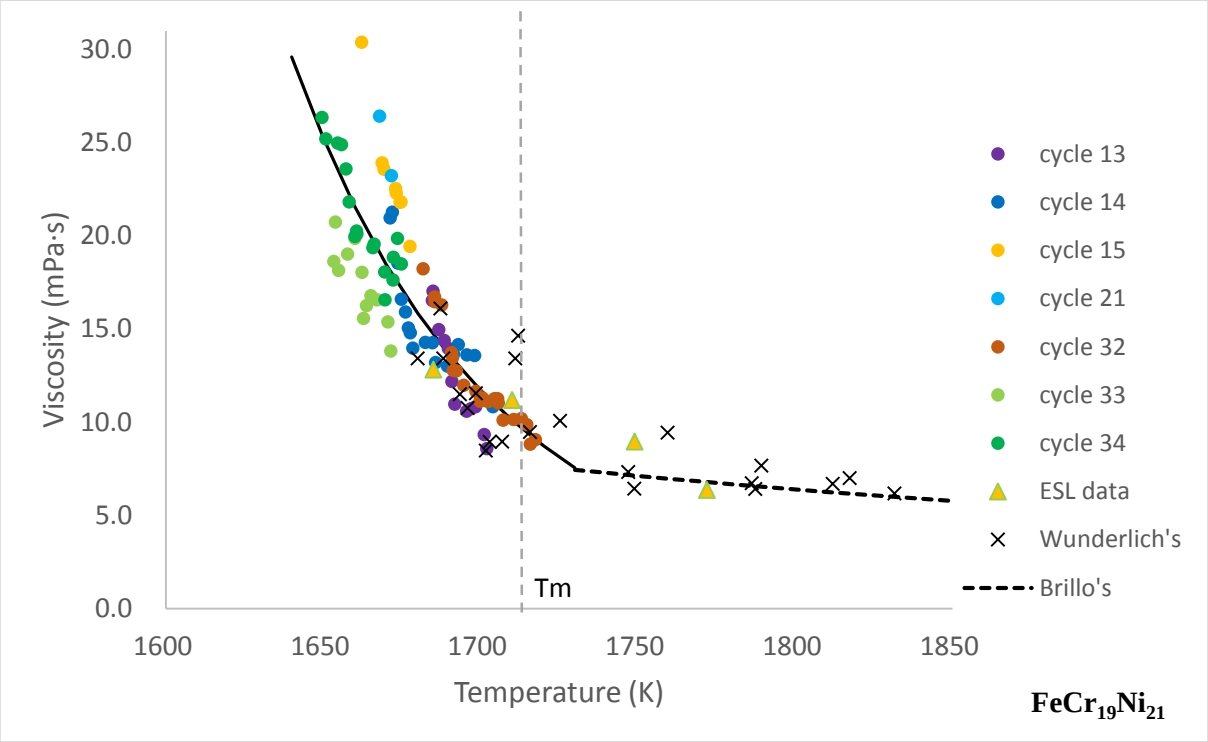

Figure 5.2.1: Viscosity of molten $FeCr_{19}Ni_{21}$

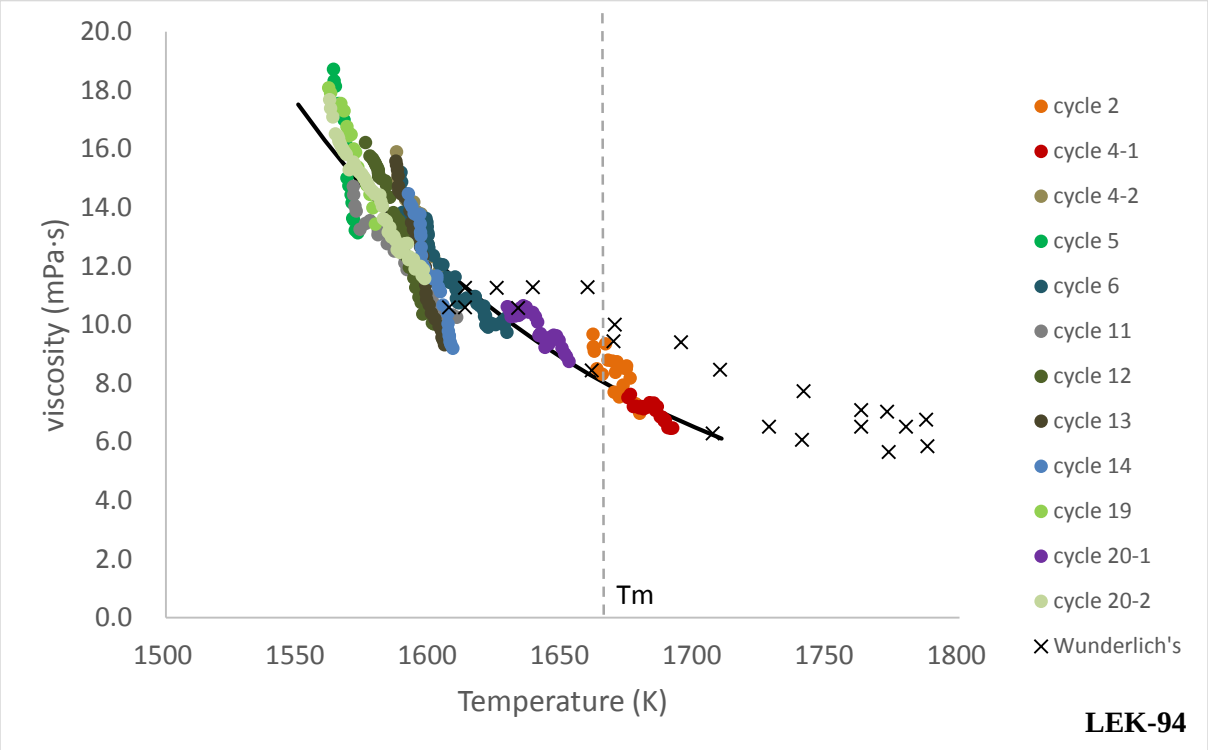

Figure 5.2.2: Viscosity of molten LEK-94

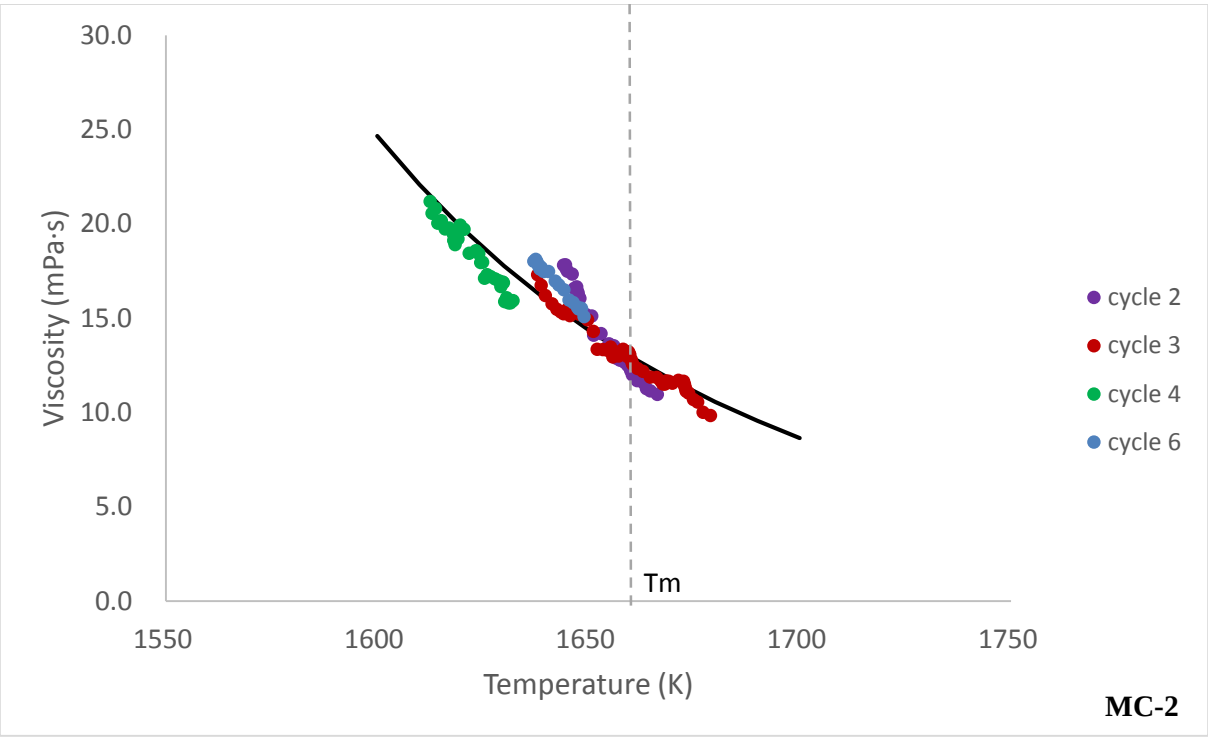

Figure 5.2.3: Viscosity of molten MC-2

Near the melting temperature for the FeCrNi alloy, the accuracy of the viscosity measurement using ISS-EML is 10.1% less than ESL, 10.7% less than Wunderlich's parabolic flight data, and 16.1% larger than Brillo's results. Over the entire temperature range the precision is 7.4% for the new space EML results based on variability defined by deviation from an Arrhenius fit. This compares well other levitation measurements where the observed precision was 10.7%, 13.8% for the ESL and parabolic flight EML respectively. Ground based rotating cup measurements showed a precision of 2.1% but it is unclear if these results are influenced by contamination issues associated with test conditions where the molten liquid is in contact with a crucible.

5.3 Experiment Parameters

During viscosity measurement, it is desirable for the sample droplet to stay in the Phase-2 region as long as possible and it is critical to reduce the Phase-1 time. These conditions are necessary to maximize science return during the limited opportunity to run experiments in

space. Through well designed experiment plans with appropriate parameter settings, the length of Phase-1 region during the pulse excited oscillation could be controlled.

In subsequent discussion, we define the duration time of Phase-1 and Phase-2 region as t_{phase1} and t_{phase2}, and the duration through the whole damped oscillation is $t_{osc} = t_{phase1} + t_{phase2}$. Thus, the ratio of $t_{phase1}/\ t_{osc}$ represents the fraction of Phase-1 region within the oscillation process. Figure 5.3.1 shows a histogram of the $t_{phase1}/\ t_{osc}$ ratio from ISS EML experiments for the three compositions. Based on statistical analysis, 80% of the data are distributed in the range of 0.2 to 0.4, and the remainder of the data could reach values up to 1.0 indicating that a minority of cycles are mostly Phase-1 due to inappropriate settings of the size or timing of the heater pulse.

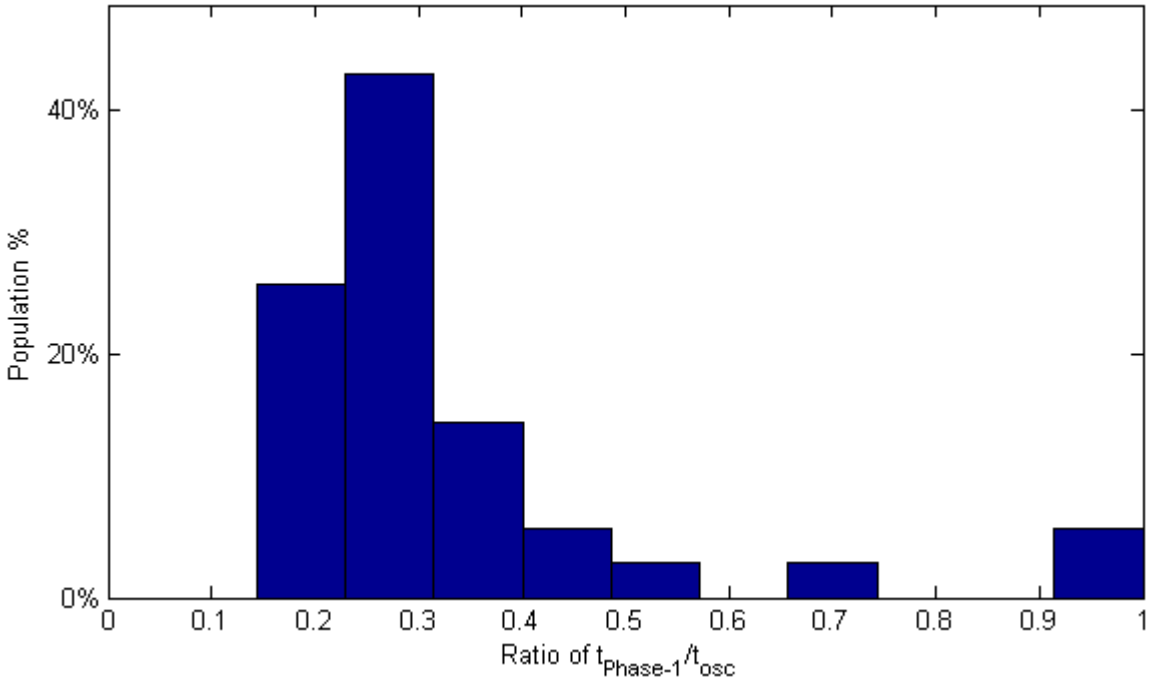

Figure 5.3.1: Histogram of Phase-1/Oscillation time ratio $t_{phase1}/\ t_{osc}$

The duration of the Phase-1 region t_{phase1} could be estimated in a fashion similar to Equation 4.3.3 such that,

$$t_{phase1} = C_{\varepsilon_1} \log_{10}(Re) + C_{\varepsilon_2} \tag{5.3.1}$$

In the empirical formula, C_{ε_1}=1.413 and C_{ε_2}= -3.317.

The Reynolds number calculated from Equation 4.1.3 is obtained from MHD simulation, which could be treated as a linear function of temperature for different pulse settings,

$$Re = C_{Re_1}^{Pul} T_0 + C_{Re_2}^{Pul} \tag{5.3.2}$$

Where T_0 is the temperature while heater pulse is applied, and for temperature T which is decreasing with time and cooling rate γ,

$$T = T_0 - \gamma t \tag{5.3.3}$$

Thus, t_{phase1} could be expressed as follows,

$$t_{phase1} = C_{\varepsilon_1} \log_{10}\left(C_{Re_1}^{Pul} T_0 + C_{Re_2}^{Pul}\right) + C_{\varepsilon_2} \tag{5.3.4}$$

When the oscillating sample droplet is damped to a small magnitude, the oscillation deformation η_d could be considered as damped out where η_d is assumed to be around 0.5% or equivalent to the level of the background noise, as described in Section 2.3.4. At the end of Phase-1 region, η_{d_0} is related with the duration time of Phase-1, as shown in Figure 5.1.7, and can be approximated with the following linear fit,

$$\eta_{d_0} = C_{\eta_1} t_{phase1} + C_{\eta_2} \tag{5.3.5}$$

Where the fitted parameters C_{η_1}=-0.0236, C_{η_2}=0.05534.

During the Phase-2 region, the magnitude of the deformation is subjected to exponential decaying from the deformation remaining at the end of the Phase-1 region, with damping constant τ,

$$\eta_d = \eta_{d_0} e^{-\frac{(t_{osc} - t_{phase1})}{\tau}} \tag{5.3.6}$$

The damping constant τ is defined in Equation 2.3.1, for oscillation mode l=2, τ has the following expression,

$$\tau = \frac{\rho {R_0}^2}{5\mu} \tag{5.3.7}$$

Where the viscosity μ is subjected to Arrhenius fit, where C_{μ_1} and C_{μ_2} is the coefficient for specific alloy composition,

$$\mu \approx e^{\left(\frac{C_{\mu_1}}{T_0 - \gamma(\alpha t_{phase1})} + C_{\mu_2}\right)} \tag{5.3.8}$$

During the damped oscillation in the Phase-2 region, the viscosity μ is increasing with time as well, and thus an averaged viscosity in the Phase-2 region is used. Usually t_{phase2} could be less than t_{phase1} while the length of Phase-1 region is large, or up to 4 times of t_{phase1} while the Phase-2 region is dominant. For $t_{phase1}/\, t_{osc}$ with a ratio of 0.2 to 0.4, the value of α could be estimated as 1.5 to 2.5.

Thus, the duration of oscillation t_{osc} could be expressed as follows,

$$\begin{aligned} t_{osc} &= t_{phase1} + \tau \log\left(\frac{\eta_{d_0}}{\eta_d}\right) \\ &= t_{phase1} + \frac{\rho {R_0}^2}{5e^{\left(\frac{C_{\mu_1}}{T_0 - \gamma(\alpha t_{phase1})} + C_{\mu_2}\right)}} \log\left(\frac{C_{\eta_1} t_{phase1} + C_{\eta_2}}{\eta_d}\right) \end{aligned} \tag{5.3.9}$$

Both of t_{phase1} and t_{osc} defined in Equation 5.3.4 and Equation 5.3.9 are functions of temperature T_0 and heater pulse voltage V_H^{Pul}, and $t_{phase1}/\, t_{osc}$ ratio could be calculated accordingly for different temperature and pulse settings.

As an example using data from the LEK-94, the Reynolds number has the following fit based on MHD simulations,

$$\begin{aligned} V_H^{Pul}&=5.49\text{V},\ Re = 15.10T - 2.30\cdot 10^4 \\ V_H^{Pul}&=6.46\text{V},\ Re = 18.45T - 2.82\cdot 10^4 \\ V_H^{Pul}&=7.44\text{V},\ Re = 21.63T - 3.30\cdot 10^4 \\ V_H^{Pul}&=8.42\text{V},\ Re = 24.78T - 3.77\cdot 10^4 \end{aligned} \tag{5.3.10}$$

And the coefficients of viscosity are,

$$\begin{aligned} C_{\mu_1} &= 1.743\cdot 10^4/\log 10^3 \\ C_{\mu_2} &= -8.39/\log 10^3 \end{aligned} \tag{5.3.11}$$

If sample is cooling down with heater off, the cooling rate will be $\gamma \approx 19.5\ K/s$. In contrast, with the heater set to 0.3V the cooling rate becomes $\gamma \approx 14.5\ K/s$.

Figure 5.3.2 shows the predicted $t_{phase1}/\,t_{osc}$ ratio for various pulse sizes as applied at different temperature. For pulses larger than 6.46V, the $t_{phase1}/\,t_{osc}$ ratio increases rapidly from superheated 1700K to 1750K, and could achieve the value from 0.6 to 1.0 for a large pulse applied at a highly superheated temperature, indicating the corresponding pulse excited oscillation is Phase-1 dominated and thus not appropriate for viscosity measurement purposes for these experimental parameters. For pulses below 6.46V, the $t_{phase1}/\,t_{osc}$ ratio is expected to be in the range from 0.2 to 0.5 for a moderately superheated sample.

Statistically, the existing experiments show agreement with the above predictions where most of the pulses for LEK-94 are applied with magnitude of 6.46V and at temperature in the range of 1600K to 1730K, and the $t_{phase1}/\,t_{osc}$ ratio is primarily in the range of 0.2 to 0.4.

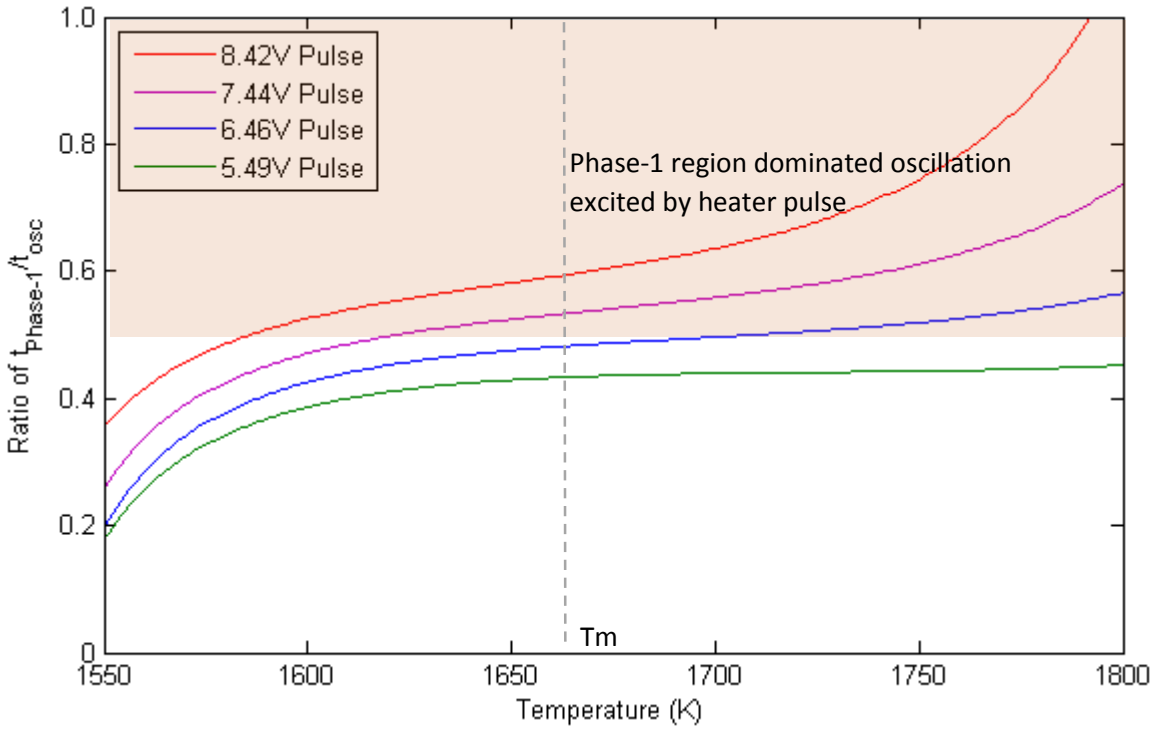

Figure 5.3.2: Ratio of $t_{phase1}/\ t_{osc}$ vs. temperature/pulse voltage

For a well-designed experiment, the pulse excited oscillation should not be Phase-1 dominated, and the $t_{phase1}/\ t_{osc}$ ratio should be less than 0.5. For 5.49V pulse, the ratio is expected to be in the acceptable range; for 6.46V pulse, the critical temperature is around 1710K; for 7.44V and 8.42V pulse, the critical temperature is around 1630K and 1590K respectively, indicating that the oscillation would be possibly Phase-1 dominated when the sample is under less than 200K superheating. Similar observations are apparent for LEK-94 as shown in Figure 4.3.2. The Phase-1 duration times for the oscillation excited by 7.44V and 8.42V pulse are significantly higher than the pulses below 6.46V.

Based on these predications, several recommendations are apparent. A heater pulse larger than 7.44V should be applied at an undercooling temperature well below T_m, while a 6.46V pulse should be applied at a moderate superheating less than 40K, and a 5.49V pulse should be applied at a relatively larger superheating. Figure 5.3.3 shows the critical temperature for each pulse setting, the pulse application temperature should be limited to below the suggested limit curve based on identification of a critical temperature for viscosity measurement. There is an

estimated error of 30K to 60K in this critical temperature curve due to the sum of uncertainties from viscosity precision, Reynolds number estimation error, and fitting errors in the experimental data.

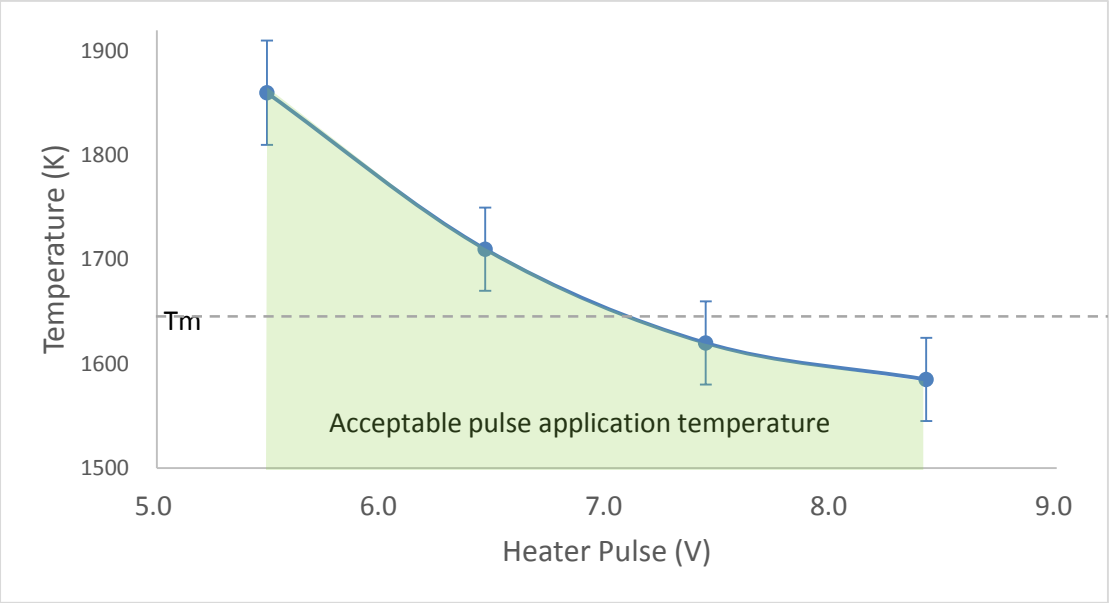

Figure 5.3.3: Critical temperature for pulse application

Thus, an appropriate pulse voltage could be selected for certain testing temperatures, and pulses below 6.46V are suitable for measurement above T_m. However, pulse application with much lower voltage may not result in a successful measurement either. The excitation pulse needs of appropriate magnitude to excite sufficient initial and/or maximum deformation of the sample droplet to allowing tracking of the decay of the deformation. For an oscillation starting with a deformation below 4%, at the end of Phase-1 region the sample deformation would quickly decreases to below 3% to 2%, and the evaluation of damping rate in Phase-2 region would be limited if not fully obscured by the limited video resolution or accumulation of background noise. As shown in Figure 3.3.2, the maximum deformation η_0 has the following approximate linear relation with the heater pulse,

$$\eta_0 = C_{H_1} V_H^{Pul} + C_{H_2} \tag{5.3.12}$$

Where V_H^{Pul} is the heater pulse voltage in the range of 5.49V to 8.42V, and fitted parameters C_H=0.01233, C_{H_2}= -0.02067.

The maximum deformation η_0 is usually around 4.5% for 5.49V pulse, 6.5±0.5% for 6.46V pulse, and larger than 7.3% for pulse above 7.44V. Thus, a pulse below 5.49V might not be able to provide enough sample deformation at the beginning of the pulse excited oscillation for accurate viscosity measurement. A magnitude of 5% to 7% initial sample deformation at the start of Phase-1 region is considered to be appropriate to avoid the limitations imposed by either too small or too large a sample deformation.

6 Conclusions

The damping behavior of induced surface oscillation of electromagnetically levitated molten metal droplets has been modeled and evaluated for viscosity measurement purposes. Through this work, the accomplishments could be drawn in the following aspects:

1. Oscillation Signal Processing:

- Oscillation damping of levitated droplets is captured using high-speed cameras and an elliptical fit of the droplet's projection image could be used to track deformation decay with time. This technique is an improvement over previous protocol because of capability to dynamically capture the shape change of oscillating droplet under arbitrary deflection angle.
- The influence of aliasing of captured deformation signals due to selection of a reduced camera acquisition rate settings is presented. An acquisition rate larger than 100Hz is acceptable for signal processing with droplet natural frequencies between 30Hz to 40Hz.
- The oscillation damping rate of the molten metal droplet under different temperatures could be evaluated through use of a fitting coefficient to optimize segmentation of the decay curve for different test temperatures with error of 10K-20K and curve fitting error less than 5%.

2. Oscillation Behavior Analysis:

- The droplet oscillation excited by the EML heater pulse is shown to be subjected to different oscillation modes governed by spherical harmonics. It is mathematically proven that the two-dimensional projection of the deformed droplet could be approximated to be an ellipse for radius deformation less than 10%, indicating the validity of the elliptical fitting method used for oscillating signal analysis and tracking of deformation decay.
- The damped oscillation induced from heater pulse could be separated into Phase-1 and Phase-2 regions based on the difference in characteristic damping behavior. The apparent viscosity measured from Phase-1 region is nominally 2-4 times higher than the expected values, while Phase-2 region is reliable for viscosity measurement. The duration of Phase-1 region could be determined based on a damping behavior transition time and during this period decay is dominated by turbulence induced from the heater pulse.
- Magnetohydrodynamic (MHD) modeling is used to predict the internal recirculation velocity of the molten metal droplet under various heater/pulse power settings and a wide range of testing temperature, and the flow condition could be characterized by Reynolds number that

is positively correlated with the heater pulse voltage and molten sample's thermophysical properties regarding to the temperature. Turbulence induced from either high temperature or with large pulse size is the dominating factor influencing the viscosity measurement and will make the apparent viscosity up to 4 times higher than expected values. This is of the same order of magnitude as predictions from MHD simulation using the k-ε turbulence model. A new formula is established to estimate the turbulence decay time as function of the Reynolds number which is validated by comparison to data from ISS EML experiments.

- Potential factors other than turbulence that would skew the damping rate analysis and viscosity measurement are evaluated. (1) A larger distance greater than 4% between the sample droplet and centerline of the EML coil at the time of the pulse application would induce a fraction of more than 50% oscillation mode l=2, m=±1 mixed in with the normal mode m=0, which could make the damping rate overestimated 10%-35% using the Top-view camera (2) The magnitude of the droplet deformation is not the primary factor influencing determination of apparent viscosity in the Phase-1 region because the effects of induced turbulence dominate. Deformation can introduce less than 20% error during viscosity measurement in the Phase-2 region. (3) The influence of anharmonic oscillation due to nonlinear effect is shown to be negligible during damping analysis for current experimental conditions using the ISS EML.

3. Viscosity Analysis and Results:

- Temperature dependent viscosities of FeCrNi, LEK-94, and MC-2 are measured in the Phase-2 oscillation region.
- Viscosity is not measured in superheat because of Phase-1 dominates the region.
- The viscosity of FeCrNi measured using ISS-EML shows an accuracy of 10.1% less than ESL, 10.7% less than parabolic flight data, and 16.1% larger than Brillo's results near melting temperature.
- Over the entire temperature range the precision is 7.4% for the new space EML results. This compares well other levitation measurements where the observed precision was 10.7%, 13.8% for the ESL and parabolic flight EML respectively. Ground based rotating cup measurements showed a precision of 2.1% but it is unclear if these results are influenced by contamination issues associated with test conditions where the molten liquid is in contact with a crucible.

4. Experiment Parameters Design:

- Restrictions on the pulse application temperature are predicted for effective viscosity measurement during the ISS EML experiment. For the experiment design, an appropriate pulse voltage could be selected based on the suggested temperature limits.
- Pulse voltage has lower limit at 5V to provide enough time for the droplet to damp out for data analysis purpose.
- Pulse voltage has upper limit at 8V to avoid occupation of turbulence during most time of the droplet oscillation to allow effective viscosity measurement.

7 Future Work

The future work includes the following aspects:

- Extend the viscosity measurement utilizing EML in microgravity to a broad range of alloy systems of interest, including glass-forming alloys with high viscosity, and validate the criterion of experiment design for viscosity measurement in future ISS missions.

- Extrapolate the damping analysis method to viscosity measurement utilizing ESL. Of particular interest is the observation that the dominating factor involving turbulence effects in EML is not applicable for ESL since flow inside an ESL droplet is laminar and induced by fluid motion alone. The mechanism for excitation is different when comparing EML and ESL and operational limits will be dramatically different.

- Develop a numerical model to predict the magnitude of droplet deformation in EML subjected to different pulse voltage and sample temperature.

- For better accuracy, develop dynamic MHD models utilizing the method of direct numerical simulation or large eddy simulation instead of the k-ε turbulence model to predict the flow conditions inside the levitated droplet in EML.

References

[1] E.C. Okress, D.M. Wroughton, G. Comenetz, P.H. Brace, and J.C.R. Kelly, "Electromagnetic Levitation of Solid and Molten Metals", J. Appl. Phys., Vol. 23 No. 5(1952), 545-552.

[2] G. Lohöfer, "Theory of an Electromagnetically Levitated Metal Sphere", SIAM J. Appl. Math., 49(2), 567–581.

[3] G. Lohöfer, "Magnetization and Impedance of an Inductively Coupled Metal Sphere", Int. J. Engng Sci., Vol. 32 No. 1(1994), 101-117.

[4] G. Lohöfer, "An Electrically Conducting Sphere in a 3-D Alternating Magnetic Field", SIAM J. Appl. Math., 68(2003), 1–21.

[5] N. El-Kaddah and J. Szekely, "The Electromagnetic Force Field, Fluid Flow Field, and Temperature Profiles in Levitated Metal Droplets", Met. Trans. B, Vol. 14B(1993), 401.

[6] E. Schwatz, S. Sauerland, J.Szekely, and I. Egry, "On the shape of liquid metal droplets in Electromagnetic levitation experiments", Containerless Processing: techniques and applications TMS Denver (1993), 57-64.

[7] G. Lohöfer, "Basics for the Determination of Temperature-Time Profiles of Samples Processed in the TEMPUS and EML Facility", EML-GSP Physical Note (2012).

[8] T. Iida, and R.I.L. Guthrie, "The Physical Properties of Liquid Metals", Clarendon Press, Oxford 1988.

[9] R.F. Brooks, A.T. Dinsdale, and P.N. Quested, "The Measurement of Viscosity of Alloys - A Review of Methods, Data and Models", Measurement and Science Technology, Vol. 16(2005), 354-362.

[10] H. Lamb, "On the oscillations of a viscous liquid globe", Proceedings of the London Math Society, Vol. 13 No 1(1881), 51-66.

[11] H. Lamb, Hydrodynamics, Dover New York, 1945.

[12] J.W.S. Rayleigh, "On the Capillary Phenomena of Jets", Proceedings of the Royal Society of London, Vol. 29(1879), 71-97.

[13] P. V. R. Suryanarayana, and Y. Bayazitoglu, "Surface Tension and Viscosity from Damped Free Oscillations of Viscous Droplets", Int. J. Thermophys., Vol. 12 No. 1(1991), 137-151.

[14] E. Beckery, W.J. Hiller, and T.A. Kowalewski, "Nonlinear dynamics of viscous droplets", J. Fluid Mech., 258(1994), 191-216.

[15] E. Becker, W.J. Hiller, and T. A. Kowalewski, "Experimental and theoretical investigation of large amplitude oscillations of liquid droplets", J. Fluid Mech., Vol. 231(1991), 189 210.

[16] H. Soda, A. McLean, and W. A. Miller, “The influence of oscillation amplitude on liquid surface tension measurements with levitated metal droplets”, Met. Trans. B, Vol. 9B(1978), 145-147.

[17] J. Etay, P. Schetelat, B. Bardet, J. Priede, V. Bojarevics, and K. Pericleous, “Modelling of Electromagnetic Levitation: Consequence on Noncontact Physical Properties Measurements”, Temperature Materials and Processes, 27-6(2008). 439-447.

[18] D.V. Lyubimov, V. Konovalov, T.P Lyubimoa, I Egry, “Small amplitude shape oscillations of a spherical liquid drop with surface viscosity”, J. Fluid Mech., Vol. 677(2011), 204-217.

[19] P.F. Paradis, T. Ishikawa, and S. Yoda, “Non-contact measurements of surface tension and viscosity of niobium, zirconium, and titanium using an electrostatic levitation furnace”, Int. J. Thermophys., Vol. 23 No. 3(2002), 825-842.

[20] J. Lee, P. Choufani, R.C. Bradshaw, R.W. Hyers, and D.M. Matson, “Containerless Measurements of Density and Viscosity of Fe-Co Alloys”, Materials Research in Microgravity (2012), 97-104.

[21] T. Ishikawa, P.F. Paradis, N. Koike, and Y. Watanabe, “Effects of the positioning force of electrostatic levitators on viscosity measurements”, Rev. Sci. Instrum., 80, 013906 (2009).

[22] M. P. SanSoucie, J. R. Rogers, V. Kumar, J. Rodriguez, X. Xiao, and D. M. Matson, “Effects of Environmental Oxygen Content and Dissolved Oxygen on the Surface Tension and Viscosity of Liquid Nickel”, Int. J. Thermophys., 37:76(2016).

[23] I. Egry, H. Giard, and S. Schneider, “The oscillating drop technique revisited”, Measurement science and technology, 16, 2(2005), 426.

[24] H. Kobatake, J. Brillo, “Density and viscosity of ternary Cr–Fe–Ni liquid alloys”, J Mater Sci., (2013) 48: 6818.

[25] R.W. Hyers, G. Trapaga, and M.C. Flemings, “Surface tension and viscosity measurements in microgravity: results from space shuttle and parabolic fight experiments”.

[26] H.J. Fecht, and R.K. Wunderlich, “The thermolab project: thermophysical properties of industrially relevant liquid metal alloys”, 2000.

[27] R.K. Wunderlich, H.J. Fecht, and G. Lohöfer, “Surface Tension and Viscosity of the Ni-Based Superalloys LEK94 and CMSX-10 Measured by the Oscillating Drop Method on Board a Parabolic Flight”, Met. Trans. B., Vol. 48B(2017), 237-246.

[28] S. Amore, F. Valenza1, D. Giuranno, R. Novakovic, G. D. Fontana, L. Battezzati, E. Ricci, “Thermophysical properties of some Ni-based superalloys in the liquid state relevant for solidification processing”, J Mater Sci., 51(2016), 1680–1691.

[29] I. Egry, G. Lohöfer, I. Seyhan, S. Schneider, and B. Feuerbacher, "Viscosity of eutectic $Pd_{78}Cu_6Si_{16}$ measured by the oscillating drop technique in microgravity", Appl. Phys. Lett., 73, 462 (1998).

[30] R.W. Hyers, G. Trapaga, and M.C. Flemings, "The measurement of the surface tension and viscosity of undercooled melts under microgravity conditions", TMS, Solidification(1999), 23-31.

[31] D.M. Matson, X. Xiao, J Rodriguez, and R.K. Wunderlich, "Preliminary Experiments Using Electromagnetic Levitation On the International Space Station", Int. J. Microgravity Sci. Appl., 33 (2) (2016) 330206.

[32] M. Perez, L. Salvo, and M. Suery, "Contactless viscosity measurement by oscillations of gas-levitated drops", Phys. Rev. E., Vol. 61-3(2000), 2669-2675.

[33] G. Lohöfer, "Evaluation of surface oscillations of droplets levitated in TEMPUS using the SCE", 2014.

[34] G. Lohöfer, "Inductive measurement of thermophysical properties of electromagnetically levitated metallic melts", High Temperatures-High Pressures, Vol. 40(2010), 237–248.

[35] E.M. Schwartz, "Measurement of Surface Tension of Electromagnetically-Levitated Droplets in Microgravity", Ph.D. Thesis, Massachusetts Institute of Technology, 1995.

[36] R.W. Hyers, "Modeling and Experiments on Electromagnetic Levitation for Material Processing", Ph.D. Thesis, Massachusetts Institute of Technology, 1998.

[37] D.M. Matson, D.J. Fair, R.W. Hyers, and J.R. Rogers, "Contrasting Electrostatic and Electromagnetic Levitation Experimental Results for Transformation Kinetics of Steel Alloys", Ann. NY Acad. Sci., 1027(2004), 435–446.

[38] A.B. Hanlon, D.M. Matson, and R.W. Hyers, "Internal convective effects on the lifetime of the metastable phase in under cooled Fe-Cr-Ni alloys", Philosophy Magazine Letter, 86(2006), 165–174.

[39] A.B. Hanlon, D.M. Matson, and R.W. Hyers, "Microgravity Experiments on the effect of Internal Flow on Solidification of Fe-Cr-Ni Stainless Steels", Ann. NY Acad. Sci., 1077, (2006), 33–48.

[40] N. El-Kaddah, and J. Szekely, "Heat and Fluid Flow Phenomena in a Levitation Melted Sphere under Zero Gravity Conditions", Met. Trans. B, Vol. 15B(1984), 183-186.

[41] R.W. Hyers, D.M. Matson, K.F. Kelton, J.R. Rogers, "Convection in Containerless Processing", Ann. NY Acad. Sci., 1027(2004), 474–494.

[42] R.W. Hyers, "Fluid effects in levitated droplets", Measurement science and Technology 16, 2 (2005), 394.

[43] S. Berry, R.W. Hyers, B. Abedian, and L.M. Racz, "Modeling of turbulent flow in electromagnetically levitated metal droplets", Met. Trans. B., 31(2000), 171–8.

[44] S. R. Berry, R. W. Hyers, L. M. Racz, B. Abedian, "Surface Oscillations of an Electromagnetically Levitated Droplet", Int. J. Thermophys., Vol. 26 No.5(2005), 1565–1581.

[45] R.W. Hyers, G. Trapaga G, and B. Abedian, "Laminar-turbulent transition in an electromagnetically levitated droplet", Metall. Mater. Trans. B., 34(2003), 29–36.

[46] J. Lee, D.M. Matson, S. Binder, M. Kolbe, D. Herlach, and R.W. Hyers, "Magnetohydrodynamic Modeling and Experimental Validation of Convection Inside Electromagnetically-Levitated Co-Cu droplets", Metall. Mater. Trans. B., 45(2014), 1018–1023.

[47] J. Lee, X. Xiao D.M. Matson, and R.W. Hyers, "Numerical Prediction of the Accessible Convection Range for the Molten $Fe_{50}Co_{50}$ in support of the International Space Station Experiments", Metall. Mater. Trans. B., 2014.

[48] M.C. Flemings, D.M. Matson, J.R. Rogers, W. Löser, and R.W. Hyers, "Science Requirements Document for Levitation Observation of Dendrite Evolution in Steel Ternary Alloy Rapid Solidification (LODESTARS-SRD)", 2003.

[49] V. Bojarevics, and K. Pericleous, "Modelling Electromagnetically Levitated Liquid Droplet Oscillations", ISIJ International, Vol. 43 No. 6 (2003), 890–898.

[50] V. Bojarevics, A. Roy, and K. Pericleous, "Magnetic levitation of large liquid volume", Magnetohydrodynamics, Vol. 46 No. 4(2010), 317–329.

[51] S. Easter, V. Bojarevics, and K. Pericleous, "3D numerical modelling of liquid droplet dynamics in a high DC magnetic field", 8th PAMIR International Conference on Fundamental and Applied MHD, 2011.

[52] S. Easter, V. Bojarevics, and K. Pericleous, "Numerical Modelling of Liquid Droplet Dynamics in Microgravity", Journal of Physics: Conference Series, 327(2011), 012027.

[53] S. Easter, "Modelling of Liquid Droplet Dynamics in a High DC Magnetic Field", Ph.D. Thesis, University of Greenwich, 2012.

[54] V. Shatrov, J. Priede, G. Gerbeth, "Three-dimensional linear stability analysis of the flow in a liquid spherical droplet driven by an alternating magnetic field", Physics of Fluids, Vol. 15 No.3(2003), 668-678.

[55] E. Bjorklund, "The level-set method applied to droplet dynamics in the presence of an electric field", Computers & Fluids, 38(2009), 358-369.

[56] J. Lee, X. Xiao, D.M. Matson, and R.W. Hyers, “Characterization of Fluid Flow inside Electromagnetically-Levitated Molten Iron-Cobalt Droplets for ISS Experiments”, TMS, 2013.

[57] D.M. MATSON, M. Watanabe, G. Pottlacher, G.W. LEE, and H.J. Fecht, “Thermophysical Property Measurement: A Call to Action”, Int. J. Microgravity Sci. Appl., 33 (3) 2016, 330304.

[58] M.J. Todda, and E.A. Yildirim, “Approximate Minimum Volume Enclosing Ellipsoids Using Core Sets”, Journal of Optimization Theory and Applications, 2005.

[59] M.J. Todda, and E.A. Yildirim, “On Khachiyan's algorithm for the computation of minimum-volume enclosing ellipsoids”, Discrete Applied Mathematics, Vol.155 No.13(2007), 1731-1744.

[60] W.H. Reid, “The Oscillations of a Viscous Liquid Drop”, Quarterly of Applied Mathematics, Vol. 18(1960), 86-89.

[61] D.B. Khismatullin, A. Nadim, “Shape oscillations of a viscoelastic drop”, Phys. Rev. E., 63(2001), 061508.

[62] G. Arfken, “Mathematical Methods for Physicists”, Academic Press, 2012.

[63] MATLAB Documentation, MathWorks, Inc.

[64] P.K. Kundu, I.M. Cohen, “Fluid Mechanics”, Academic Press, 2004.

[65] ANSYS-Fluent 12.0 User's Guide, ANSYS, Inc.

[66] X. Xiao, “Magnetohydrodynamic Modeling of Convection inside Electromagnetically-Levitated Molten $Fe_{50}Co_{50}$ Droplets”, Master Thesis, Tufts University, 2013.

[67] G.K. Batchelor, “The Theory of Homogeneous Turbulence”, Cambridge University Press, 1953.

[68] D. Hurst, J.C. Vassilicos, “Scalings and decay of fractal-generated turbulence”, Physics of Fluids, 19(2007), 035103.

[69] J.C. Vassilicos, “An infinity of possible invariants for decaying homogeneous turbulence”, Phys. Lett. A., 375(2011), 1010–1013.

[70] P.C. Valente, and J.C. Vassilicos, “Dependence of decaying homogeneous isotropic turbulence on inflow conditions”, Phys. Lett. A., 376(2012), 510–514.

[71] R.K. Wunderlich, and H.J Fecht, DLR Parabolic Flight 2013 & 2014A Review Meeting, Jun 2014.

[72] J. Valencia, P. Quested, “Thermophysical Properties”, ASM Handbook, Vol. 15(2008): 468-481.0